2009

Characterization of Fracture and Debonding of Silicon Particles in Aluminium Silicon Alloys

Jun Feng Su
University of Windsor

CHARACTERIZATION OF FRACTURE AND DEBONDING OF SILICON PARTICLES IN ALUMINIUM SILICON ALLOYS

by

Jun Feng Su

A Thesis
Submitted to the Faculty of Graduate Studies
through Engineering Materials
in Partial Fulfillment of the Requirements for
the Degree of Master of Applied Science at the
University of Windsor

Windsor, Ontario, Canada
2009

Characterization of Fracture and Debonding of Silicon Particles in Aluminium Silicon Alloys

by

Jun Feng Su

APPROVED BY:

_____

Dr. Tirupati Bolisetti, Outside Department Reader
Department of Civil and Environmental Engineering

_____

Dr. Henry Hu, Department Reader
Department of Mechanical, Automotive and Materials Engineering

_____

Dr. Vesselin Stoilov, Co-advisor
Department of Mechanical, Automotive and Materials Engineering

_____

Dr. Xueyuan Nie, Co-advisor
Department of Mechanical, Automotive and Materials Engineering

_____

Dr. Randy Bowers, Chair of Defense
Department of Mechanical, Automotive and Materials Engineering

15 May 2009

Declaration of Co-Authorship / Previous Publication

I. Co-Authorship Declaration

I hereby declare that this thesis incorporates material that is result of joint research, as follows:

This thesis incorporates the outcome in collaboration with Dr. Qi Yang (Structures, Materials and Propulsion Laboratory, Institute of Aerospace Research, Ottawa, Ontario K1A 0R6, Canada) under the supervision of Professors Vesselin Stoilov and Xueyuan Nie. The collaboration is covered in Chapter 3.2.1 of the thesis. In all cases, the key ideas, primary contributions, experimental designs, data analysis and interpretation, were performed by the author, and the contribution of the co-author was primarily through the provision of nanoindentation experiments.

I am aware of the University of Windsor Senate Policy on Authorship and I certify that I have properly acknowledged the contribution of other researchers to my thesis, and have obtained written permission from each of the co-author(s) to include the above material(s) in my thesis.

I certify that, with the above qualification, this thesis, and the research to which it refers, is the product of my own work.

II. Declaration of Previous Publication

This thesis includes 1 original paper that has been previously submitted for publication in peer reviewed journal, as follows:

Thesis Chapter	Publication title/full citation	Publication status
Chapter 3 & 4	J.F. Su, V. Stoilov, X. Nie, Q. Yang, *Characterization of the Al/Si interfaces under dry wear conditions*. Journal of Vacuum Science and Technology A, 2009. **27**(4)	In press

I certify that I have obtained a written permission from the copyright owner(s) to include the above published material(s) in my thesis. I certify that the above material describes work completed during my registration as graduate student at the University of Windsor.

I declare that, to the best of my knowledge, my thesis does not infringe upon anyone's copyright nor violate any proprietary rights and that any ideas, techniques, quotations, or any other material from the work of other people included in my thesis, published or otherwise, are fully acknowledged in accordance with the standard referencing practices. Furthermore, to the extent that I have included copyrighted material that surpasses the bounds of fair dealing within the meaning of the Canada Copyright Act, I certify that I have obtained a written permission from the copyright owner(s) to include such material(s) in my thesis.

I declare that this is a true copy of my thesis, including any final revisions, as approved by my thesis committee and the Graduate Studies office, and that this thesis has not been submitted for a higher degree to any other University of Institution.

ABSTRACT

AlSi alloy engines have been used to reduce fuel consumption and CO_2 emission. The wear resistance of AlSi surface is thought to originate from the high hardness of the silicon surface formed by the primary Si particles (inclusions). The mechanical strength of the Al/Si interface and fracture toughness of Si particles in Al matrix are the primary factors determining the strength on the load bearing formation.

In this work, a hybrid method to characterize the fracture and interface debonding of Si particles in an AlSi alloy has been developed, which combining a nanoindentation experiment and a finite element analysis. The dependence of indentation response on the interface strength and Si particle fracture was systematically studied from the threshold stress for the sink-in of the Si particles. An indentation map showing the Al/Si interface debonding, Si particle fracture and Al matrix plastic deformation has been constructed.

To

my dear wife and son, Yan and Evan

for their grateful devotion and support

ACKNOWLEDGEMENTS

Sincere thanks have to be expressed to Dr. Vesselin Stoilov and Dr. Xueyuan Nie, for providing me with the opportunity to work on this project under their excellent supervision. I am grateful to them for their great encouragement and endless support for the research.

I would like to acknowledge Dr. Qi Yang of Institute for Aerospace Research, for the nanoindentation tests. I would like to extend my sincerest gratitude to my committee members for their useful comments that helped to improve the final copy of the thesis.

Thanks are also due to Mr. John Robinson for his generous help in technical assistance and sample preparation.

Sincere thanks are extended to the group members, Ms. Linlin Wang and Mr. Peng Zhang for their help and advice. Thanks also to everyone in the MAME Department who has offered me encouragement and support during the course of my study.

National Science and Engineering Research Council (NSERC) and Ontario Centre of Excellence (OCE) are greatly appreciated for the financial support.

TABLE OF CONTENTS

LIST OF TABLES

LIST OF FIGURES

CHAPTER 1 INTRODUCTION

To reduce fuel consumption and CO_2 emission, it is becoming increasingly important to reduce vehicle weight. For such an objective, AlSi alloys such as Al 356 and Al 390 [1] have been commercially used to produce engine blocks due to their high strength over weight ratio. The engine block cylinder works under mechanical and thermal cyclic stresses in relative motion with piston rings. Therefore good wear resistance is a critical property to engine block life.

Wear is a complex surface/interface process in which several physical and chemical reactions take place depending on materials, tribological conditions such as different testing geometry, sliding load and sliding speed as well as the environment etc. Sliding wear under dry (unlubricated) state produces large plastic strain near the worn surface. Not only does the material removal may occur on both the wear surface and the counterface, but large subsurface strains and plastic deformation gradients can also be generated in the subsurface below the worn surfaces[2-5]. Studies have been carried out under unlubricated conditions to investigate adhesion at the surface, formation of protective mechanical mixed layers in the near surface, severe plastic flow in the subsurface. The high shear and compressive stress in association with frictional heating during wear processes, could induce several events in the worn surface and subsurface, such as work hardening[2], recrystallization (static or dynamic) [3, 4], deformation texture [5], strain-induced phase transformation [6] and delamination [7].

For AlSi alloys, the near surface plastic flow was found to cause fragmentation of silicon particles [8-12]. Fragmentations of the particles near the surface have also been found to be the source of crack nucleation and propagation under traction [13, 14]. Delamination [7, 15] wear has been the one of consequences of such activities of the subsurface layers (10-100μm) below the contact interface. Such deformation induces significant stresses within and between the grains/inclusions in the polycrystalline materials. These stresses in turn lead to relative movements between the grains/inclusions, as well as their fracture. The overall result is a dynamic change of the subsurface structure of the materials in

contact. The change of the structure leads to change of the tribological properties of the material, which are of primary importance for its performance. Several authors have experimentally investigated the subsurface layer deformation [7, 15-19] in Al alloys. Alpas et al. [7] have demonstrated that there is an exponential relationship between accumulated strain and depth below the worn surface. Similar result has been obtained by Perrin and Rainforth [19] for Al-Cu and Al-Si alloys. However, despite the intensive research in this area, the mechanism of crack formation and delamination leading to local structure refinement is still under studying.

Since more than two sliding components are involved in a sliding system, a mutual transfer and mechanical mixing of materials from the counterparts are often observed in the worn surface. After the transfer occurs and mechanically mixed layer is formed, wear behavior of the material is altered due to the distinct features of the mixed layers as compared to the original material. Therefore, problems associated with friction and wear are complicated, and many of them are still open to investigations with respect to a deep understanding of wear mechanisms of materials.

Wear phenomenon and wear mechanisms involved in the wear process could be further complicated for multiphase materials owing to the addition of secondary particles. Under certain conditions (load, sliding velocity etc.), wear of a metal matrix composite can be treated as three-body abrasive system (the Metal Matrix Composite, sliding counterface and the fragmented particles) as the hard particles are forced away from the matrix and get settled in the wear track during wear. There have been a number of investigations and reviews [20-23] concerning the wear behavior of Metal Matrix Composites (MMCs) in which an improved wear resistance has been reported. However, wear mechanisms of these multiphase materials are still being investigated due to complications resulting from the addition of the reinforcing phases, especially on microstructural features of the top worn surfaces and microstructural evolutions along the depth below the worn surfaces. In Al alloys and Al based metal matrix composites, for example, formation of a mechanically mixed layer (MML) is generally found, which is reported to be comprised of materials from the sliding surface and the counterpart [24-26]. Depending on different

experimental conditions under which wear tests were conducted, there are differences of the formation mechanism of the MML between different observations. Some researchers reported that the mixed layer was mainly comprised of oxides [25], and others found little or no oxide in the mixed layer [27]. Clearly, there is no uniform wear mechanism applicable for different applications.

To improve the wear and scuffing resistance, liner-less engine blocks made of a hypereutectic and near-eutectic AlSi alloy typically require a chemical surface preparation that results in the hard Si particles are exposed on the surface to bear the load, prevent adhesion to the Al matrix, and resist damage [28]. The topography of the AlSi alloys surfaces has triggered the idea that the silicon particles form a load bearing surface over which the counter surfaces are sliding. Therefore the wear resistance of AlSi surface is thought to originate from the high hardness of the silicon surface formed by the primary Si particles (inclusions). Recently, microstructural characteristics of sliding wear behavior were carried out with lubrication to study the origin of wear resistance under ultra-mild wear in AlSi alloys for engine cylinder bore surfaces [29-33]. Unlike conventional mass-loss-based wear conditions under high load, the piston-cylinder block assembly in automotive engines must operate under the conditions of ultra-mild wear (UMW) which with a wear rate not exceed a few nanometers for each running hour [34]. For instance, the wear rate of a piston-cylinder block assembly with lubrication working in a fired engine dynamometer was measured on-line using radionuclide-technique (RNT) and was below 20 nm/h for all operating conditions, at partial load well below 10 nm/h [33]. However, sink-in and fracture of Si particles were still observed in such studies under UMW. The experimental observations [18, 35-37] have collectively showed that the vicinity of the inclusion/matrix interface is usually the starting point of the cracks and the interface decohesion observed in the AlSi alloys. Therefore the interface strength of Al/Si plays a key role for in sink-in mechanism and needed to be studied. The fracture mechanism of Si particles is also important for forming a mechanically mixed layer.

Al/Si interfaces can be found in AlSi composites in many different forms. AlSi alloy is considered as an “in-situ composite”, since the Si particle reinforced Al composite is

formed during casting process. The typical microstructure is the eutectic Si particles with size ~10μm surrounded by large Al grain as large as hundreds of microns. The applied far-field loading initiates severe plastic deformation in the Al matrix around the Si particles, which leads to formation of voids in the close vicinity of the matrix/inclusion interface. In turn, these voids have twofold effect on the evolution of the local microstructure: first, the presence of the voids induces high stress concentration within the stiffer Si particles [38-40]; and second, they initiate new crack nucleation inside the Al matrix. As a result, the Si particles fracture, facilitating matrix cracks coalescence and eventually causing the ultimate failure of the alloy [35-40]. These failure mechanisms are directly related to the strength of the Al/Si interface.

As the second phase particles fracture and debond, finite element calculations can be used to obtain the evolution of local stress and strain distributions with respect to the far field loading. Previous finite element studies have used cohesive zone approaches to study for example, inclusion debonding in ductile materials [41-43], dynamic crack propagation in brittle materials [44] and various other crack growth problems [45, 46]. However these studies focused on the influences of particle fracture under far field loading without considering the local particle fracture mechanism. For UMW applications, local debonding behavior of Al/Si interface and Si particle fracture near the surface are of our interests.

The present investigation was carried out with a primary objective of a deeper understanding of wear of two phase AlSi alloys in terms of their microstructural characteristics. In particular, the interface strength of Al/Si and facture mechanism of the primary Si particles were targeted for the investigation. Microstructural characterization of the studied materials were mainly conducted by using nanoindentation, scanning electron microscopy (SEM), scanning probe microscopy (SPM), serial sectioning and other physical and metallurgical methods. After that, FEM simulations were used to verify the analytical interface strength derived from molecular dynamics simulation [40] and investigate the fracture mechanism of Si particles and plastic deformation of Al matrix.

The thesis is divided into six chapters. In Chapter Two, the relevant literature is reviewed which is followed by materials and methodology in Chapter Three. The Al/Si interface strength under nanoindentation and microstructural characterization are presented and discussed in Chapter Four. Chapter Five is dedicated to FEM analysis of Si inclusion/Al matrix system. Finally, a summary of the thesis and future work are given in Chapter Six.

CHAPTER 2 LITERATURE REVIEW

2.1 Wear

2.1.1 Definition and Mechanisms of Wear

In general, wear may be defined as damage to a solid surface caused by the removal or displacement of material by the mechanical action of a contacting solid, liquid, or gas. Wear process generally involves progressive loss of materials from at least one of the contacting components and loose wear debris may be generated. Wear process can also take place without removal of materials, and only material displacement and plastic deformation occur in the surface and subsurface during the wear process accompanying some changes in shape and/or properties [47].

Wear has been classified in various ways. It is common to classify types of wear in terms of different relative motions such as sliding wear, rolling wear, impact wear and lubricated/unlubricated (dry) wear and so on (Fig. 2.1) [48]. These processes act on the surfaces in the relative motion either independently or cooperatively, for example, abrasion in a corrosive medium. Another possibility is to classify wear on the basis of the fundamental mechanism that is operating as shown in Fig. 2.2 [49]. Unfortunately, this approach is complicated by the fact that more than one mechanism may be operating at the same time and by the fact that those developing wear classification schemes have come from different backgrounds and experiences with wear. Therefore wear mechanisms could be different under different conditions. To date, many wear mechanisms have been proposed to address the wear phenomenon, and it seems almost impossible that a single wear mechanism can be expected to be responsible for wear of materials.

Following an initial suggestion by Tabor [50], Lim and Ashby [51] constructed the first wear mechanism maps which show the wear rate and the dominant wear regimes including delamination, mild and severe oxidation, melting and seizure wear, in dry sliding wear system of steels. The diagram can be constructed empirically (ie., from experimental data alone) and by modeling (by theoretical analysis calibrated to

experiments). They obtained the wear rate mechanism map for a steel by using the oxidation wear theory together with thermal analysis of sliding contact, as shown in Fig. 2.3.

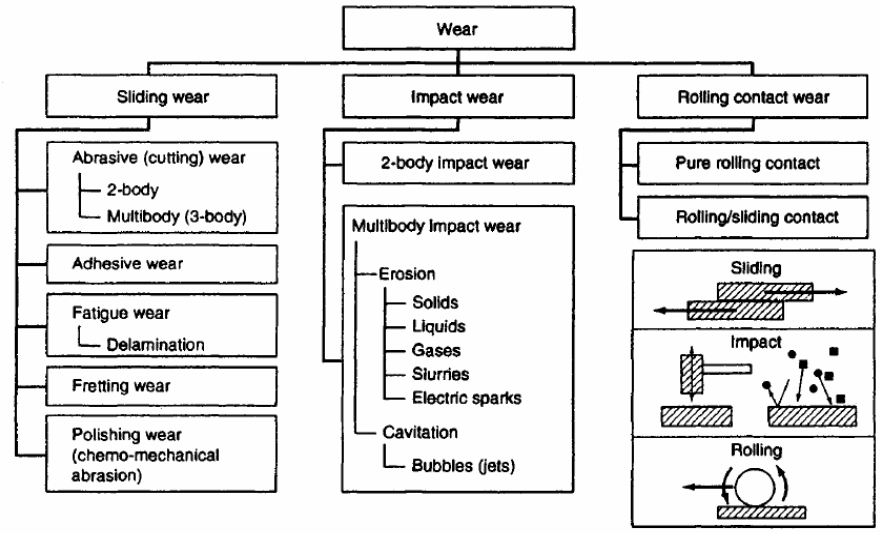

Fig. 2.1 Categories of wear classified by the type of relative motion [48].

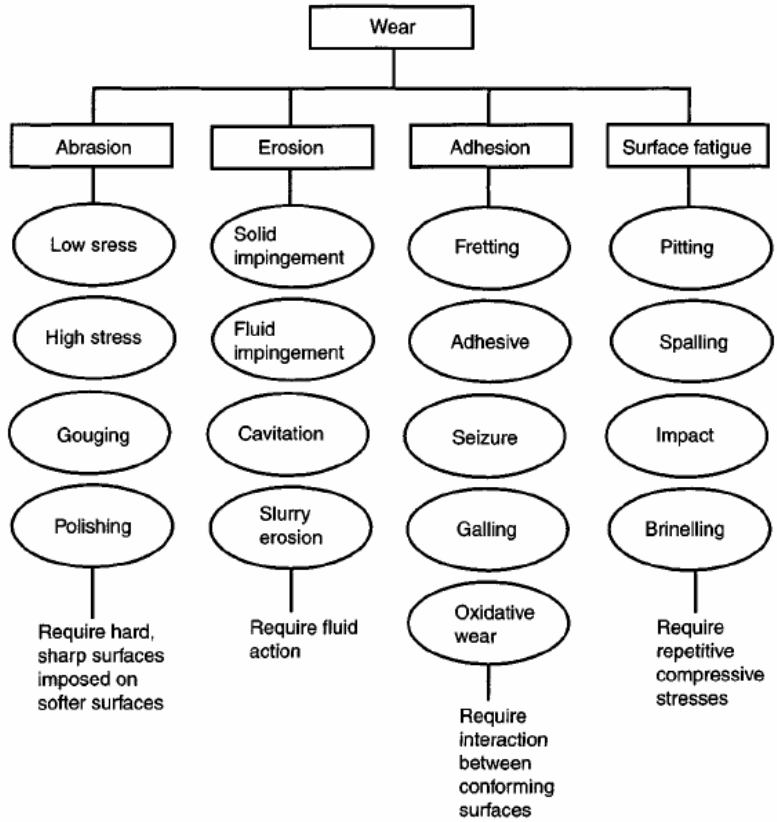

Fig. 2.2 Categories of wear classified by the fundamental mechanisms [49].

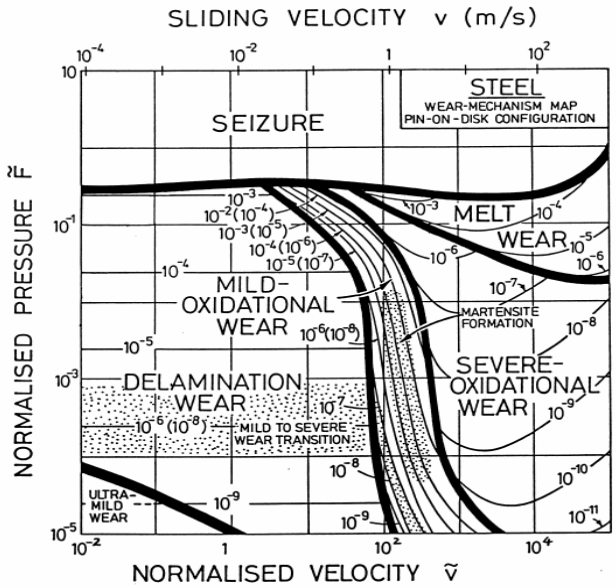

Fig. 2.3 The wear mechanism map for a steel sliding pair using a pin-on-disk configuration [51].

In Fig. 2.3, contours of constant normalized wear rates are superimposed on fields showing the regimes of dominances of different wear mechanisms. There are discontinuities in the contours where they cross the field boundaries into the regimes of severe oxidation wear and melting wear. The wear rates given in parentheses are the values when mild wear takes place and the shaded area indicates a transition between mild and severe wear. A review of the development of mostly sliding wear maps for metals, ceramics, metal-matrix composites and polymers has been given by Lim [52]. These maps describing the wear of coatings, tool wear, fretting wear, erosion and time-dependent wear transitions are then introduced.

Following the same methodology used in constructing the maps for steels, a wear-mechanism map (Fig. 2.4) for the unlubricated sliding of aluminium and aluminium alloys on steel was later proposed by Liu et al. [53]. This map is a considerable improvement over the earlier empirical wear map for the same group of alloys presented by Antoniou and Subramanian [54]. New model equations based on a different state-of-stress criterion suitable for aluminium alloys have been developed by Liu et al. and found to match well with reported experimental wear data (marks in Fig. 2.4) on aluminium alloys.

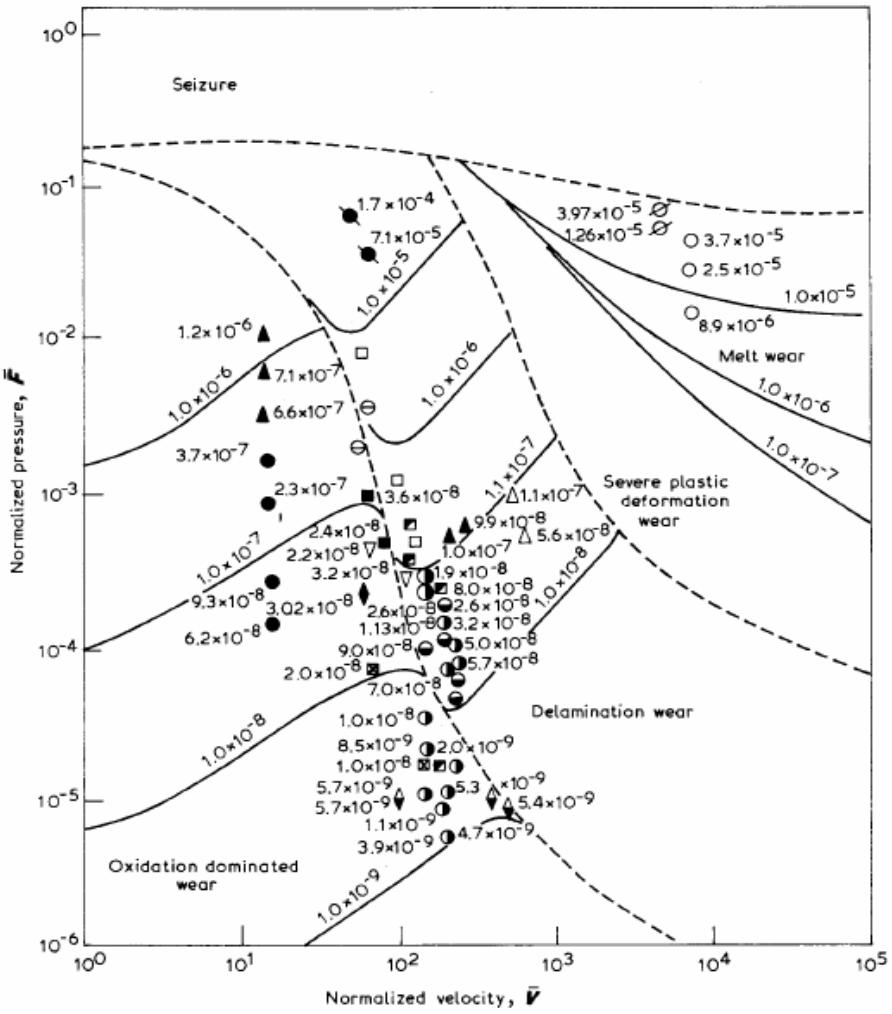

Fig. 2.4 A wear mechanism map in aluminium alloys [53].

2.1.2 Stress Distribution

The conditions of sliding wear, especially in dry (unlubricated) state, produce large plastic strains at and near the wear surface. Not only does the material removal occur on both the wear surface and the counterface, but large subsurface strains and plastic deformations can also be generated near the worn surfaces [47, 55-58]. Several researchers have emphasized the contribution of surface strains and plastic deformation to wear, either developing and modifying [55] or challenging [59] the adhesive theory. Moore and Douthwaite [55] studied the worn surface focusing on large plastic strains observed at considerable distances from the wear surface, and they suggested that because of strain hardening, an extensive region below the worn surface was also deformed plastically and a large part of the energy expended in the sliding wear might be

expected to be absorbed by the plastic deformation. Many investigations [3, 25, 55, 58, 60] have discussed plastic shear strain as a function of depth in the worn surface in a number of ways, such as measurement of deviation of plastic flow from being normal to the worn surface by using a marker technique [55, 58], and microhardness depth profile obtained on the cross section of the worn surface.

2.1.3 Transfer and Mechanical Mixture of Materials

Transfer of materials from one sliding surface to another occurs in a sliding system either in lubricated or unlubricated conditions. A number of investigations have dealt with the mechanically mixed or alloyed layer generated by sliding wear in the extreme wear surface [61-66] using SEM and EDS techniques. Since the mixed layer is located on the top surface and may directly contribute to the formation of wear debris, it is important to understand the formation mechanisms and characteristics of mixing layers.

Antoniou and Borland [27] and Subramanian [67] have discussed the characteristics of mechanical mixing in sliding wear system of AlSi binary alloys. Based on their experiment conducted in a pin-on-disk dry sliding condition at a sliding speed 0.1 m/s, applied pressure range of 0.1-5 MPa, they found that there were two processes which were important in mechanical mixing or alloying: (i) debris removal from the wearing interface and (ii) debris particles reprocessing at the wearing surface. The wear surfaces were protected by the formation of the mixed layer and thus resulted in a lower wear rate. They also found that the formation of the mixed layer was a product of a certain combination of the normal loads and sliding speed, i.e., high load and low speed. There was no mechanical mixing either at high loads or at high speeds. Li and Tandon [68] have investigated mechanically mixed layer of Al–Si alloys sliding against a tool steel using scanning electron microscopy and transmission electron microscopy with energy dispersive spectroscopy and X-ray mapping. They found that the mixed layers and wear debris had similar microstructural features and were comprised of mixtures of ultrafine grained structures, in which the constituents vary depending on the sliding loads. At a low load, the ultrafine structures mainly consisted of the original base materials, i.e., α-Al solid solution and α-Fe from the steel. With an increase in sliding load, the ultrafine

structures were incorporated with Fe-Al(Si) intermetallic compounds and aluminum oxides.

Alpas and Zhang [24], Feng and Tandon [63] and others [25] have found similar mechanical mixing layer in the sliding wear of the MMCs. Not only did the mechanical mixing layer occur in the matrix, but the reinforced particles were fragmented and redistributed in the mixed layer as well. Similarly, the occurrence of the mixed layer was mainly dependent on the normal load and sliding speed. In MMCs, incorporation of the reinforced particles is considered as an enhancement to the formation of the mixed layer during sliding wear [63]. The abrasive action of the hard particles resulted in debris fragments and some loose debris deposited on the contact surface of the composite. As a result, an oxidized mixed layer was formed by an association of strain and friction heating during the sliding Wear.

The mechanically mixed layer was also found in the bore surface of an AlSi alloy engine block with lubricant by Dienwiebel et al [33]. The engine block had been operated in a fired engine dynamometer test of 250 h over the full speed and torque range of the engine using a commercially available, fully formulated engine oil. Wear debris from various sources were embedded and mixed into the soft aluminium matrix. There they led to an increase of the shear strength of the mixed layer.

2.1.4 Metal Matrix Composites

Modern composite materials are referred to as advanced materials in which two or more components are combined on a macroscopic and/or microscopic scale. These materials can be tailored to take advantage of the desirable properties and minimize the undesirable properties of their constituents. Consequently, composite materials often exhibit some qualities that their constituents do no possess individually. Metal Matrix Composites (MMCs) are comprised of a metal matrix and reinforcements such as fiber, whisker and particulate ceramics which are incorporated in the matrix in order to provide enhancement in properties such as strength, stiffness, and temperature-dependent strength,

wear resistance, as well as modifications of the thermal expansion and electrical conductivity.

The modulus of the MMCs is found to be always significantly increased by addition of reinforcement. The volume fraction of reinforcement is the dominant factor in increasing the modulus of elasticity. For a given fraction of reinforcement, the modulus tends to be isotropic with nearly equal values obtained from tests in the longitudinal and transverse directions. Moreover, the modulus appears to be insensitive to the type of reinforcement used. The modulus is also independent of the matrix alloy, but heat treatment may have a slight effect upon it. The yield strength or ultimate tensile stress (UTS) of the MMCs is generally found to be higher as compared to the base alloys. The strengthening mechanisms of the particulate reinforced MMCs have been studied by a number of investigators [69-72].

The ability to transfer stress from the matrix to the reinforcing particles is also critical to the strengthening of the MMCs. As a composite is loaded, the matrix in the vicinity of the stronger reinforcing particles is able to transfer a portion of the load to the particles [73]. This effect can be seen from the fact that an increase in elastic modulus is found in composites compared to the unreinforced alloys. The load transfer, however, is dependent upon a stronger interfacial bond between the reinforcement and the matrix. To a large extent, an increase in the mechanical properties the MMCs is determined by the structure and properties of the interface. Therefore, a number of studies have been conducted on microstructures and properties of the interface including interface reaction [10, 74, 75], crystallographic relationships and interface precipitation [76].

2.1.5 Wear of Al alloys and Al Based MMCs

Deformation structures are complex in the worn surface, which could get further complicated during the sliding wear of ductile composite metallic materials reinforced with hard second phase particles owing to the presence of the hard particles. In research reported by Reddy et al. [77] three distinct wear regimes were identified as a function of

applied load in AlSi alloys. These wear regimes are discussed below and presented in Fig. 2.5:

- Mild wear. At low loads, the worn surface was characterized by the formation of an iron-rich compacted debris layer. Wear debris formed in this regime was a result of abrasion and cracking of this protective layer with a significant proportion of this debris again added to the compacted layer.
- Severe wear. As load increased, a delamination type wear mechanism was operative in which sub-surface deformation and cracking caused fragmentation of the Si particles and removal of the iron-rich protective layer resulting in a high wear rate.
- Seizure wear. In this wear regime, near surface temperatures were high enough to lower the shear strength in the sub-surface layer and promoted extensive material transfer from the wearing alloy to the steel counterface.

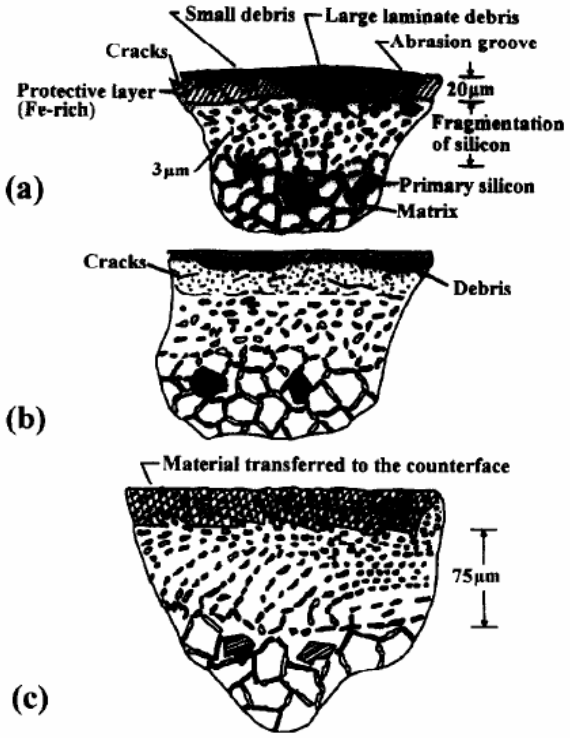

Fig. 2.5 Schematic diagram of the following wear processes in Al-Si alloys: (a) mild wear, (b) severe wear and (c) seizure [77].

Wear behavior of the Al composites at elevated temperatures is also an important issue since many high temperature tribological applications of these composites are found, for example, some engine components. Only limited investigations of the influence of ambient temperature on wear performance have been reported [78-81]. Martin et al [79] and Martinez et a1 [78] studied wear behavior of an Al-Si/SiCp composite and an eutectic Al-Si alloy at ambient and elevated temperatures (20 °C to 200 °C). They reported that at low temperatures the wear behavior was controlled by the eutectic Si or SiC particulate, and at high temperatures, on the other hand, the wear behavior was controlled by the matrix which underwent large plastic deformations. Both materials experienced a transition temperature at which wear mechanisms changed from mild to severe wear with an increase in temperature, and the transition temperature was increased by the addition of SiC particles. Therefore, they concluded that the main effect of the SiC reinforcement on the sliding wear at high temperatures was to delay the transition from mild to severe wear by about 50 °C. Similarly, Wilson and Alpas [80] investigated the effect of ambient temperature on wear performance of A356 Al and 6061 Al composites in comparison with their base alloys. They found that the reinforcements increased the transition of wear mechanisms from mild wear to severe wear into high temperature and the increase could be 100-200°C higher than that in the unreinforced alloys. They attributed the increase to formation of protective transfer layers of comminuted reinforcing particles and transferred steel debris from slider counterfaces.

2.2 Ultra Mild Wear in Aluminium Alloys

To optimize the power-to-weight ratio, aluminum alloys are used to replace traditional cast iron cylinder liners and cylinders. The chemistry and microstructure of such alloys, from the above consideration, should minimize wear of cylinder surface under realistic pressure and velocity conditions. In order to achieve this objective, it is of great importance to understand the mechanism of wear under these conditions. The levels of wear rates of piston–cylinder bore assemblies which normally run under lubricated conditions, should not exceed a few nanometers per hour (or approximately 0.1Å per cycle) [34]. Such wear with low wear rates are defined as Ultra Mild Wear (UMW). The research of lubricated sliding of aluminium alloys under UMW is quite limited. Das et al

[31] investigated pin-on-disk sliding on a 13% Si AlSi alloy under lubricated condition in the 1~100 MPa mean contact pressure range and 0.2 m/s sliding speed. They found two transition in wear rate, at 10 MPa and 70 MPa and the wear rate in the 1~10 MPa regime was found to be very small and within the measuring instrument resolution and also insensitive to contact pressure (Fig. 2.6). The regime is designated as UMW.

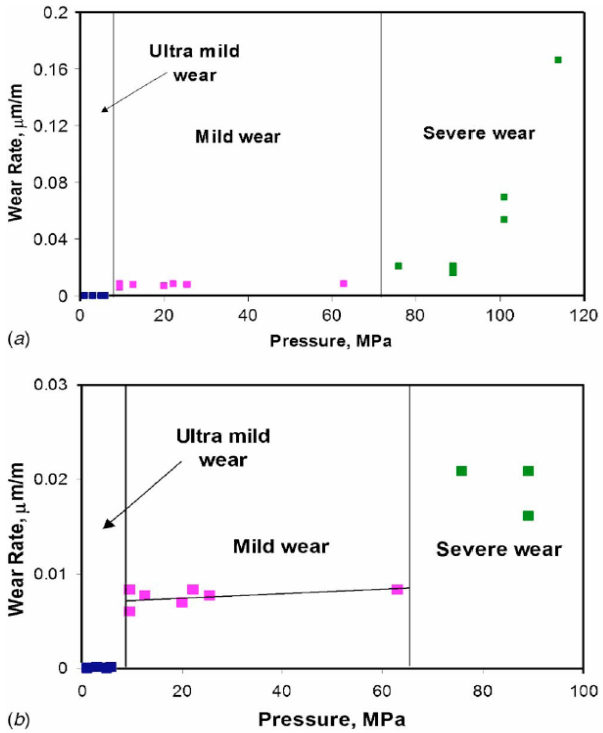

Fig. 2.6 (a) Steady-state wear rate as a function of mean contact pressure indicating three wear regimes: ultra mild wear, mild wear, and severe wear. (b) Expanded view to show mild wear regime more explicitly [31].

Microscopic observation of subsurface damage in slid samples indicated that elastic state prevails in the steady-state UMW regime. In the mild wear regime, there was an initiation of plastic flow. With the higher load, plasticity dominated in the severe wear regime. Noticeable, after a run-in process, a mechanically mixed layer of ~1 μm has been occasionally formed at the surface. Voids at the Al/Si interface within 2~3 μm of the surface and fractured Si particles were observed as shown in Fig. 2.7. There is also further refinement of the Al subgrain size with respect to the run-in sample.

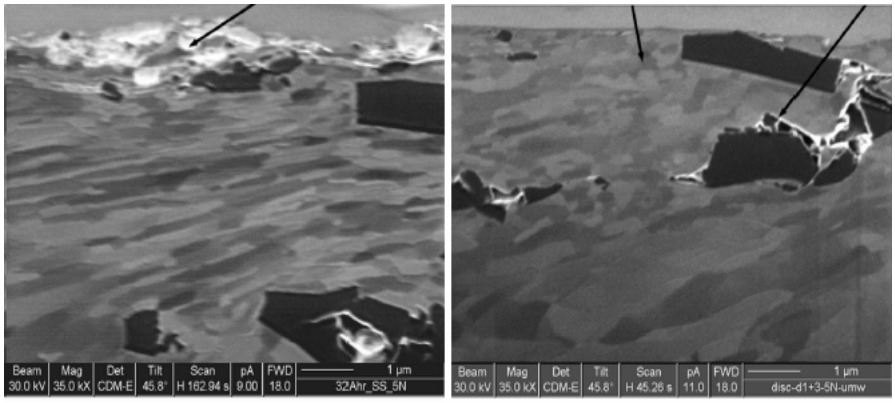

Fig. 2.7 FIB images of an UMW sample (mean contact pressure=0.32 MPa): (a) one area of the subsurface which shows mechanically mixed layer, (b) one area of the subsurface that shows voids at the Al-Si interface when silicon is unfractured and in the cleaved gap in fractured silicon particles [31].

Chen and Alpas [32] reported UMW mechanisms in a Al-25% Si alloy consist of three stages as shown in Fig. 2.8.

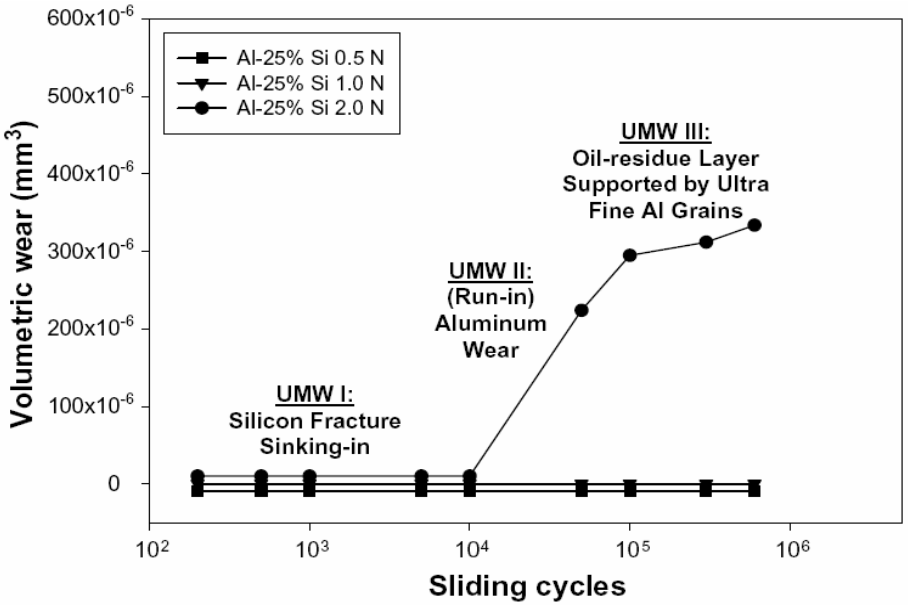

Fig. 2.8 Variation of volumetric loss with sliding cycles showing the three stages of UMW in Al–25% Si [32].

In UMW I, wear at the top surfaces of silicon particles occurred along with particle fracture and particle sinking-in (Fig. 2.9). Damage was limited to the silicon particles. During UMW I, the aluminum matrix remained protected. In UMW II, the aluminum was no longer sheltered and measurable quantities of material loss occurred, which is a period

of rapid wear (or run-in). UMW II was not persistent, and eventually the rate of damage decreased. This decrease was coincident with the formation of an oil residue layer (Fig. 2.9d) on the contact surface as well as the formation of a subsurface structure consisting of ultra-fine aluminum grains. This is the regime depicted in Fig. 2.8 as UMW III. Similar to the study of Das, voids and fracture Si particles plus the refinement of Al grains were observed as presented in Fig 2.10.

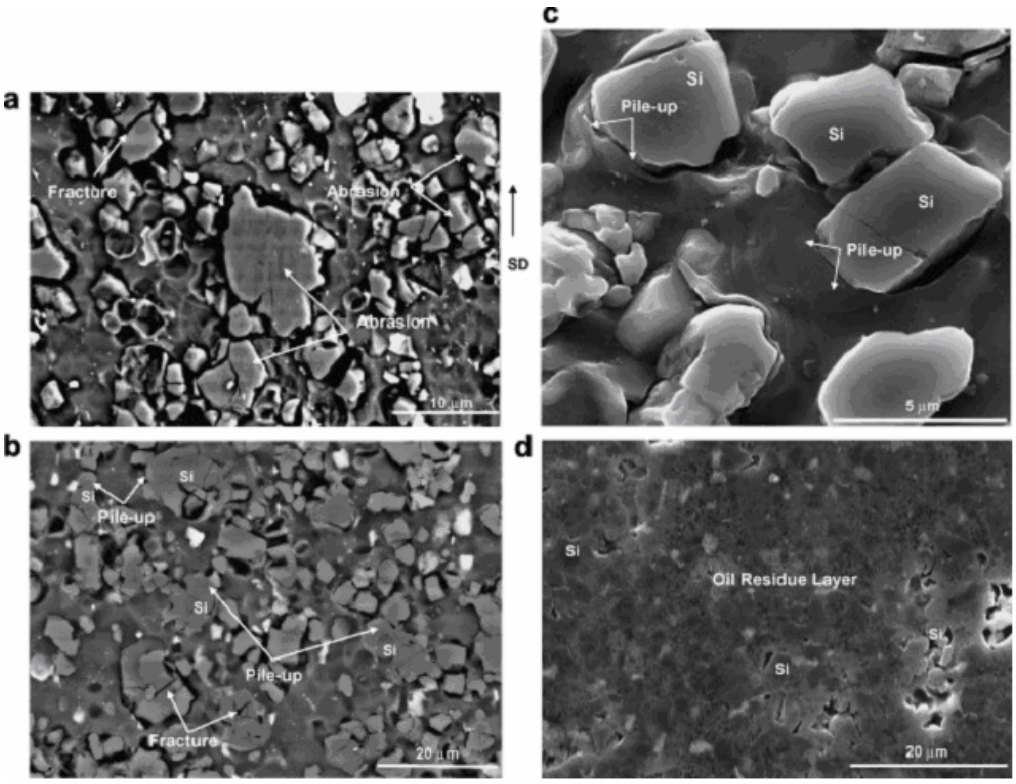

Fig. 2.9 Worn surface morphologies of Al–25% Si showing aluminium pile-up and Si fracture [32].

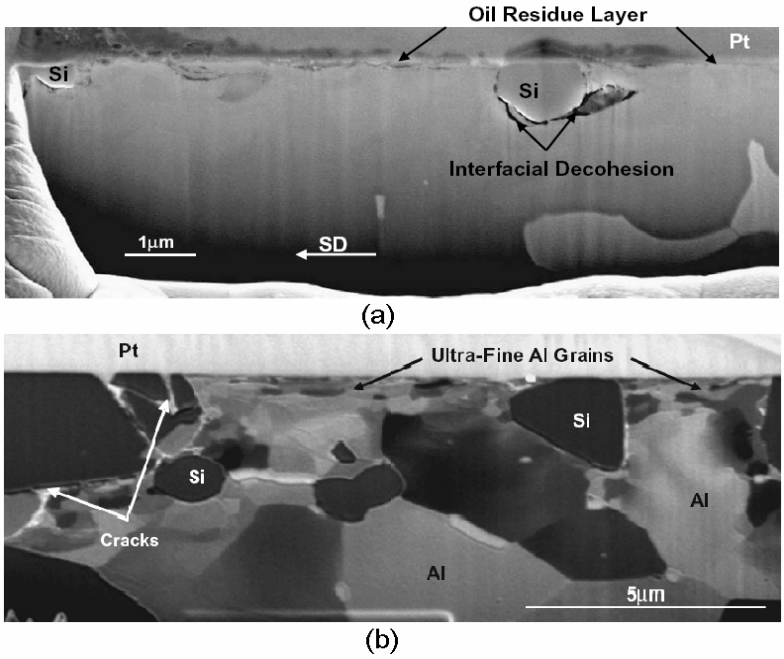

Fig. 2.10 Cross-sectional SEM image of the wear track of Al–25% Si showing (a) the oil residue layer on the contact surface, where damage to Si and at Al/Si;(b) ultra-fine aluminum grains around the silicon particle [32].

Dienwiebel et al [33] invested wear resistance of a AlSi alloy in an internal combustion engine. Surface analyses of the bore surface of an AlSi17Cu4Mg engine block has been carried out after operating in a fired engine dynamometer test of approx 250 h over the full speed and torque range of the engine. The wear rate was measured on-line using radionuclide-technique (RNT) and was below 20 nm/h for all operating conditions, at partial load well below 10nm/h. The wear rate is acceptable to achieve a typical service life. Although Si particles protruded 700~800 nm above Al matrix at initial stage, radioactive wear particles mainly aluminium were detected by RNT in the engine oil at the very beginning of operation. After a short running-in, Si particles and Al matrix were at the same height level. Dienwiebel et al. proposed a new energetic wear model for the system of piston ring/hypereutectic AlSi cylinder bore. Based on the fact that the Al matrix is strongly modified during running-in, a friction induced wear particle dispersion strengthening process is made responsible for the enhancement of the wear resistance of the aluminium (Fig. 2.11). Due to the dissipated energy during sliding, wear particles from various sources such as fracture Si particles are embedded and mixed into the soft

aluminium matrix. There they lead to an increase of the shear strength of the material. Dienwiebel et al. suggested that the initial protrusion of Si primary particles is necessary to direct the energy input into the Si grains in order to initiate a sintering process with Si wear particles and to separate the piston ring from the initial nascent Al surface. After running-in Si particles are not necessary to provide the load-bearing capacity. Again, many voids are present under Si wear particles as shown in Fig. 2.12.

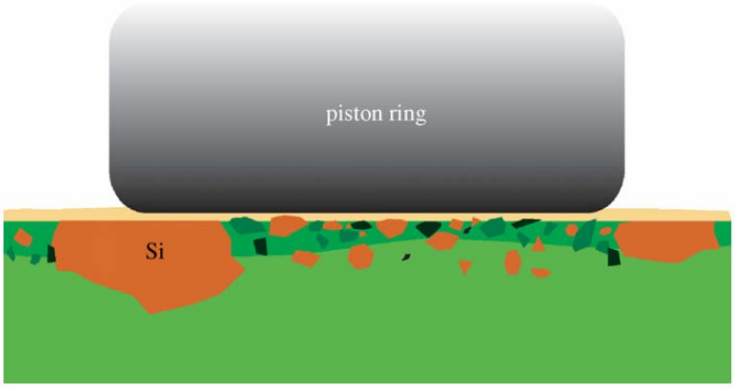

Fig. 2.11 Schematic of a friction induced wear particle dispersion strengthening wear model [33].

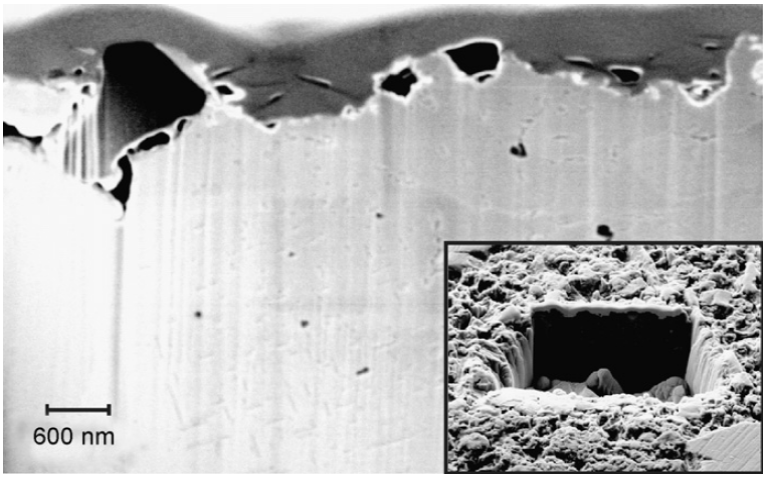

Fig. 2.12 Cross section of the worn Al matrix using focused ion beam milling. Small Si particles (dark grey) are found embedded into the aluminium matrix during operation since their surface is entirely oxidized (due to charging effects the oxide layer appears as a white rim at the surface) [33].

The observation of microstructure of near surface regime of AlSi by Dienwiebel, Das and Chen reveal that the Al/Si interface strength and fracture of Si particles play key roles on wear properties in the UMW regime. However, the interface strength and particle fracture mechanism are far from clear and further studies are needed.

2.3 Molecular Dynamics Study of Al/Si interface strength

The interface plays an important role in controlling deformation and fracture. Previous Modified Embedded Atom Method (MEAM) simulations on AlSi interfaces [82-84] are mainly focused on interface decohesion under tensile load and provided insightful but somewhat limited results. For example, Gall et al. [82] determined the traction-displacement relationship of the AlSi interface for fixed orientation ($[100]_{Al}[100]_{Si}$) under tensile loading. However, such studies have not considered the effects of different crystals orientation and dislocations on the strength of the interface. In order to develop an accurate cohesive zone model, a more thorough study of the effects mentioned above has been carried out by Noreyan et al [40]. Noreyan et al developed an atomic level model of contact interface between the matrix (Al) and the inclusion (Si) with shear loading. The atomic level model was based on molecular dynamics (MD) simulation using the Modified Embedded Atom Method (MEAM) potential [85] and the Verlet integration algorithm [86]. In addition, the effect of different orientations of the Al and Si crystals and local temperature has been considered. Fig. 2.13 shows the atomic structure of the typical simulation cell and the settings for the applied shear loading. Simulation results are given in Fig. 2.14 and the applied threshold stress of Al/Si interface using molecular dynamic simulations is between 318 MPa and 1.172 GPa (Table 2.1).

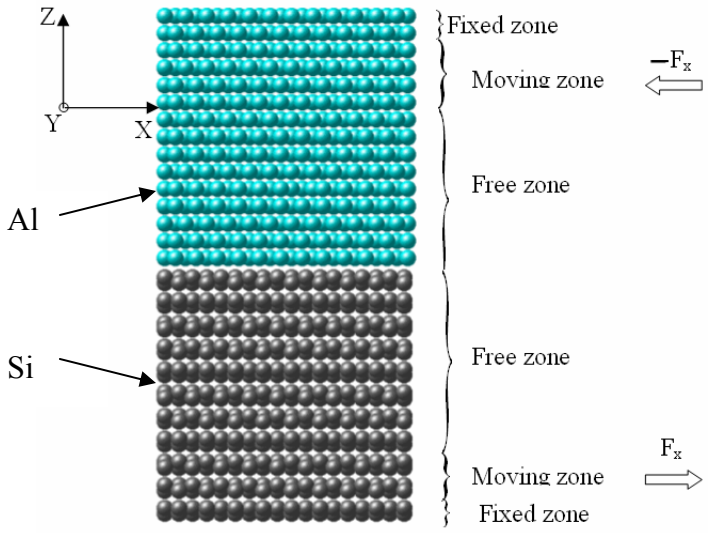

Fig. 2.13 Simulation cell for Al(111)/Si(111) interface: In shear loading simulations, the workpiece is divided into three zones for Al and Si, and the external forces/strains are applied to atoms in moving zone [40].

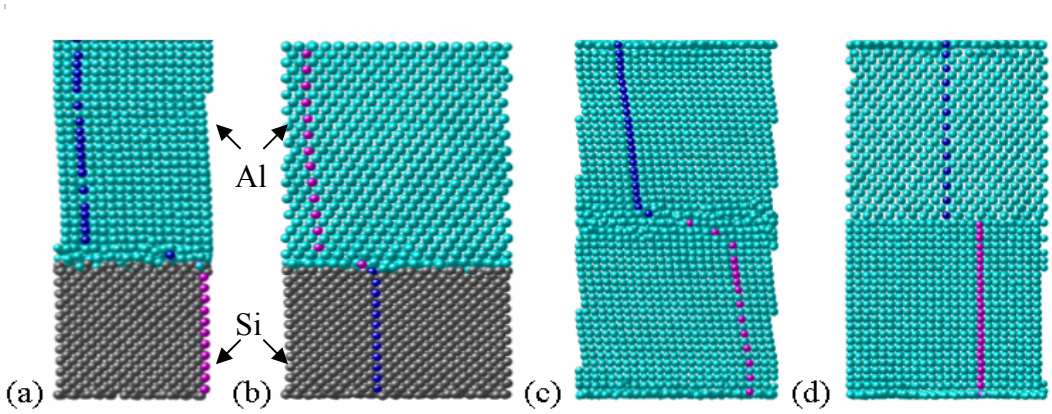

Fig. 2.14 Snapshots of simulations cells after shearing for a) Si(001)<100> ||Al(001)<100> for applied strain rate of 1 Å/ps, b) Si(001)<100>||Al(001)<110> applied force of 0.02 eV/Å, c) Al(001)<100>||Al(001)<100> for applied force of 0.05 eV/Å, d) Al(001)<100>||Al(001)<110> for applied force of 0.002 eV/Å. All the highlighted atoms were aligned before sliding [40].

Interface	Applied threshold force for initiating sliding at interface eV/ Å (N)	Applied threshold stress (GPa)	Al/Si Tensile strength (GPa)
Si(001)<100>||Al(001)<100>	0.015 ± 0.0005 *(~2.48 × 10^{-11})*	1.172 ± 0.04	6.4
Si(001)<100>||Al(001)<110>	0.0145 ± 0.0005 *(~2.32× 10^{-11})*	1.136 ± 0.039	-
Si(001)<100>||Al(111)< 1 $\bar{1}$ 0>	0.0075 ± 0.0005 *(~1.2× 10^{-11})*	0.657 ± 0.044	5.6
Si(111)<1 $\bar{1}$ 0>||Al(111)< 1 $\bar{1}$ 0>	0.0035 ± 0.0005 *(~5.6 × 10^{-12})*	0.318 ± 0.045	7.2

Table 2.1. Threshold forces and critical shear stresses of Al/Si interface [40].

2.4 Fracture Toughness

Fracture toughness is a property which describes the ability of a material containing a flaw to resist fracture. Flaws may appear as cracks, voids, metallurgical inclusions, weld defects, design discontinuities or their combinations. There are three modes of fracture as illustrated in Fig. 2.15a.

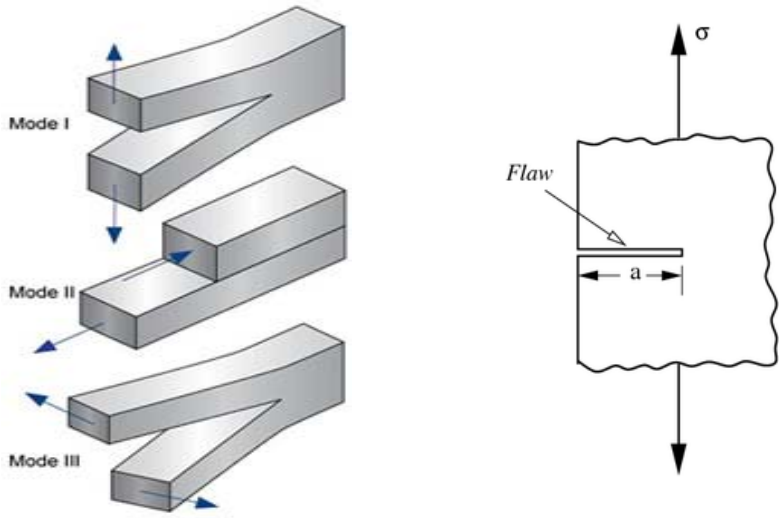

(a) (b)

Fig. 2.15 Three modes of fracture. (a) Three modes, (b) Mode I.

In this project, only Mode I fracture of Si particles is considered. The fracture toughness is expressed as,

$$K_{IC} = Y\sigma\sqrt{\pi a} \tag{2.1}$$

where K_{IC} is Mode I fracture toughness, σ is applied stress, a is crack depth, Y is a geometric constant, generally Y=1.

Fracture toughness of the MMCs is considered as the work of fracture, i.e., the dissipation of elastic energy imposed in the specimen by the externally applied load per unit of new crack surface formed. As a crack grows rapidly through the particulate reinforced composite, many events occur that are potentially related to the fracture toughness, and each of these either makes it easier or harder for the crack to extend. The events were summarized by Davidson [87] as shown in Fig. 2.16. These main mechanisms associated with fracture of the MMCs with respect to the above aspects. As we can see from Fig. 2.5, the energy dissipated around a propagating crack tip of a SiC particle in a MMC is satisfactory with the elastic energy consideration regarding the fracture toughness, but a crack tip in the ductile matrix is readily associated with plastic deformation.

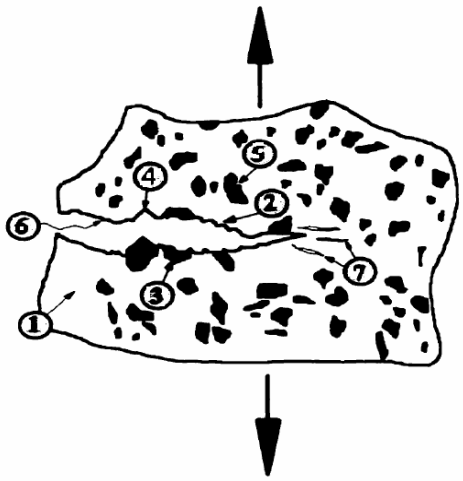

Fig. 2.16 Schematic illustration of events of fracture of MMCs reinforced with particulate. (1) deformation within plastic zone; (2) formation of voids along fracture surface; (3) fracture of SiC particles along crack path; (4) interfacial separation between matrix and SiC; (5) fracture of SiC within the plastic zone; (6) tortuous fracture path increase fracture surface area; (7) matrix cracks near, but not continuous with, the main crack [87].

2.5 Instrumented Nanoindentation Technique

To experimentally verify the above mentioned numerical simulation model by Noreyan et al., nano indentation tests are designed to carry out in AlSi alloys. Instrumented

indentation technique has become popular as it provides a continuous record of the variation of indentation load, P, as a function of the depth of penetration, h, into the indented specimen, from which mechanical properties such as hardness, elastic modulus, yield strength and strain hardening exponent can be estimated [88, 89]. In an instrumented indentation test, the indenter is driven into a specific site of the material to be tested by applying an increased normal load [Fig. 2.17a]. Upon reaching a prescribed value, the normal load is removed. The position of the indenter relative to the sample surface is precisely monitored. For each loading/unloading cycle, the applied load is recorded against the corresponding position of the indenter [Fig. 2.17b]. The resulted load/depth curve provides data specific to the mechanical nature of the material under examination. Well established models can be used to obtain the hardness and modulus of the material [90].

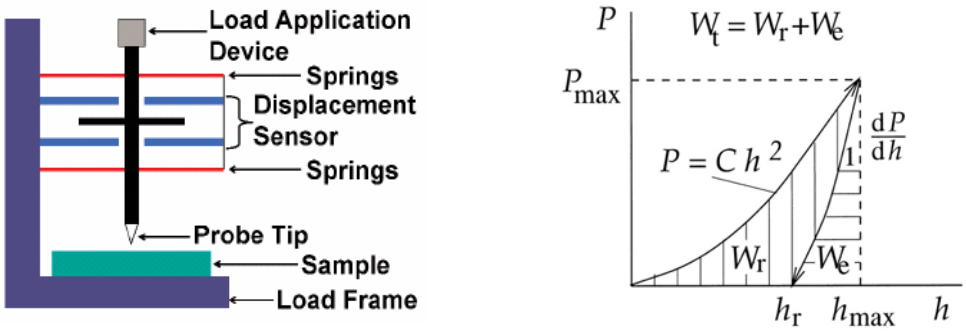

(a) (b)

Fig. 2.17 Indentation for hardness and modulus measurements [90]. (a) Illustration of instrumented indentation test; (b) typical result.

In this project, the Oliver-Pharr method [91] was applied to acquire hardness and elastic modulus. Fig. 2.17(b) schematically shows an indentation load-depth curve with a sharp indenter. The indentation load increases at a constant rate and leads to a nonlinear increase of the penetration depth. h_{max} is the maximum depth at the maximum load P_{max}. The curve follows the Kick's law, i.e., $P = Ch^2$, where C is the indentation curvature. Kick's Law is not valid in the rate-dependent cases as the loading rate, and thus the material strength, varies during the impact. When the material response is rate-sensitive, C is not a constant and instead varies with the loading rate. With a sharp indenter, the loading process is always elastic-plastic, while the unloading is basically elastic.

Hardness and some other material properties can be obtained from the load-depth curve. Hardness is normally defined as the mean contact pressure [91] and is given as,

$$H = \frac{P_{\max}}{A_p} \tag{2.2}$$

where A_p is the projected contact area at the maximum load (Fig. 2.18). For a perfect Berkovich indenter, $A_p = 24.56h_c^2$.

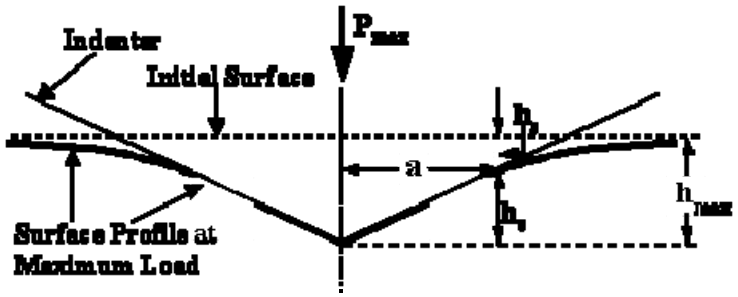

Fig. 2.18 Schematic representation of the indentation process. h_c is the contact depth, h_s is the depth of the surface at the perimeter of contact and a is the radius of the contact circle defined by the indenter.

Elastic modulus can also be determined by an indentation test. According to Oliver-Pharr method [91], the indentation modulus, E, can be calculated from the slope of the tangent of the unloading curve using a linear fit to the initial unloading data, i.e.,

$$E = \frac{1-\nu_s^2}{\frac{1}{E_r} - \frac{1-\nu_i^2}{E_i}} \tag{2.3}$$

where E_i is the elastic modulus of the indenter (1141 GPa for diamond), ν_i is the Poisson's ratio of the indenter (0.07 for diamond) and ν_s is the Poisson's ratio of the tested sample. The reduced modulus, E_r, is given by,

$$E_r = \frac{\sqrt{\pi}}{2\beta\sqrt{A}}\left(\frac{dP}{dh}\right) \tag{2.4}$$

where $S = dP/dh$ is experimentally measured stiffness of the upper portion of the unloading curve and β is a correction factor. For Berkovich indenter, β=1.034.

Pile-up and sink-in are the distinctive features in indentation experiments. The material around the contact area tends to deform upwards (pile-up) or downwards (sink-in) along the direction of the load (Fig. 2.19).

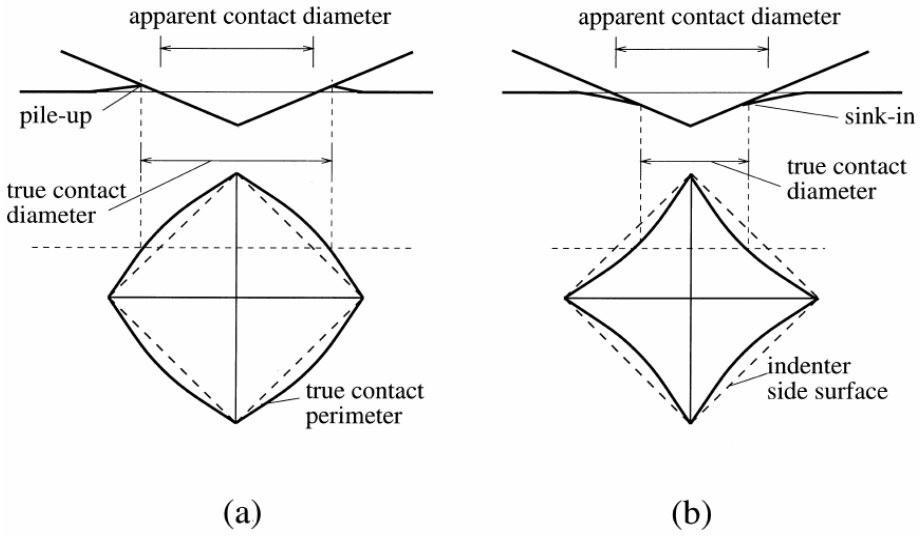

Fig. 2.19 Schematic illustrations of (a) pile-up and (b) sink-in around a sharp indenter [89].

Alcala et al [92] found that the deformation of pile-up or sink-in is correlated with the uniaxial strain hardening exponent. If the strain hardening exponent $n > 0.2$, sink-in is dominant. Das et al [93] and Xu and Rowcliffe [94] found that no pile-up occurs for materials with $n > 0.3$. Giannakopoulos et al [95] interpreted the deformation mode with computation results. They found that the pile-up or sink-in in a material around the indenter is primarily affected by the plastic properties of the material. Plastically displaced material tends to flow up to the faces of the indenter in a low-strain-hardening alloy due to the incompressibility of plastic deformation. The result is a "barrel-shaped" impression due to pile-up around the sharp polygonal indenter. On the other hand, for high-strain-hardening materials, the plastically deformed region is pushed out from the indenter with the imprint sinking below the initial surface level. The result is a "pin-cushionlike" impression around the sharp indenter. Methods, which are properly account for pile-up and sink-in around the indenter, are essential for the interpretation of the

plastic properties of materials by recourse to instrumented indentation. It also influences hardness measurements as the true contact area between the indenter and the specimen increases in the case where pile-up predominates, and decreases in the event that sink-in occurs. For Al and its alloys, the strain hardening exponent is < 0.242 [96].

2.6 Fracture Toughness Measurement through Nanoindentation

Micro/Nano Indentation technique is widely used for measuring the elastic modulus and the hardness of small volumes of material and thin films. The fracture toughness K_C , a measure of materials resistance against crack propagation, is a critical parameter investigated with micro/nano-indentation. Fracture toughness can be readily measured in brittle materials by inducing cracks at the corners of the indentation, a method known as indentation microfracture [97-102]. Indentation of brittle materials with a Vickers or Berkovich indenter often produces crack systems that generate from the indentation corners, as shown in Fig. 2.20 and Fig. 2.21**.** The sizes of the resultant cracks that develop about the residual impression are generally measured or the resultant strengths of such indented samples are determined from which the fracture toughness is calculated. It has been usual to employ a Vickers diamond pyramid indenter at loads greater than 1 N for such purposes. Different from Vickers indenter, the Berkovich geometry does not allow a halfpenny crack to join two corners and pass through the centre of the indent. Another difference is that the number of cracks of Vickers is 4 and Berkovich is 3. Dukino and Swain [103] compared the load dependence of the radial crack size with Vickers and Berkovich indenters They found that the expression developed by Laugier [98] is the best to describe the radial crack for Berkovich as shown in Fig. 2.21a. They also found that the Berkovich indenter gave more consistent toughness values at lower loads (<5N) than a Vickers indenter. They also suggested that the extent of radial cracks was slightly larger (of a ratio $(1.073)^{2/3}$) for the Berkovich than for the Vickers indenter due to the different crack numbers. Therefore the fracture toughness equation for Palmqvist crack extension as proposed by Laugier may be written

$$k_C = x(\frac{a}{l})^{1/2}(\frac{E}{H})^{2/3}\frac{P}{c^{3/2}} \tag{2.5}$$

where $x = 0.015$ for Vickers indenter [101], $x = 0.015 \times 1.073 = 0.0161$ for Berkovich indenter.

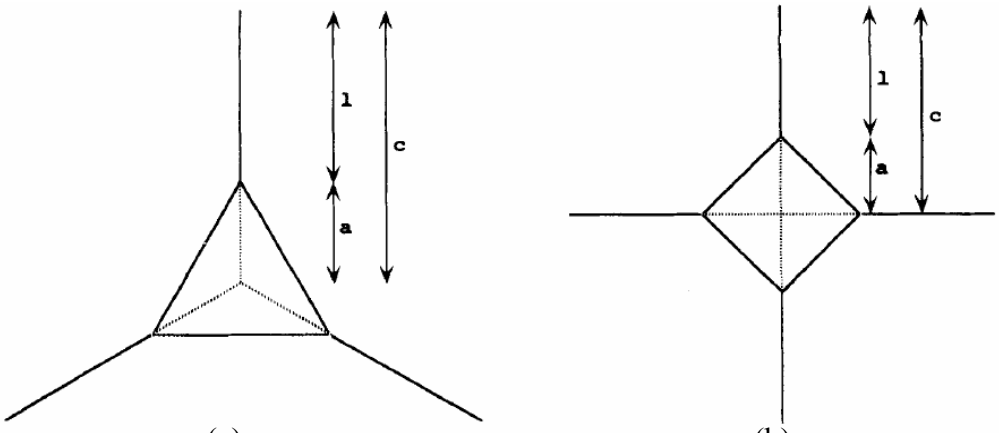

(a) (b)

Fig. 2.20 Illustration of indentation crack geometry: (a) Berkovich and (b) Vickers impressions [98].

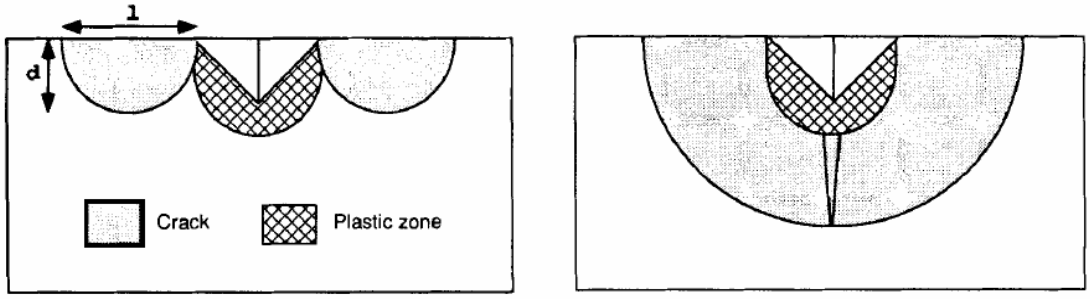

(a) (b)

Fig. 2.21 Cross-section view of (a) radial or Palmqvist (Berkovich indenter) and (b) halfpenny crack systems (Vickers indenter) [98].

Literature reviews have been conducted on basic wear mechanisms and an emphasis on the wear properties of AlSi alloys. However, the underline mechanism of wear resistance of AlSi alloys is far from clear and need further investigation. In the following chapters, a system study has been carried out to study the surface damages in AlSi alloys which may occur during wear tests. For this reason, experimental and theoretical approaches such as molecular dynamics study and indentation technique have also been introduced for characterizing surface damages at micro scale.

CHAPTER 3 MATERIALS AND METHODOLOGY

3.1 Materials

A hypereutectic Al-Si alloy with 17wt%Si is selected as a model system in which the primary Si particles are metallurgically formed during a die cast process and have a similar volume (~20,000 μm^2) but irregular shapes and characteristic microstructure shown in Fig. 3.1. Energy dispersive X-ray spectroscopy (EDS) spectrum of Al matrix and Si particles are given in Fig. 3.2. All figures and illustrations in this chapter are extracted from experimental results.

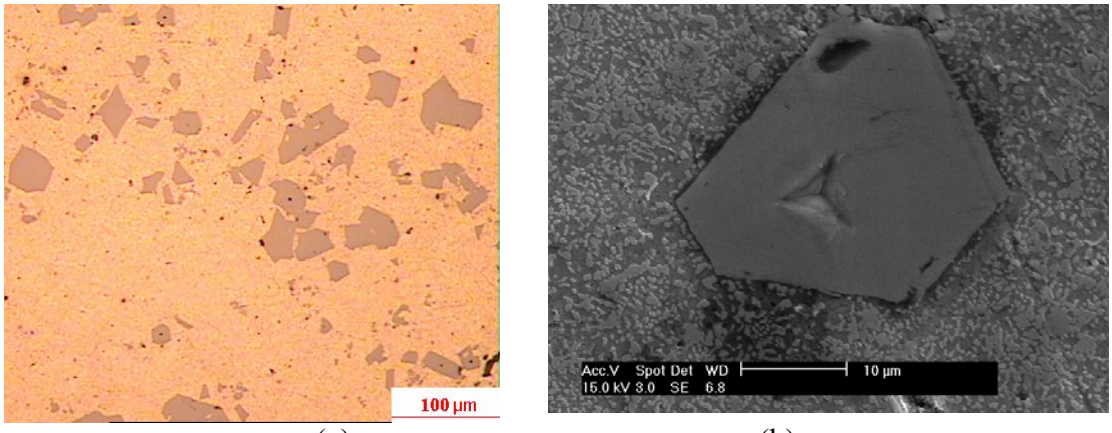

(a) (b)

Fig. 3.1 Microstructures of the alloy: (a) optical and (b) secondary-electron SEM image of etched surface. Notice Al in dark grey, intermetallics in light grey and a primary silicon particle with a Berkovich indent.

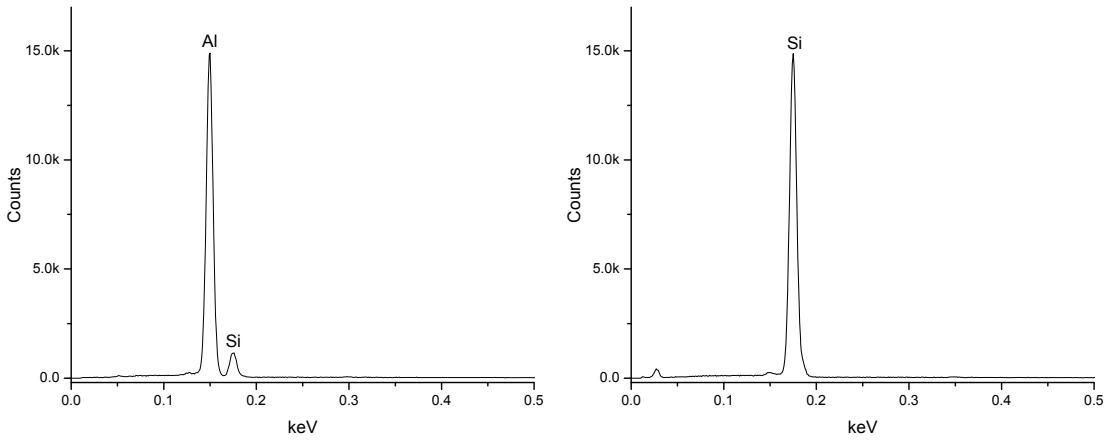

(a) Al matrix (b) Si particles

Fig. 3.2 EDS spectrum of (a) Al matrix and (b) Si particles.

The sample surfaces were finished by mechanical grinding using 4000 grit SiC grinding paper and polishing using 0.1 μm alumina suspension. After cleaned with ethanol and acetone, the surface was examined using a Hysitron Ubi 1 Nanomechanical Test Instrument, which is a nano indentation/scrach tester with SPM imaging capability. The roughness R_a of silicon particles was around 3 nm while the surrounded area was below 10 nm. The silicon particles protruded about 40 nm from the matrix as shown in Fig. 3.3. The hardness of matrix was HV 76.6 (751 MPa).

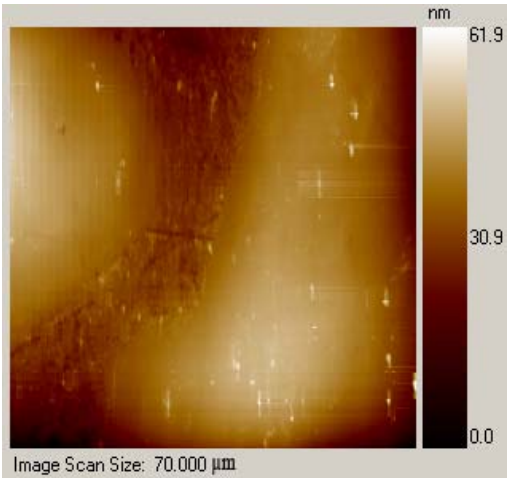

Fig. 3.3 SPM image of protruding Si particles.

3.2 Methodology

To study the debonding strength of Al/Si interface and fracture mechanism of Si particles in Al matrix, nanoindentation, SEM and SPM imaging, a serial sectioning method, first derivative analysis of load-displacement curves and FEM simulation were employed. The first derivative of load-displacement curves combined with SPM imaging was utilized to obtain the yield and debonding strength of Si particle under indentation in the inclusion-matrix system. The serial sectioning method was applied to acquire 2D images of the microstructure as a basis for reconstructing 3D solids for FEM modeling. 3D structure of Si particles and threshold stresses will be used as input for FEM analysis to verify the abovementioned atomistic simulation. Fracture of Si particles was statistically investigated.

3.2.1 Nanoindentation*

Instrumented indentation is a technique used to characterize local mechanical properties of solid materials by recording load and displacement data throughout the indentation experiment. Standard techniques such as the Oliver and Pharr method [91] are used to obtain hardness, elastic modulus and other mechanical properties. For many materials, discrete phenomena such as phase transformation, dislocation nucleation or cracking take place during indentation testing, showing up as discontinuous events in the load-displacement curve. For silicon, the responses during indentation are pop-in, elbowing and pop-out (Fig. 3.4.). These responses on the loading/unloading curves are considered to be related to the density change of silicon caused by the high pressure induced phase transformations. In loading, diamond cubic silicon transforms to the denser phase and thus the pop-in appears due to a sudden volume reduction [104, 105]. In contrast, in unloading the transition is to a lower density structure associated with a volume expansion, and consequently elbowing (continual decrease in slope of unloading curve) and pop-out occur [106, 107]. However, these pop-in events in silicon induced by phase transformation have been seen for spherical indentations, but have never been reported for indentations created by sharp indenters. Regarding dislocation nucleation under indentation, the critical shear stress for the generation of dislocations in silicon is higher than that for the inset of phase transitions, no dislocations could be found to generate pop-in [108]. The influence of indenter angle on the nanoindentation cracking behavior of single crystal Si and Ge was systematically explored with a series of triangular pyramidal indenters with different centerline-to-face angles in the range [109]. Pop-in events only occurred with a very sharp cube-corner indentation (centerline-to-face angle was 35.3º) in Ge sample at 50 mN which was deemed to correspond to chipping and material removal. Therefore, sharp Berkovich indenter (centerline-to-face angle is 65.3º) was chosen in this work to avoid unwanted discrete events for determining the debonding strength of Al/Si interface.

* In collaboration with Dr. Qi Yang at Structures, Materials and Propulsion Laboratory of Institute of Aerospace Research, Ottawa, Ontario

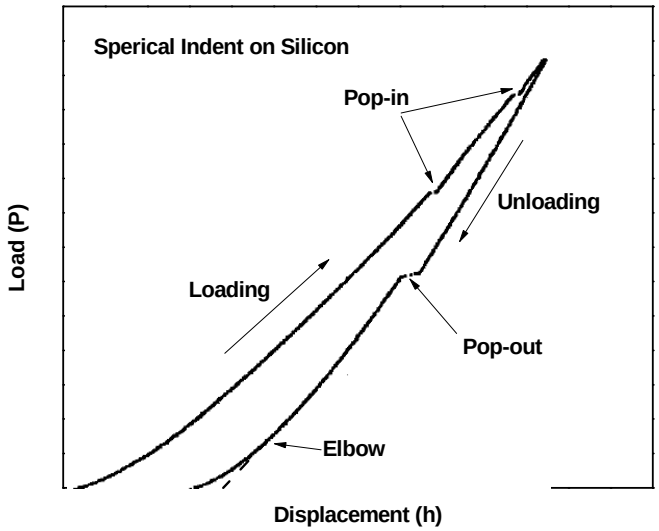

Fig. 3.4 Typical discrete events during spherical indentation.

In this work, nanoindentations were made on randomly selected 60 Si particles with sharp Berkovich diamond pyramid using a CSM Nano Hardness Tester as shown in Fig. 3.5a. The average size of these Si particles was 15.1 μm. Indentations were performed under load control and with a loading/unloading rate of 600 mN/min and the maximal load of 300 mN as shown in Fig. 3.5b.

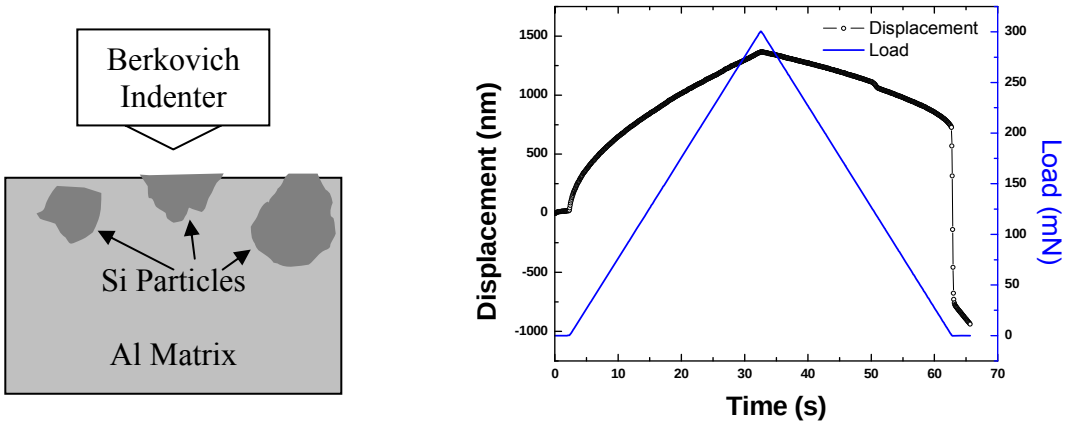

(a) (b)

Fig. 3.5 Indentation setup (a) and load controlled loading rate (b).

After indentation, secondary electron SEM images were taken for each indented Si particle to obtain surface topography and backscattered electron SEM images were used to measure the indentation crack length of Si particles. The debonding was checked by

backscattered electron SEM and measured as the sink-in depth of Si particles over Al matrix using Hysitron UBI 1 SPM.

3.2.2 Numerical Derivative Analysis of Load-Displacement Loading Curves

The load-displacement curve is used to derive mechanical properties such as Young's modulus and the hardness from the unloading curve [91], as well as the yield stress and strain hardening from the loading curve using FEM analysis [110-112]. However, discrete events such as pop-in and pop-out cannot be analyzed by conventional techniques that require load-displacement data to form continuous curves during loading and unloading of the experiment. Consequently, it is necessary to develop quantitative methods to determine the discrete events and whatever mechanism it is due to. Derivative calculation method has been used to characterize such events by Juliano et al [113], Malzbender and de With [114]. Juliano et al investigated transient event during loading and elbowing/pop-out during unloading in both thin film and bulk material by first derivative calculation. Malzbender and de With incorporated more dependencies to see the point at which fracture of coatings begins. They have used plots of P/h^2 vs. h^2 and $\partial P/\partial(h^2)$ vs. h^2 for Berkovich indentation to more clearly see these event points. In this work, first derivative of load-displacement curves has been used to investigate discrete events such as debonding of Al/Si interface and matrix yield strength in two phase materials. However, due to inherent sampling and control mode of instrumented indentation, noise is inevitable in practice and the first derivative of load is considerably wavy as shown in Fig. 3.6. Without appropriate fitting procedure, the usefulness of derivative analysis is limited within the scope near discrete events.

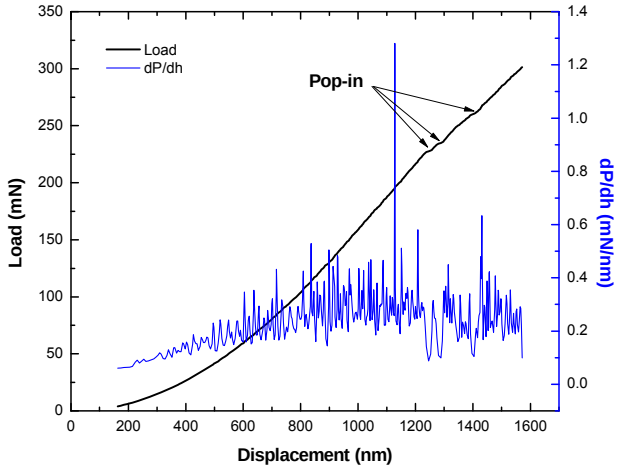

Fig. 3.6 Typical dP/dh curve upon loading without fitting.

In this work, a subsection polynomial fitting was used to derivate the slope of load-displacement loading curve. First, the first derivative of load-time was plotted as Fig. 3.7. The stable loading portion has been extracted for the derivation analysis. The extracted loading load-displacement data was then divided into continuous intervals, in which the curve was monotone.

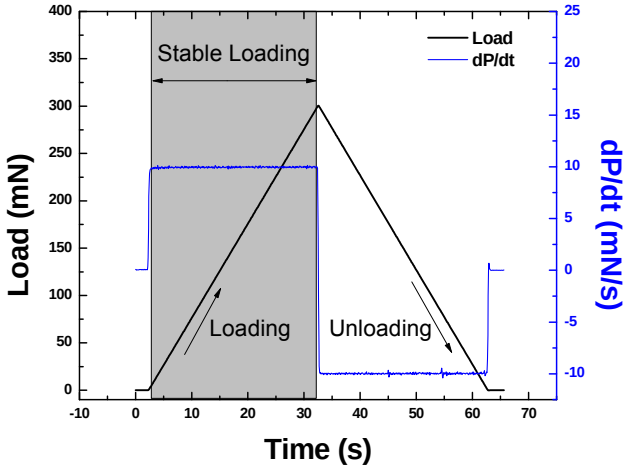

Fig. 3.7 Stable loading portion of indentation.

Each interval was polynomial fitted to the following model:

$$y = \beta_0 + \beta_0 x + \beta_2 x^2 + \beta_3 x^3 + ... + \beta_n x^n + \varepsilon \tag{3.1}$$

where $\varepsilon \sim N(0, \sigma^2)$, β_i are the coefficients and ε is the error term. Parameters are estimated using a weighted least-square method. This method minimizes the sum of the squares of the deviations between the theoretical curve and the experimental points for a range of independent variables. After fitting, the model can be evaluated by plotting residuals. It is worth noting that the higher order terms in polynomial equation have the greatest effect on the dependent variable. Consequently, models with high order terms (higher than 4) are extremely sensitive to the precision of coefficient values, where small differences in the coefficient values can result in a larges differences in the computed y value. For example, different orders polynomial fit are carried out for the same load-displacement curve. Although the regular residual of fitted load-displacement curves are all small (Fig. 3.8a), the first derivative of fitted curves show different trends (Fig. 3.8b). Among them, *dp*/*dh* curves of 3rd and 5th order polynomial fittings are better than 9th order.

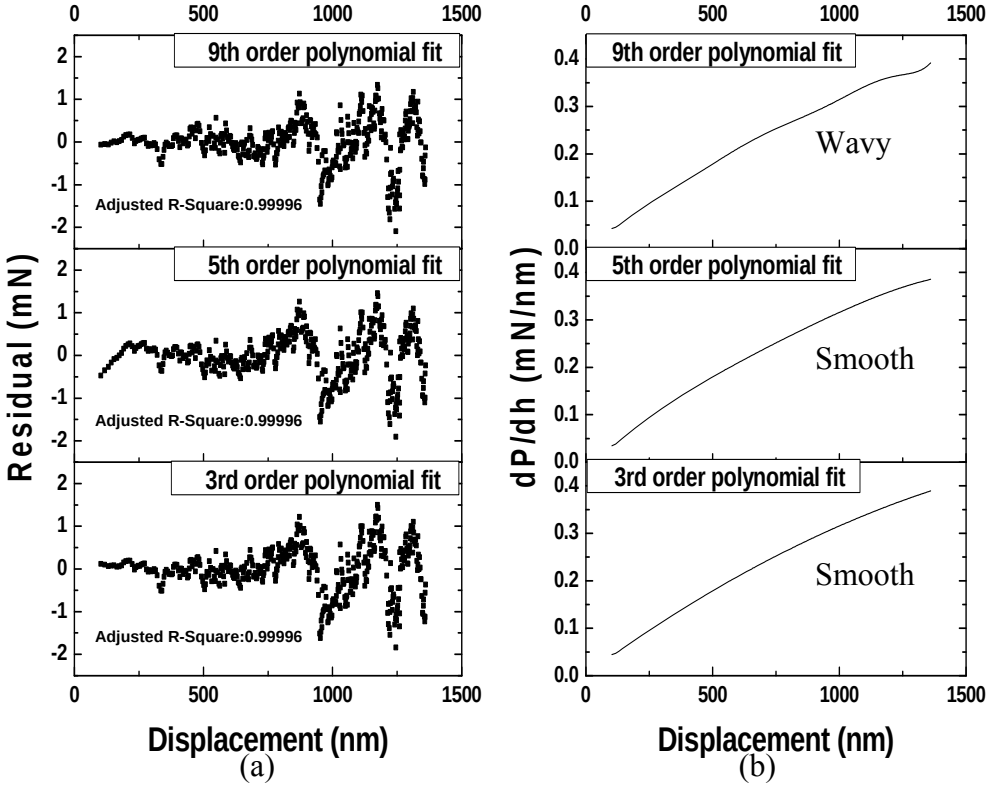

Fig. 3.8 Regular residual (a) and the first derivative (b) of different order polynomial fitted load-displacement curve.

Generally speaking, any continuous function can be fitted to a higher order polynomial model. However, higher order terms may not always have much practical significance. In this work, the order of polynomial fitting was not higher than 5. After fitting, the first derivative of load-displacement was calculated and analyzed.

3.2.3 Serial Sectioning

To capture the three dimensional microstructure, a few techniques are available such as non-destructive X-ray tomography [115], four–dimensional X-ray diffraction microscopy [116], and destructive serial sectioning including dimpling, machining, polishing or microtomy. A detailed comparison of serial sectioning techniques was given by Spowart [117]. Although automated serial sectioning [118, 119] increases sectioning rate and the consistency between the metallographic images produced from each section, manual polishing coupled with the use of optical fiducial marks was employed in this work due to inherent flexibility and relatively low cost of equipment. The basic concept of this serial sectioning process was to cyclically polish material to generate a series of microstructure sections. These sections were then segmented and assembled into a 3D solid using computer software. The basic steps of were as follows:

- Sample preparation
- Fiducial marking by indentation
- Polishing
- Imaging and image segmentation
- Serial section stacking and visualization

Fig. 3.9 shows a flow chart of the serial sectioning process. The material was sectioned and indented by a Vickers micro-hardness tester to create fiducial marks. Systematic polishing and imaging of the sample surface generated series of microstructure sections. Measurement of changes in the fiducial mark depth was used to determine the distance between sections. As shown in Fig. 3.10, the small indent in (b) was indented before polishing. The big one was indented after polishing. The difference in size and position of these two indents were used to calibrate particle section orientation and calculate distance

of sections. Using the 2D sections, a 3D solid was constructed using computer software. This solid was then used in modeling of deformation of the material using FEM analysis.

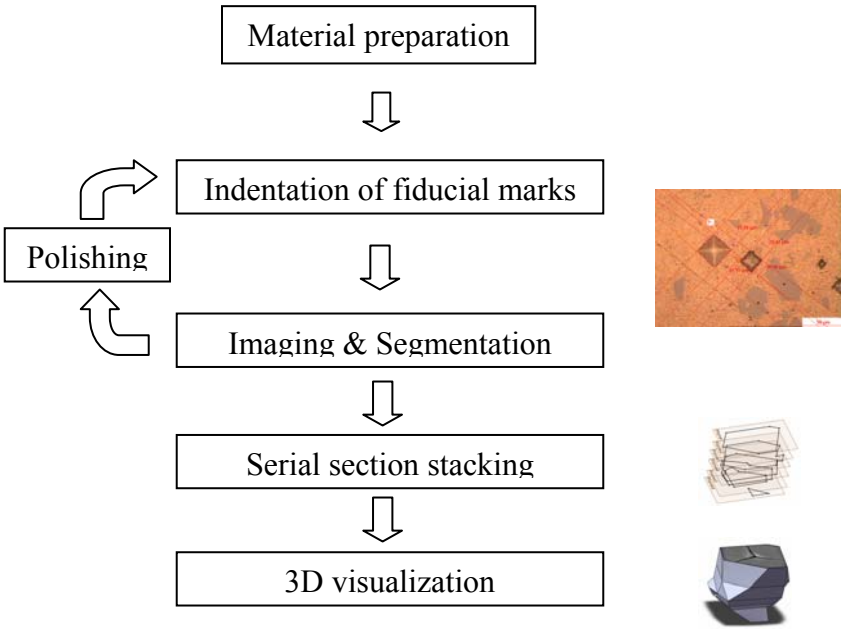

Fig. 3.9 Flow chart of serial sectioning process.

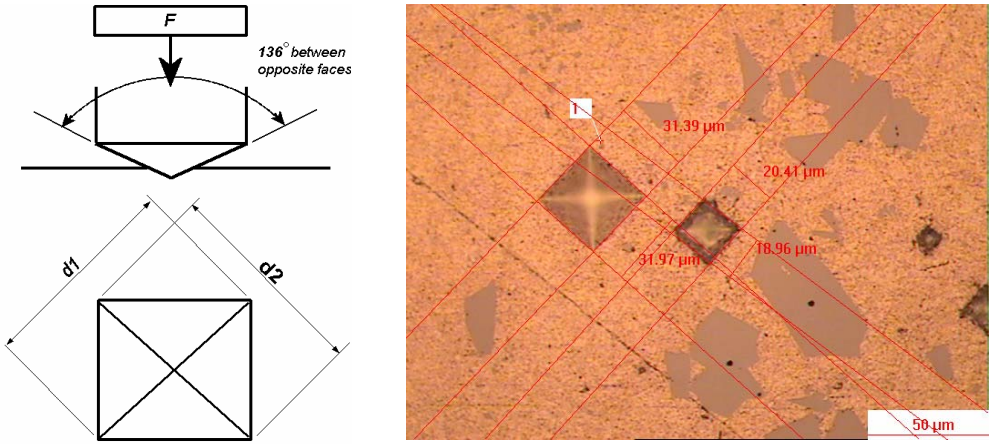

(a) (b)

Fig. 3.10 Fiducial marks made by Vickers indenter.

CHAPTER 4 RESULTS AND DISCUSSION

4.1 Classification and Identification of Indentations on Si Particles

After the indentations were made, a systemic classification and identification process has been performed to identify the indentation response of the particle/matrix system at micro scale following the workflow in Fig. 4.1:

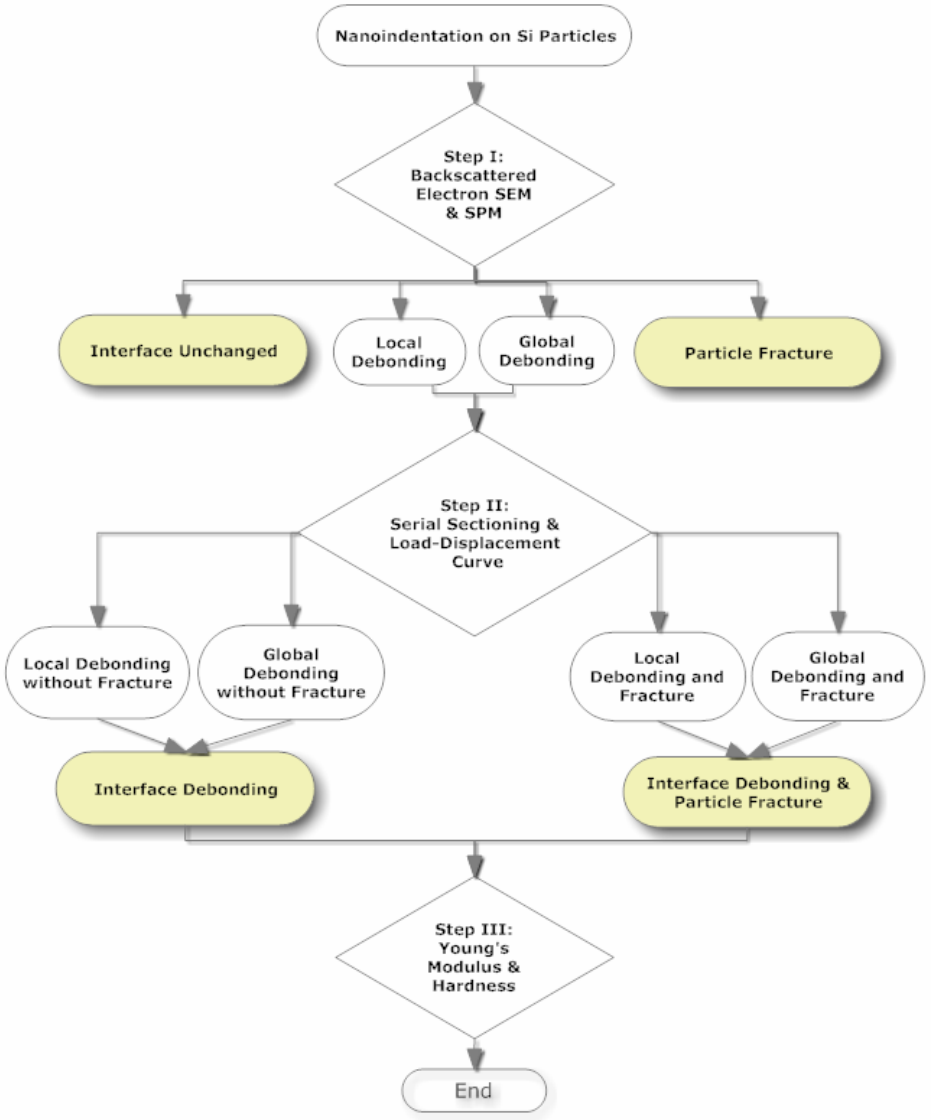

Fig. 4.1 Identifying indentation response of particle/matrix system at micro scale.

There were four classifications made to distinguish the indentation behavior of Si particles inside Al matrix. These cases are (1) interface unchanged, (2) interface

debonding, (3) interface debonding and particle fracture, and (4) particle fracture. Indentations with local/global debonding without fracture are our interest for studying the Al/Si interface strength. Fracturing of Si particles during indentation can be used to investigate wear property of AlSi alloys.

Step I:

Backscattered electron SEM imaging provides elemental composition variation as well as surface topography. Backscattered electrons are produced by the elastic interactions between the sample and the incident electron beam. These high energy electrons can escape from much deeper than secondary electrons, so surface topography is not as accurately as secondary electron imaging. However, the efficiency of production of backscattered electrons is proportional to the sample material's mean atomic number, which results in image contrast as a function of composition. Higher atomic number material appears brighter than low atomic number material. Profiting from this feature, backscattered electron imaging is particularly effective on detecting interface debonding where interstice between two materials shows dark color (Fig. 4.2a).

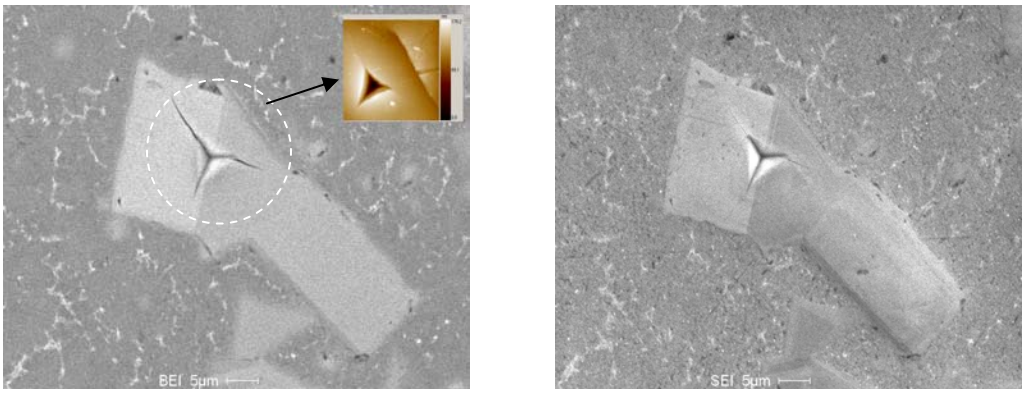

(a) Backscattered electron image (b)Secondary electron image

Fig. 4.2 Backscattered electron (a) and secondary electron (b) SEM image of a Si particle in Al matrix. Local interface debonding is visible in backscattered electron image and confirmed by SPM.

After roughly distinguished by backscattered electron SEM imaging, particles with unchanged interface and particles with debonding interface were identified by SPM

technique. Particles with debonding interface were further classified by serial sectioning and pop-out phenomenon in load-displacement curve. Fig. 4.3 demonstrates a particle without any deformation at Al/Si interface and a fracture particle.

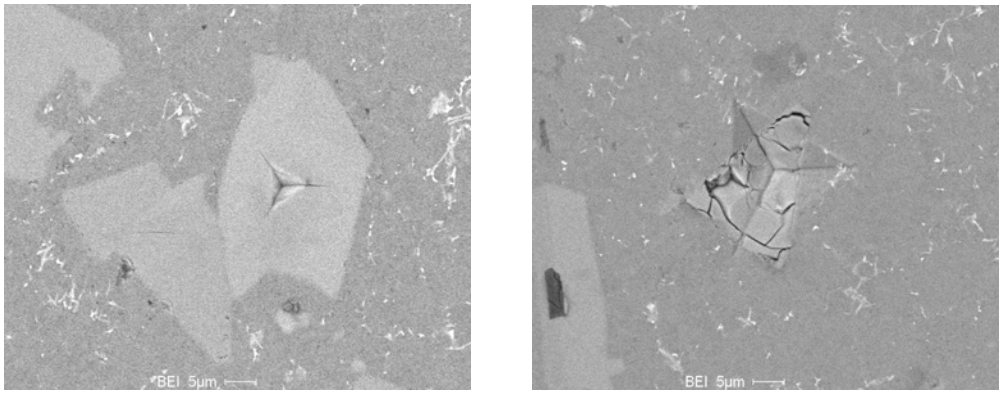

(a) Particle with unchanged interface (b) Particle fracture

Fig. 4.3 Backscattered electron imaging of a particle with interface unchanged and a fracture particle.

Step II:

Si particles with partial or overall debonding were evaluated by load-displacement curve, backscattered electron imaging and images from serial sectioning. Typical cases are listed in Fig. 4.4. It was found that if there was a crack at the edge of the particle in SEM image, the particle was likely to fracture (Fig. 4.4c-d). The percentage of fracture particles with edge crack was 68.8%. Pop-out phenomenon of load-displacement curve was also used to determine whether a particle was broken or not. If a particle fractures, the high stress induced by indentation is released before the phase transformation in Si can take place and therefore pop-out is not observed.

After completing the serial sectioning, 3D reconstruction was performed and all kinds of indentations on Si particles were grouped and presented in Fig. 4.5. In the case of a particle with global interface debonding, the whole particle sinks into the matrix with or without internal fracture. In contrast a particle with local interface debonding is predominantly tilted as a result of a partial sink-in of a portion of the particle under the

indenter force. These phenomena significantly affect the mechanical properties at micro scale. A further verification on the classification has been done in next step.

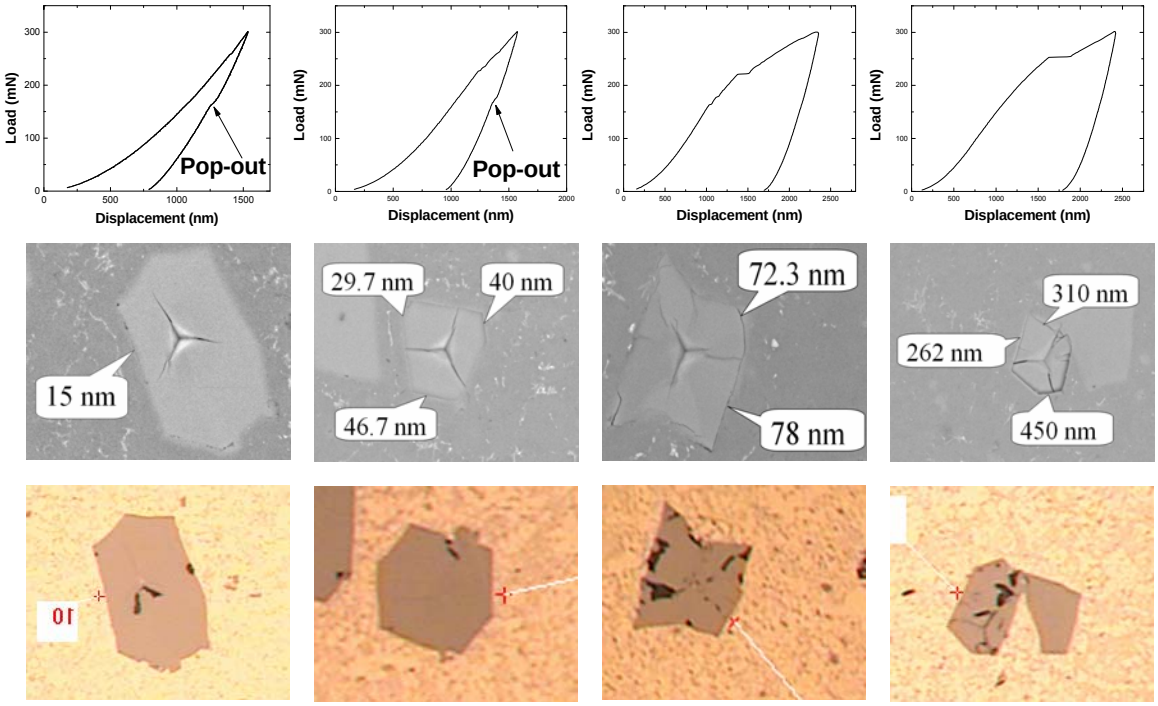

(a) Polished 3.53 um (b) Polished 6.32 um (c) Polished 4.94 um (d) Polished 6.32 um

Fig. 4.4 Determining interface debonding and particle fracture: (a) local debonding without fracture; (b) globe debonding without fracture; (c) local debonding and fracture; (d) globe debonding and fracture. Debonding depths were measured by Hysitron UBI 1 SPM. Notice in (a), (c) and (d), median cracks still existed.

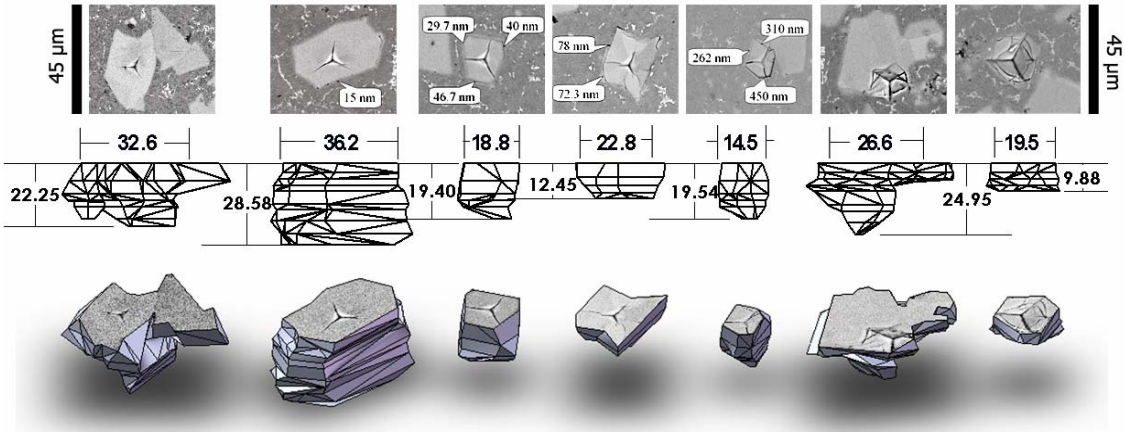

Fig. 4.5 Reconstruction of Si particles: (1) interface unchanged; (2a) local debonding; (2b) global debonding; (3a) local debonding and fracture; (3b) global debonding and fracture; (4a) and (4b) are fracture particles.

Step III:

Classification and Identification of Indentations on Si Particles were verified by indentation hardness and Young's modulus derived using Oliver and Pharr method. Following Eqns 2.1~2.3, Young's modulus and hardness distribution of indented Si particles are shown in Fig. 4.6.

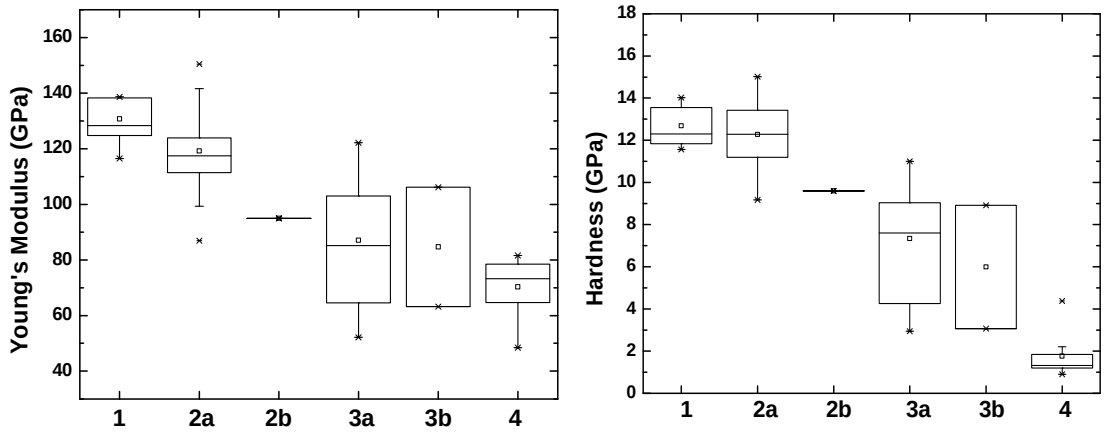

Fig. 4.6 Distribution of Young's modulus and hardness. From left to right, Group 1 - interface unchanged, Group 2a - local debonding, Group 2b - global debonding, Group 3a - local debonding and fracture, Group 3b - global debonding and fracture, Group 4 - fracture.

It can be noticed from Fig. 4.6, both average Young's modulus and hardness for particles with unchanged interface are close to bulk Si. For fracture particles, average Young's modulus is around 70 GPa, which is consistent with bulk Al materials. However, hardness of fracture particles is higher than of bulk Al. This may be explained by considering the definition of indentation Young's modulus, which is based on the slope of unloading starting portion where elastic deformation dominates. Because broken Si does not contribute to the elastic recovery, only the underneath matrix interacts with the load-controlled indenter, thus the Young's modulus measured is mainly the Al matrix modulus. For hardness measurement, due to the work of hard Si particles before fracturing, the final indent in Al matrix is smaller than in single phase matrix. Therefore the projected contact area is smaller and the hardness is higher than in bulk Al. Fig. 4.6 also shows an overall trend that the more deformation modes, the higher deformation degree and the lower Young's modulus and hardness. This trend is consistent with the indentation classification made in last two steps.

4.2 First Derivative Analysis of Load-Displacement Curves

Berkovich indenter was applied in this work to study the interfacial strength of Al/Si and indentation mechanism. The discrete events such as pop-in during loading are deemed to be irrelevant to phase transformation, crack or dislocation nucleation, etc. Indentations have been sorted and two main deformation mechanisms have been outlined, namely, interface debonding and particle fracture. To study the threshold of these two deformations, first derivative analysis was employed. Except that particles without debonding, pop-in phenomenon occurred during almost all the other indentations. Typical load-displacement cases of indentations on Si particles are presented in Fig. 4.7 corresponding to the SEM and 3D structure shown in Fig. 4.5.

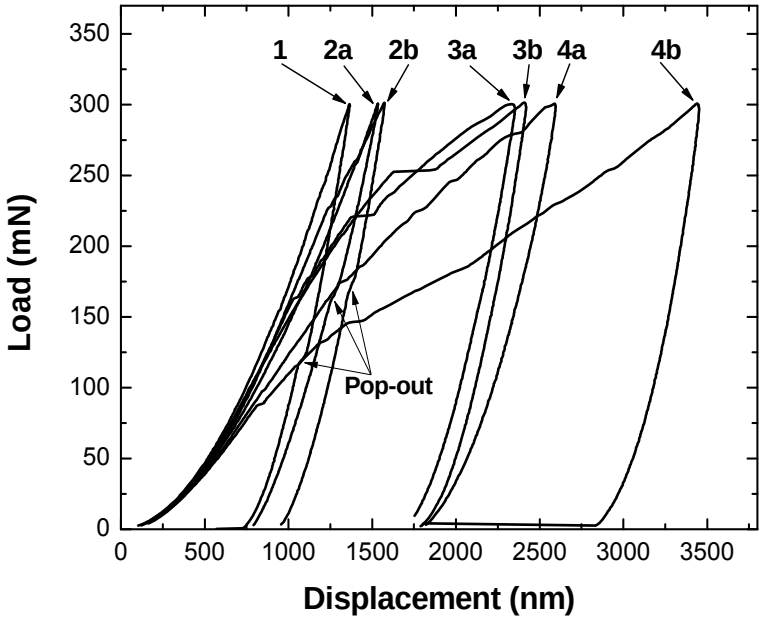

Fig. 4.7 Typical load-displacement curves of indentations on Si particles.
(1) Interface unchanged; (2a) local debonding; (2b) global debonding:
(3a) local debonding and fracture; (3b) global debonding and fracture;
(4a) particle fracture at corner; (4b) particle fracture at centre.

4.2.1 Unchanged Interface

A load-displacement curve of Case 1 is plotted in Fig. 4.8. Both the load-displacement and load-*dP/dh* are monotone. Hainsworth et al. [120] illustrated that for geometrically self-similar indenter tips, such as Berkovich, conical or pyramidal, the indentation load *P* and the indentation depth *h* were experimentally determined for single phase materials

during loading by the expression $P = Kh^n$, where K is a material-dependent constant, n falls somewhere between about 1.5 and 2. The power of dP/dh is 0.5~1 and accords with the power of the experimental dp/dh curve of Case 1. Thus the behavior of particles with unchanged interface under indentation can be considered as being the same as the bulk Si material. This judgment has been verified by indentation hardness and Young's modulus of such particles.

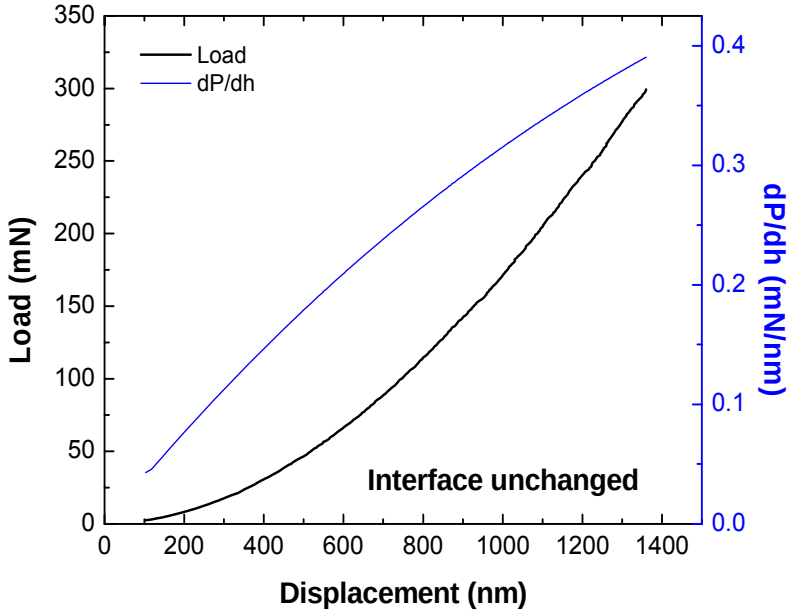

Fig. 4.8 Typical load-displacement and dP/dh curves of interface unchanged particles.

4.2.2 Interface Debonding

Pop-in events occurred in both local and global debonding cases (Fig. 4.9). The pop-in excursions derived from indentation curves fit well with the profile difference at Al/Si interface gained from SPM imaging (Fig. 4.4(2a) and 4.4(2b)). Indentations in these two cases exhibited the same behavior respectively. Therefore, the pop-in excursions can be used to estimate the interface debonding quantitatively. In contrast to the local debonding curve (Case 2a), the global debonding dp/dh curve (Case 2b) reaches a peak before pop-in appears. The stress at this point, calculated as the load over maximal section area of the

Si particle, is 470 MPa. Similar peaks were found in global debonding and fracture cases such as 438 MPa in Case 3b (Fig. 4.10), the average stress of this kind of peak is 460 MPa. The cause of such peaks during loading are not well understood at this time, but we may suggest at this point that the matrix surrounding the Si particle yields first, followed by interface debonding when indentation load is high enough to break the Al/Si interface. The first derivative of load displacement curve of Case 2a shows similar trend as of unchanged interface particle. Before the abrupt drop induced by partial debonding, the slope of load over displacement increases almost monotonously. Because the indention is made near the edge of the particle, the median cracks increase with the increase of the indentation load until one or two median cracks reach the boundary of the particle. The portion of the particle between the radial cracks tilt and partially sinks-in under the compressive pressure of the indenter. As a result a pop-in is observed in the load-displacement curves. Since in this case, only portion of the particle contributes to the debonding, no global matrix yield is involved and therefore no peak is observed in the *dP*/*dh* curve.

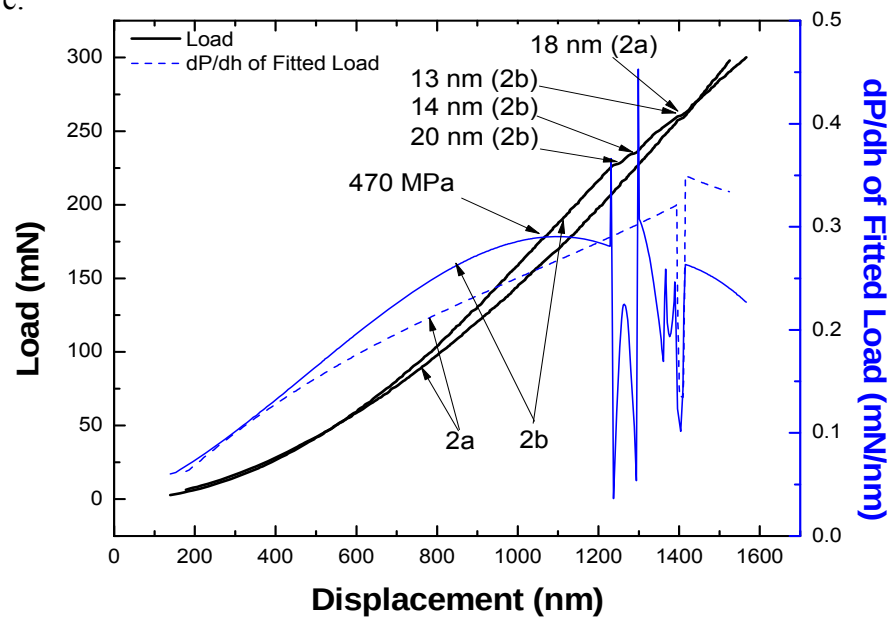

Fig. 4.9 Typical load-displacement and *dP/dh* curves of interface debonding particles.

4.2.3 Interface Debonding and Fracture

The *dP/dh* behavior of global interface debonding (Case 3b) with fracture is similar to global debonding without fracture (Case 2b), featuring a yield peak of 438 MPa and a large pop-in excursion of 262 nm. However, due to relatively smaller size and volume, the particle fractured after global debonding. As to local debonding and fracture Case 3a, it seems that fracturing occurred first at 278 MPa and followed by local debonding to generate a pop-in excursion of about 140 nm. The stress of the first pop-in, 278 MPa, is defined as fracture stress.

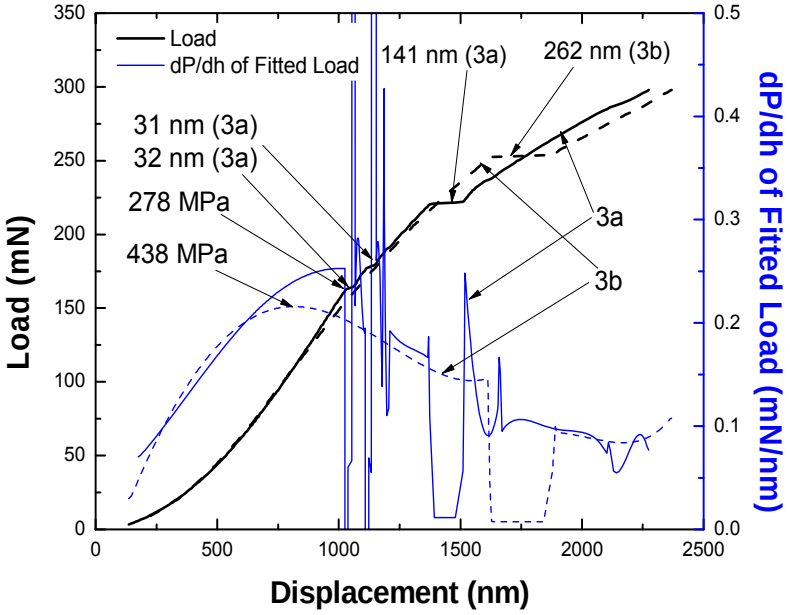

Fig. 4.10 Typical load-displacement and *dP/dh* curves of interface debonding and fracture particles.

4.2.4 Particle Fracture

For fractured particles, there are no distinct pop-in events as shown in Fig. 4.11. It suggests that particle fracturing is a gradual process with accumulation of small pop-in segments. Particle fracturing is much more complicated than debonding. There is no clear

trend in the overall scope of the *dP/dh* curve. The threshold stress for fracture initiating was calculated for the following statistics study.

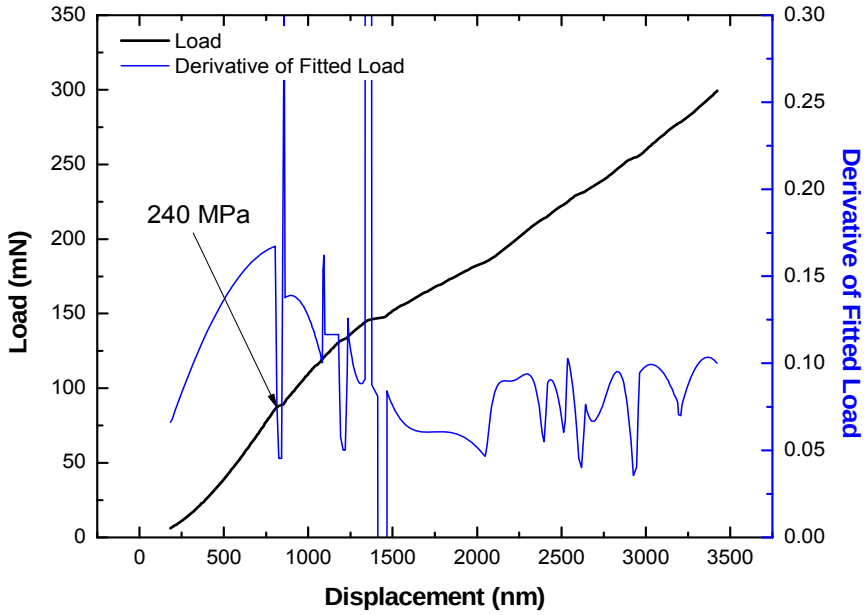

Fig. 4.11 Typical load-displacement and dP/dh curve of fracture particles.

4.3 Statistics of fracture particles

An important factor for wear resistance of MMC is the particle morphology. Both the size and morphology of the silicon particles affected the wear resistance [121-123]. Particle morphology can be characterized in three ways (i) size, (ii) aspect ratio, and (iii) circularity values of the particles. Dighe and Gokhale [122] observed that debonded Si particles are on the average larger than non-debonded particles in a cast AlSiMg alloy. The fracture is found to be governed by the "tail end" (i.e., extremum) of the Si particles size distribution, and not by the over all population of Si particles (i.e., not by average microstructure). Elmadagli et al [123] investigated microstructural elements including Si weight percentage, Si particle morphology, Si particle size, alloy hardness of AlSi alloys on the wear behaviour of AlSi alloys. The Si particle morphology and size influenced the wear coefficients in mild wear as well as the transition loads between two mild wear phases. For instance, decreasing particle size reduced the wear coefficients and increased the transition loads. However, the values used in such studies are usually area based, i.e., limited in 2D field. In this work, Si particle morphology is both 2D and 3D valued using

fracture stress induced by nanoindentation. 3D size, aspect ratio and sphericity are obtained from 3D reconstruction. As shown in Fig. 4.12, size effect in 2D and 3D are largely different. The high fracture stresses appear in the small 2D size and large 3D size area. The fracture stress vs. 2D aspect ratio and circularity seem to be dispersed. On the contrary, 3D aspect ratio, defined as particle height over equivalent diameter of maximal section, is in direct ratio to fracture stress, which means the particle that has a spherical structure will sustain a higher fracture stress. This trend is also confirmed by the relationship of 3D sphericity vs. fracture hardness. To sum up, 3D particle morphology produces more information than of 2D.

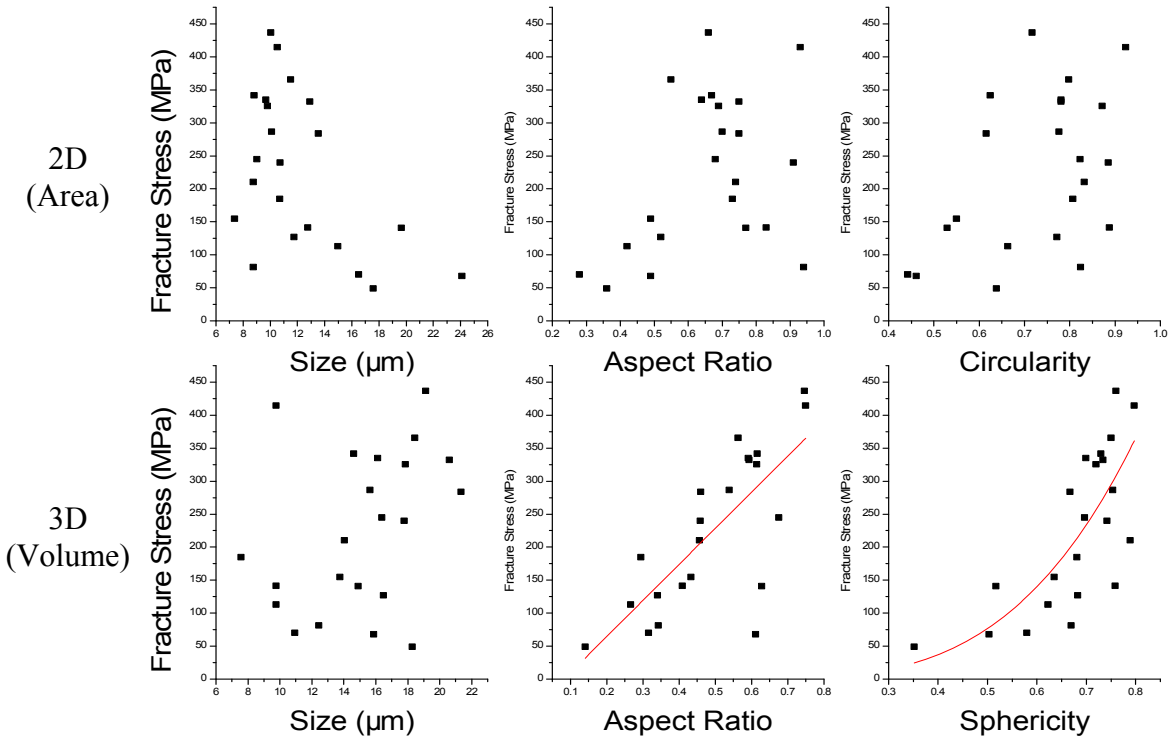

Fig. 4.12 Comparison of 2D and 3D particle morphology. Definitions are given in Table 4.1.

	Size	Aspect Ratio	Circularity/Sphericity
2D (Area based)	Diameter of the sphere that has the same surface area as a given particle.	width/length	$S = \frac{4\pi(\text{area})}{(\text{perimeter})^2}$
3D (Volume based)	Diameter of the sphere that has same volume as a given particle	h/D_{max} h is particle height, D_{max} is equivalent diameter of the maximal section	$\Psi = \frac{\pi^{\frac{1}{3}}(6V_p)^{\frac{2}{3}}}{A_p}$ V_p is volume of the particle, A_p is surface area of the particle.

Table 4.1. Definition of Particle Morphology in 2D & 3D.

4.4 Fracture Toughness

In this project, the 2D size of Si particles require of the loads in order to produce small cracks, shorter than minimal size of 10 μm, within the Si particle. However, to study the interface strength, indentation load must be high enough to break the Al/Si interface. As a result, four kinds of particles are classified in Section 4.1. To obtain accurate fracture toughness of Si particles in Al matrix, only particles without fracture and interface debonding (Case 1) are proper for the work. Among 60 indented Si particles, only 4 of them have identifiable indentation cracks that no one reaches the particle boundary. Backscattered electron images of these 4 indentations were taken to measure the length of cracks. The average fracture toughness calculated using Eq. 2.4 is 1.31 MPa/m$^{1/2}$ with $x = 0.0161$ for Berkovich indenter. To our knowledge, this fracture toughness for Si primary particles in AlSi alloys has not been reported before. Laugier expression and other expressions are applied mostly to bulk materials, without restrictions on the load applied or the crack length. In order to assess the K_C by Laugier expression with short crack length, it is necessary to compare the K_C with well reported ones including both short cracks and large cracks. A comparison between short and large crack testing method is given in Fig. 4.13. Xin et al [124], Brede et al [125], Chen et al [126] and Casellas et al [127] investigated indentation fracture toughness on singlecrystal Si in the (100) plane. Among them, Casellas et al studied the fracture toughness with a small load of 0.2 N to get short cracks and used a modified Laugier expression the same as

described in Section 2.5. It is obvious that for bulk Si materials, K_C is consistent for both short and large crack cases.

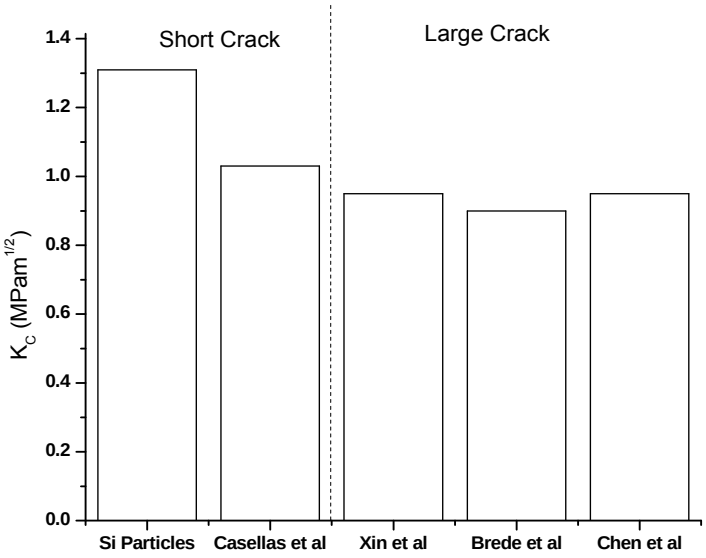

Fig. 4.13 Comparison between K_C obtained with short and large crack testing methods.

Considering the anisotropy in K_C, Ericson et al studied fracture toughness of single crystal Si with different crystal orientations and found K_C of Si is between 0.83~0.95 $MPam^{1/2}$ [128]. In this project, K_C of Si particles in Al matrix is much higher than of bulk Si materials. It is well know that materials with high fracture toughness are capable of absorbing more energy than materials with low toughness before fracturing. For brittle materials such as Si, the plastic deformation is little and the ability of energy absorption is low. Plastic deformations induced by indentation in Si bulk materials mainly are Berkovich indents and radial cracks. When indentation is made on a Si particle in Al matrix, Si particle may sink to some extent into the ductile Al matrix (K_C > 14 $MPam^{1/2}$) and part of the energy is transfer into Al matrix and induces elastic deformation in surrounding Al matrix. This elastic deformation in Al matrix leads to a difference Δh in indentation depth which decreases crack length in Si particle. Therefore, considering the Eqn. 2.4, the K_C of Si particles is higher than of bulk materials. After indentation, Si particle recovers to its original position. The elastic motion of Si particle in Al matrix has been proved in FEM analysis.

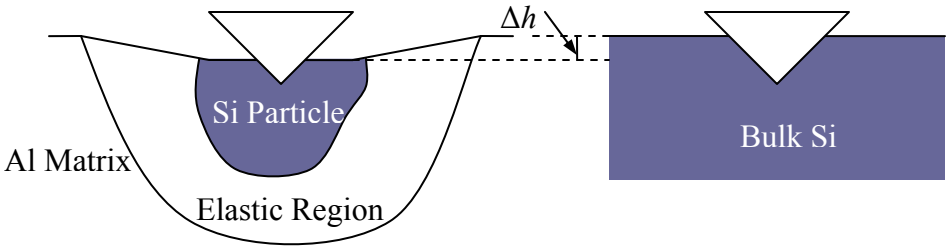

Fig. 4.14 A schematic of indented Si particle in Al matrix at maximal load.

4.5 Pile-up of Indentations

Both indentations of Si particle and Al matrix under Berkovich indenter show pile-up which are consistent with their single crystal counterparts [129]. Fig. 4.15 presents an AFM image of indentation on a Si particle and the section profile. Indentation pile-up for Al matrix is plotted in Fig. 4.16. As reviewed in Chapter 2, this pile-up can be explained by the plastic properties of low-strain-hardening materials, i.e., the plastically displaced material under the faces of the indenter tends to flow up due to the incompressibility of plastic deformation.

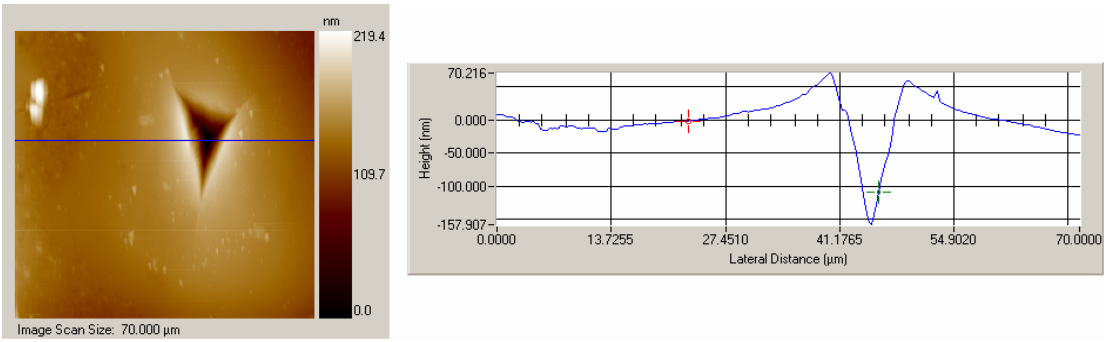

Fig. 4.15 Indentation pile-up of Si particles in Al matrix. Indentation load was 300 mN.

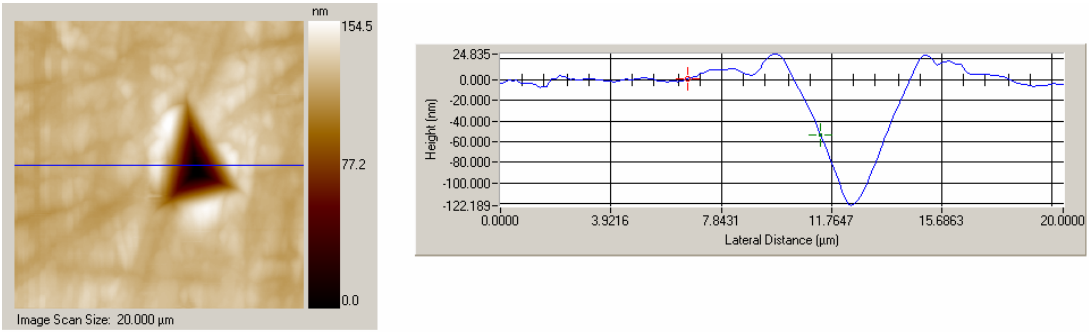

Fig. 4.16 Indentation pile-up of Al matrix. Indentation load was 5 mN.

4.6 Wear Model during Break-in

Based on above discussions, an energetic wear model for the hypereutectic AlSi during break-in is proposed. In the early stage of UMW, the contact pressures and the local energy dissipation is highest on the raised Si particles. Si particles elastically sink into the Al matrix without interface debonding when the applied stress does not exceed a threshold value, in this project, around 450 MPa for 300 mN load. Considering the drop of strengths of Al alloys at high temperature, for example, the tensile yield strength of Al 390 after T6 temper is 365 MPa at 38 °C and is 305 MPa at 150 °C [130], the feasibility of Si particle sinking under loading is higher. The result of the elastic sinking is twofold. On the one hand, the elastic sinking of Si particles can reduce the impact of wear load and thus protect the material surface. On the other hand, if the raised height of Si particles and hardness, strength of the matrix are not well controlled, Si particles may sink too much that the matrix exposes to the sliding counterpart, wear becomes severe.

Fracture of Si particles also plays a key role in the early stage of wear. Even large particles will crack if the 3D shape of the particle is highly irregular. This leads to increased local wear on these spots. The released Si wear debris then, are embedded into the relatively soft Al matrix. This mechanism could be described as friction induced dispersion hardening. Orowan type strengthening is applicable for this kind of mechanism and the new formed layer has higher shear stress after break-in.

From above discussion, we may suggest that Si particles do not have to bear the load after break-in as supposed to. However, Si particles may act as micro bumpers if morphology of the Si particles and matrix properties are rightly designed to avoid unfavorable fracture, crack and debonding. Therefore, the interface strength of randomly distributed Si particles with different crystal orientations and the matrix is a key in wear properties of AlSi alloys.

CHAPTER 5 FINITE ELEMENT ANALYSIS OF INSTRUMENTED INDENTATIONS

This chapter presents finite element analysis of instrumented nanoindentations of Si inclusions/Al matrix system. The indentation processes are simulated with the ABAQUS finite element (FE) software package. Debonding of Al/Si interface, fracture mechanism of Si particles and plastic deformation of Al matrix are discussed with their effects on wear behavior. Based on the simulation, an indentation map for Si particles in Al matrix is developed.

5.1 Structural Model

The indentation process is complex, so simplifications and assumptions have to be made to achieve low numerical cost but sufficient accuracy. For instance, we assume the surface of the specimen as ideally smooth, whereas in reality a certain roughness may be present as well as e.g. a thin layer of oxidized material. The indentation process is considered to be quasistatic and the method of indentation control is also considered. All indentation experiments were carried out under load-controlled conditions because a real indentation experiment is hard to execute under displacement-controlled conditions up to a maximal displacement. Therefore, load-controlled condition is applied in the simulation.

For the experiments, diamond Berkovich indenter was applied in all indentation tests. The Berkovich geometry is not axisymmetric. Due to low numerical cost in the simulation of the experiment, a conical rigid indenter with a half angle of 70.3º as given in Fig. 5.1, which has the same projected area-depth function as the standard Berkovich indenter, is used for simulation to build the axisymmetric model. The radius of the tip of the indenter is chosen to be 0.2 μm [131]. The size of the Al matrix is chosen so that the boundaries of the matrix do not influence the results. The half plane of Al matrix is defined as 100 μm in both width and height. The nodes at the bottom of the Al matrix are fixed in all directions and the center line is fixed horizontally. The applied boundary conditions are depicted in Fig. 5.1.

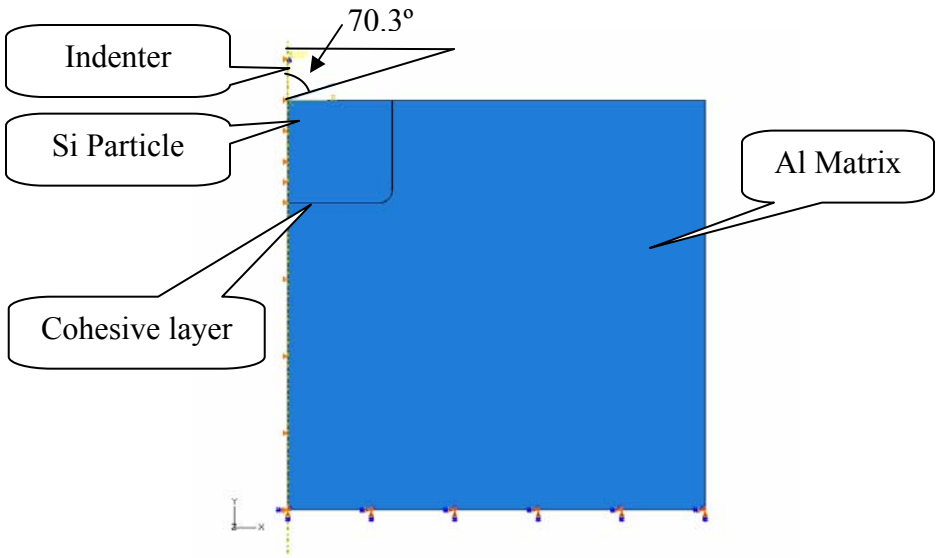

Fig. 5.1 Structural model and boundary conditions.

\

Si particle is defined as a cylinder with a round edge of 3 μm in radius. Between Si particle and Al matrix, a cohesive layer of 0.05 μm in thickness is set to act as the bonding interface of Al/Si. The cohesive behavior is defined directly in terms of a traction-separation law which can be used to model the delamination at interfaces in composites directly in terms of traction versus separation. It also allows specification of material data such as the fracture energy as a function of the ratio of normal to shear deformation at the interface. The cohesive behavior assumes a linear elastic traction-separation law prior to damage which means the initial response of the cohesive element is linear until a damage initiation criterion is met, and then material damage can occur according to a user-defined damage evolution law. Normally a maximum nominal stress criterion is used with a damage evolution based on fracture energy. The damage evolution law describes the rate at which the material stiffness is degraded once the corresponding initiation criterion is reached. However, for Al/Si system, the fracture energy has not been reported or studied neither experimentally nor theoretically. If the damage initiation criterion is specified without a corresponding damage evolution model, Abaqus will evaluate the damage initiation criterion for output purposes only; there is no effect on the response of the cohesive element (i.e., no damage will occur) [132].

Therefore, the damage evolution is not set in this project and the shear stress of interface is used to be compared with the atomic simulation results as given in Section 2.3.

For the indenter/Si particle interaction, the standard Lagrange method is used to handle surface-to-surface contact. The contact surfaces are thereby treated with the master-slave concept. Therein the master, in our case the indenter, is trying to penetrate into the half-space Si particle which is defined as the slave. The nodes of the slave are not allowed to penetrate into the master's surface. The implementation of contact in ABAQUS is done by adding a contact term with a Lagrangian multiplier to the potential. Applying a variation to the potential, this term contributes to the stiffness matrix. ABAQUS offers the possibility to consider Coulomb's friction with the coefficient of friction μ as a parameter. However, Zhang and Mahdi [133] demonstrated that calculations with different friction coefficients show that the effect of interface friction is negligible in terms of the indentation load-displacement relationship and the stress and strain distributions with a certain distance away from the contact surface. The friction has a large effect on the stresses in the neighborhood of the indentation interface, particularly near the contact boundary. In this project, the research focus on the Al/Si interface, plastic deformation of Al matrix and fracture of Si particles determine that the local stress near contact boundary is not important. Therefore, the friction between the indenter tip and the specimen surface is assumed to be zero.

5.2 Materials

The indenter is assumed to be much harder than Si particle and Al matrix. Therefore it was modeled as a rigid body. The Al matrix is an elastic-plastic work hardening material. To study the influence of matrix, two Al matrixes with different yield strengths and work hardening behaviors are applied in this project. The compressive stress-strain relationship of a soft and a hard matrix are taken from T4 and T6 curves as shown in Fig.5.3 [134]. The plasticity used in Abaqus is in the form of true stress vs. plastic strain which can be transformed from the nominal stress vs. strain relationship in Fig.5.2 [132]. Elastic modulus of Al is 70 GPa. After transformation, the plasticity of Al matrix is presented in Fig. 5.3.

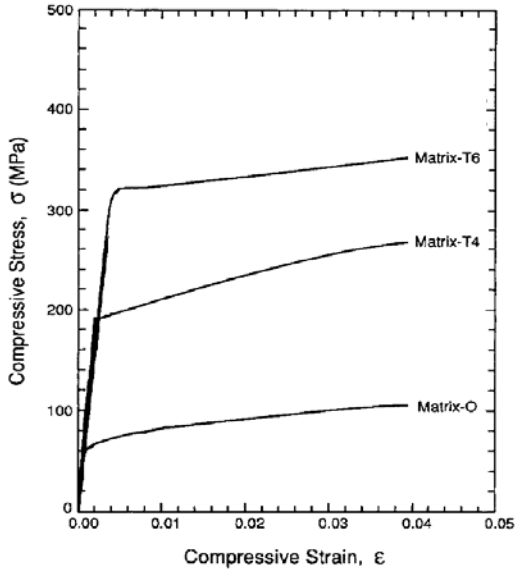

Fig. 5.2 Compressive stress vs. strain curves in different heat treatment: (i) annealed (O), (ii) naturally aged (T4) and (iii) peak-aged (T6) [134].

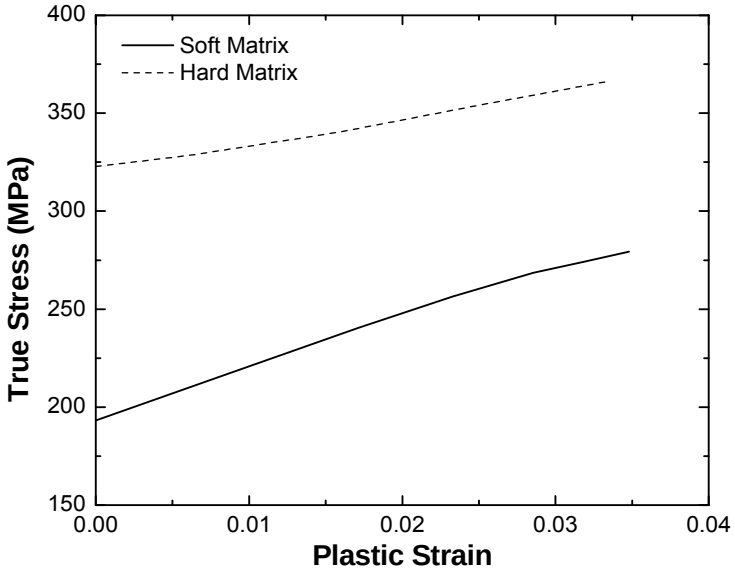

Fig. 5.3 True stress vs. plastic strain of Al matrix.

As to Si, indentation behavior includes yielding, indentation crack and phase transformation as briefly reviewed in Chapter 3. Some necessary mechanical properties used in the simulation for Si are Young's modulus, E = 150 GPa; Poisson's ratio, ν = 0.28; and yield strength, σ_Y = 7 GPa. After yielding, stress in Si is assumed to remain as 7 GPa.

5.3 Element Type and Mesh

For the application in contact problems second-order (quadratic shape functions) elements do not apply very well, often yielding to convergence problems, so only first-order (linear shape functions) elements are used. That is also the reason why quadrilateral-dominated elements are chosen, since first-order triangular elements are too stiff and exhibit slow convergence with mesh refinement. Reduced integrated elements are chosen to effectively eliminate volumetric locking with nearly incompressible material. Therefore, for both the Al matrix and Si particle, 4-node bilinear axisymmetric quadrilateral, reduced integration and hourglass control element type (CAX4R) is chosen. While for cohesive layer, a 4-node axisymmetric quadrilateral cohesive element (COHAX4) is the only suitable option for simulation [132]. A typical mesh of a 10 μm Si particle in Al matrix is given in Fig. 5.4. The minimal mesh size is 0.05 μm.

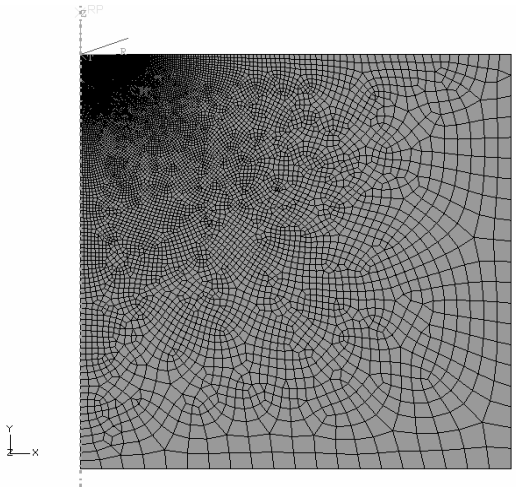

Fig. 5.4 Mesh of the Si particle/Al matrix with the indenter.

5.4 Verification of Materials, Element Type and Mesh

5.4.1 Verification in Al matrix

The developed FEA model is verified by comparing the simulated load-displacement curves with those obtained from experiments. Supplementary nanoindentation tests have been performed by directly applying Berkovich indenter on the Al matrix using Hysitron Ubi 1 Indentation. FEM simulations using both soft and hard matrixes are then carried out. Simulation results and experimental curves are compared in Fig. 5.5. It appears that hard matrix shows better consistency with experimental tests. However, the surface of

matrix (depth < 0.5 μm) may be harder than inner part due to surface oxidation and work hardening induced by mechanical polishing. Therefore soft matrix is used for FEM analysis. This judgment is verified in the following sections.

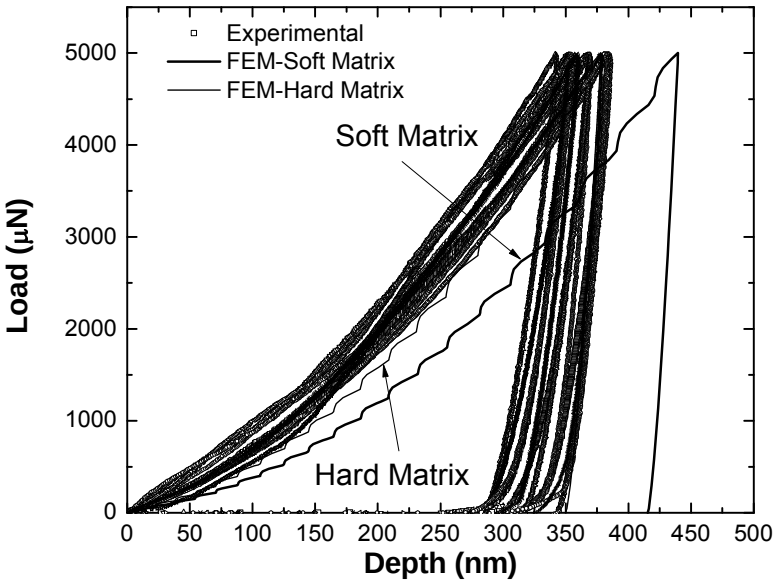

Fig.5.5 Comparison of FEA and experimental results for Al matrix. Solid lines are experimental curves.

5.4.2 Verification of Experimental Cases

Simulations of some typical cases are carried out to study the Al/Si interface debonding behavior. FEM simulations have been performed with both soft and hard matrixes. The shape of Si particle is generalized to be a cylinder with the dimensions listed in Table 5.1. The radius of the cylinder is obtained from the average cross section area,

$$R = \sqrt{\frac{\text{Volume}}{\pi \bullet \text{Height}}} \tag{5.1}$$

Case/Particle No.	Volume (μm^3)	Height (μm)	Radius (μm)
1/I-AB-9	17719.57	29.14	14
2b/I-AB-10	5396.59	19.4	9.4
3b/I-AB-3	3231.11	19.54	7.3

Table 5.1 Dimension of simplified model of typical Si particles for FEM simulation.

5.4.2.1 Case 1 Si Particle – Unchanged Interface

Simulation load-displacement curves are compared with the experimental curve in Fig. 5.6. The elastic deformation in surrounding Al matrix of both soft and hard matrixes are small even at highest indentation load (the vertical displacement of Si bottom is calculated as 53 nm for both soft and hard matrixes at 300 mN load) when the Si particle is big enough. Hence the Al matrix does little contribute to the indentation output and results in the overlapping of these two curves. The maximal indentation depth of FEM is smaller than of the experiment, while the residual depth, i.e. inelastic deformation, is almost the same as of the experiment. Considering the shift of pop-out and elbow, the difference in maximal indentation depths is owing to phase transformation of Si during loading and unloading. The difference is around 200 nm at 300 mN. Thus we can conclude that simulated load-displacement curve accords well with the experiment.

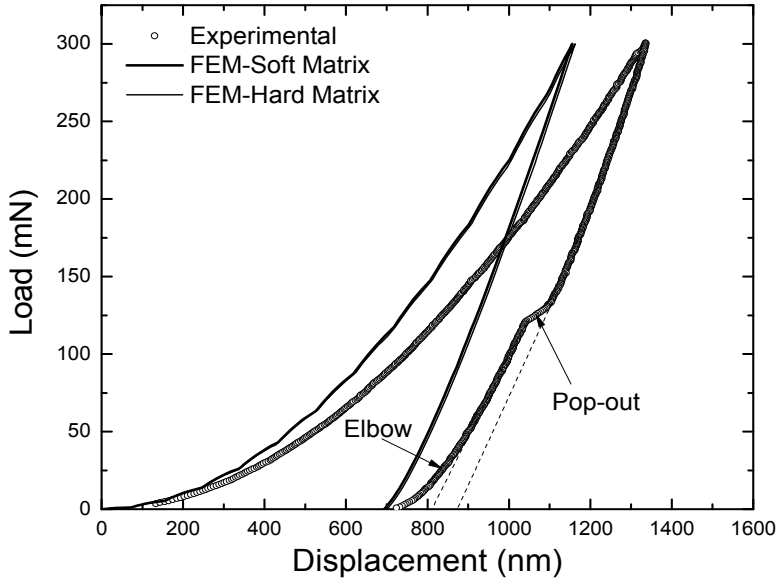

Fig. 5.6 Comparison of FEM and experimental results for a Case 1 Si particle.

5.4.2.2 Case 2b Si Particle – Global Debonding

Fig. 5.7 compares load-displacement curves and *dP/dh* obtained from experiments and FEM model. In Fig. 5.7a, the difference in maximal indentation depth between soft matrix and experimental curves is 330 nm. The difference in residual depth Δh_R between

soft matrix and experimental is around 160 nm. Hence the shift of Si phase transformation is around 170 nm, which is close to Case 1. Al matrix appears to yield near indentation depth of 1000 nm for soft matrix and experiment test. The peak in Fig. 5.7b (185 mN) indicating matrix yielding is found near the FEM calculated peak around 201 mN. In Fig. 5.8a, the surrounding Al matrix is plastically deformed severely. While for hard matrix, the *dP/dh* is monotone and FEM calculation verifies that there is no plastic deformation in Al matrix during the whole procedure.

The difference in residual depth Δh_R may contain the Si particle sinking induced by plastic deformation of Al matrix (50 nm in Fig. 5.8b) plus debonding of Al/Si interface. However, the maximal shear stress at Al/Si interface near surface (the first element of cohesive layer in Fig. 5.8b and Fig. 5.8c) is 207 MPa < 318 MPa (Table 2.1). Therefore, interface debonding does not seem to occur or only part of the interface debonds. On the other hand, Si particles are irregular in nature in this project and the stress distribution is much more complicated than the simplified FEM model. As to the traction-separation model, damage evolution is also unclear at present stage. To study interface debonding, more investigations are needed both experimentally and theoretically.

(a)

(b)

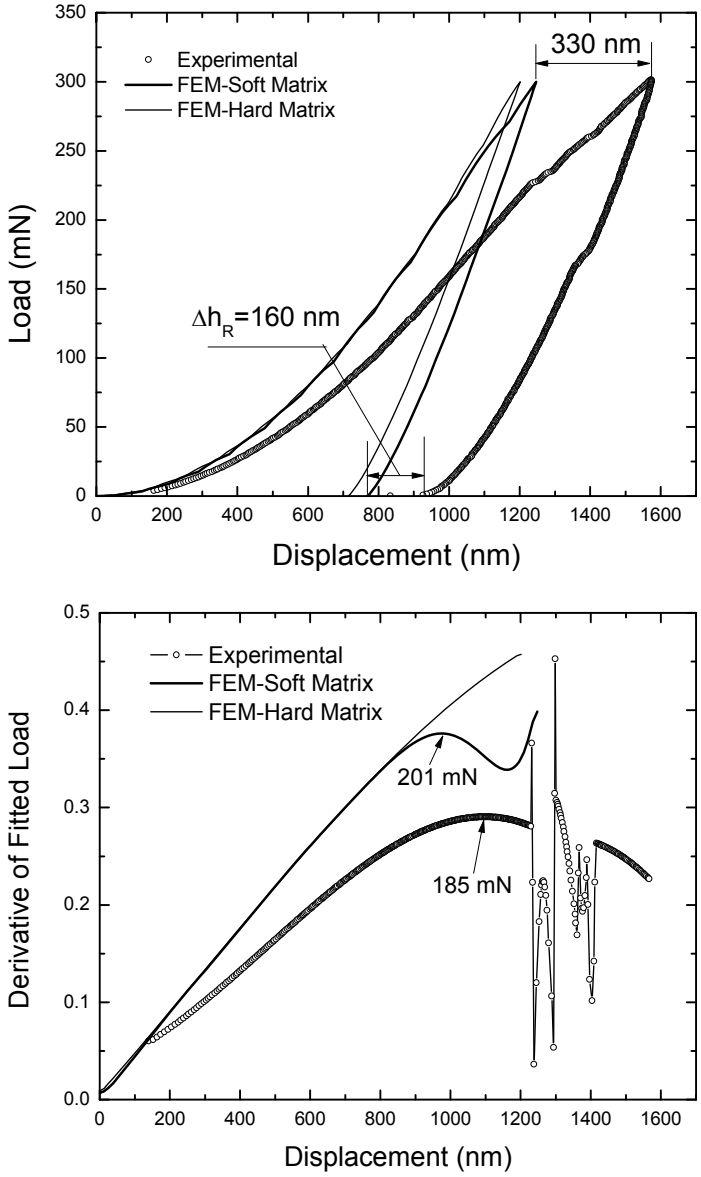

Fig. 5.7 Comparison of FEM and experimental results for a Case 2b Si particle: (a) load-displacement curves, (b*) dP/dh* curves upon loading.

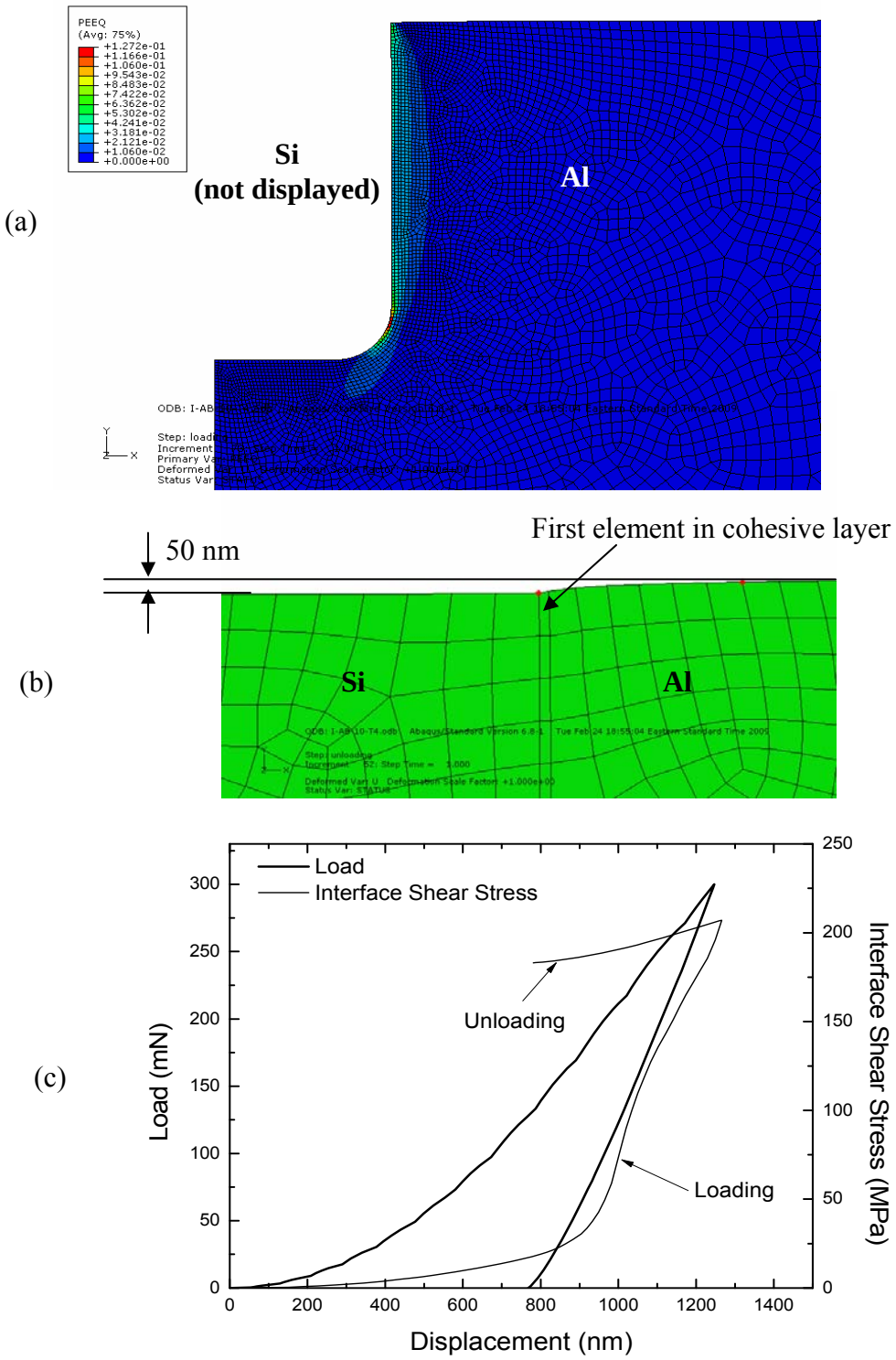

Fig. 5.8 FEM calculation of plastic deformation of surrounding Al matrix: (a) local view of Al matrix at maximal load; (b) local view of Al/Si interface near surface after unloading, the depth difference between Si and Al is around 50 nm; (c) shear stress of the first element in cohesive layer.

5.4.2.3 Case 3b Si Particle – Global Debonding with Fracture

A Si particle with global debonding and fracture is studied using the soft matrix with abovementioned conditions. Similar to Case 2b, yielding of Al matrix also occurs during loading as presented in Fig. 5.9b. Both the displacement and load show good consistency in FEM and experimental curves. Noticeably, no pop-out occurs during unloading while a small elbow at the end of unloading suggests that Si phase transformation may happen at the beginning of loading before fracturing. In view of the shift of elbow, load-displacement curve by FEM simulation is in good accordance with the experimental counterpart.

Fig. 5.9a appears that the experimental indentation undergoes matrix yielding and interface debonding. This can be explained with FEM results. Before Al matrix yielding, i.e., $P < 102$ mN, the interface shear stress is lower than 27 MPa. Along with matrix yielding, the interface shear stress increases with the indentation load till it reaches the threshold for debonding, 843 MPa at 252 mN in this case. The shear stress 843 MPa is in the range from 318 MPa to 1172 MPa (Table 2.1). Thus interface debonding occurs and Si particle sinks 262 nm. After that, Si particle may partially fracture due to the small radius and make a further displacement.

For other cases of Si particles such as local debonding and fracture with local debonding, due to the irregularity of these particles, it is difficult to generate a general model to fulfill the FEM simulation. Fracture cases are discussed in next section. To sum up, soft matrix is appropriate for FEM simulation and the results from the FEA model are in close agreement with the experimental results.

(a)

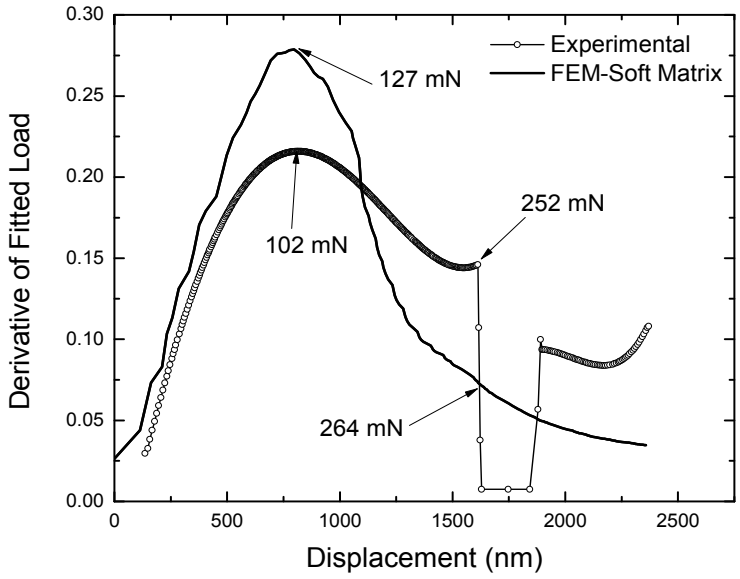

(b)

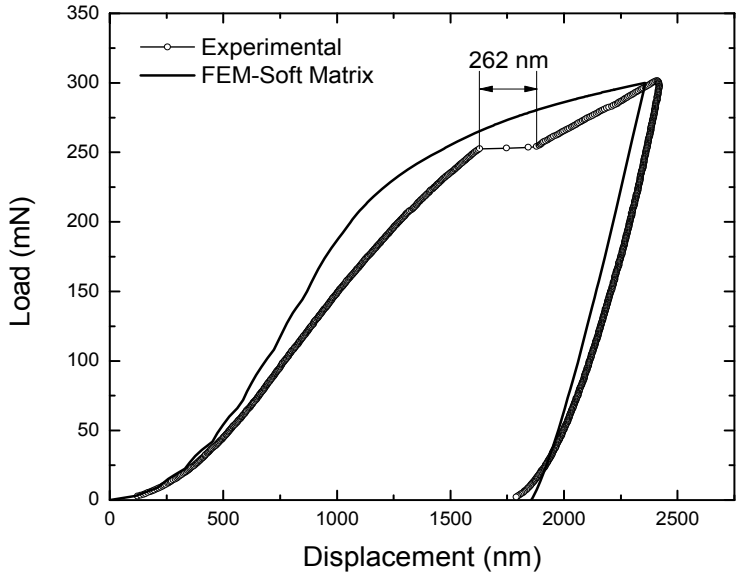

Fig. 5.9 Comparison of FEM and experimental results for a Case 3b Si particle: (a) load-displacement curves, (b*) dP/dh* curves upon loading.

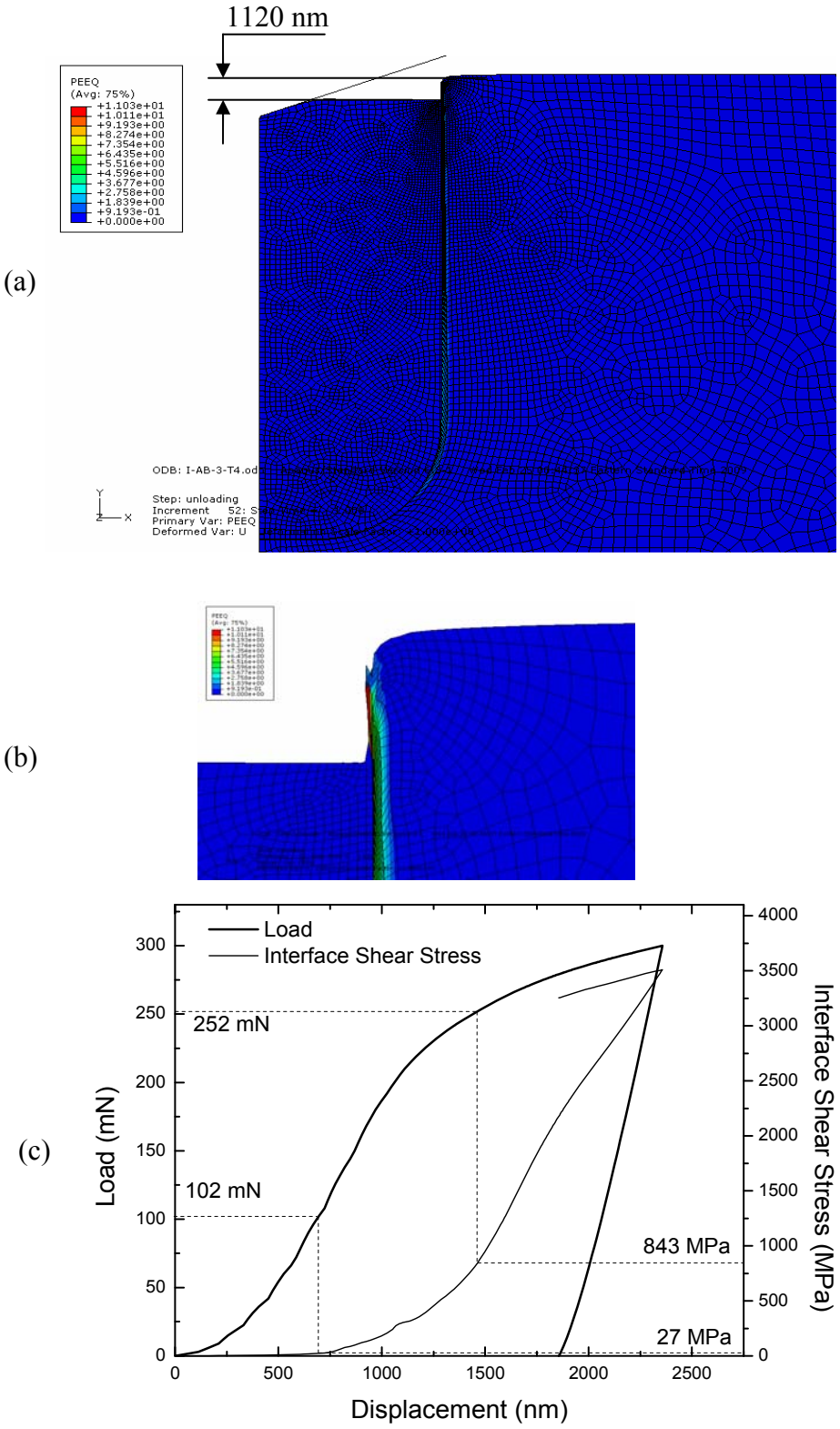

Fig. 5.10 FEM calculation of plastic deformation of surrounding Al matrix: (a) local view after unloading; (b) local view of Al/Si interface near surface after unloading, the depth difference between Si and Al is around 1120 nm; (c) shear stress of the first element in cohesive layer.

5.5 Al/Si Interface Debonding

5.5.1 Debonding Contour Plot

To acquire an overall understanding of the debonding behavior, the interface shear stress of different size and shape of Si particles has been computed. The height of Si particles for simulation is from 5 μm to 60 μm; radius of particles is 7.3 μm to 25 μm as listed in Table 5.2. For radius smaller than 7.3 μm, due to the high stress under sharp indenter, it is difficult to get convergence in FEM simulation and thus the lower limit of radius is 7.3 μm. The maximal shear stresses of the first element of cohesive layer are given as the interface shear stress in Table 5.2. The mark "F" means that before indentation load reaches 300 mN, the particle fractures first (Section 5.6) and then will not be considered in this section. A contour plot of the interface shear stress is drawn in Fig. 5.11. Below the contour line of 318 MPa, the calculated interface shear stress is smaller than 318 MPa. The dimension of particles without debonding (Case 1), and particles with global debonding (Case 2b & 3b) from experiments are superposed on the contour plot. Other cases such as local debonding with fracture are not presented in Fig. 5.11.

The global debonding Si particles are located below contour line of 318 MPa in the contour plot, which means the debonding shear stress is in a good agreement with the atomic simulation by Noreyan et al [40]. For hard matrix, interface shear stress is lower than of soft matrix when height is smaller than 25 μm and two particles above the contour line will not debond in hard matrix.

5.5.2 Influence of Morphology of Particles on Debonding Behavior

The relationship between morphology of Si particles and calculated interface shear stress is given in Fig. 5.12. The interface shear stress tends to be higher for particles with smaller size, lower aspect ratio and higher sphericity for both soft and hard matrixes.

Height (μm)	Radius (μm)	Size (μm)	Aspect Ratio	Sphericity	Interface Shear Stress at 300 mN (MPa)		Fracture Load at K_{ic}'=0.9 MPa$\sqrt{m}$ (mN)		Fracture Stress at K_{ic}'=0.9 MPa$\sqrt{m}$ (MPa)		Plastic Load for Al Matrix (mN)		Plastic Stress for Al Matrix (MPa)	
					Soft Matrix	Hard Matrix	Soft Matrix	Hard Matrix	Soft Matrix	Hard Matrix	Soft Matrix	Hard Matrix	Soft Matrix	Hard Matrix
5.00	7.30	5.65	0.34	0.80	F	F	42.72	49.65	255.20	296.59	11.91	23.30	71.12	139.16
5.00	10.00	7.03	0.25	0.72	F	F	42.77	49.42	136.14	157.32	14.14	22.67	45.02	72.15
5.00	15.00	9.29	0.17	0.62	F	F	44.05	50.92	62.32	72.04	15.18	25.89	21.47	36.62
5.00	20.00	11.30	0.13	0.54	F	F	44.17	51.03	35.15	40.60	15.06	26.63	11.98	21.19
5.00	25.00	13.15	0.10	0.48	F	F	43.28	49.94	22.04	25.43	15.37	25.72	7.83	13.10
10.00	7.30	7.25	0.68	0.90	1916.19	F	NF	187.02	NF	1117.11	49.71	97.71	296.94	583.66
10.00	10.00	8.98	0.50	0.86	F	F	140.17	166.04	446.18	528.53	56.27	98.46	179.11	313.40
10.00	15.00	11.81	0.33	0.79	F	F	140.82	165.67	199.23	234.38	55.37	85.37	78.33	120.77
10.00	20.00	14.33	0.25	0.72	F	F	139.99	164.45	111.40	130.87	55.06	95.75	43.82	76.20
10.00	25.00	16.65	0.20	0.66	F	F	139.14	163.36	70.86	83.20	57.81	96.25	29.44	49.02
15.00	7.30	8.34	1.03	0.91	1847.00	470.00	NF	NF	NF	NF	63.47	123.47	379.11	737.50
15.00	10.00	10.32	0.75	0.90	298.50	47.00	NF	NF	NF	NF	123.87	207.87	394.27	661.65
15.00	15.00	13.55	0.50	0.85	F	12.00	276.63	NF	391.35	NF	123.56	213.56	174.80	302.13
15.00	20.00	16.44	0.38	0.80	F	4.20	278.48	NF	221.60	NF	125.04	215.04	99.51	171.13
15.00	25.00	19.09	0.30	0.75	F	1.10	279.26	NF	142.23	NF	119.36	209.36	60.79	106.63
25.00	7.30	9.93	1.71	0.87	365.60	343.00	NF	NF	NF	NF	81.47	135.47	486.63	809.18
25.00	10.00	12.27	1.25	0.90	116.00	32.50	NF	NF	NF	NF	144.29	240.29	459.29	764.87
25.00	15.00	16.11	0.83	0.89	10.90	11.00	NF	NF	NF	NF	NP	NP	NP	NP
25.00	20.00	19.53	0.63	0.87	5.00	2.00	NF	NF	NF	NF	NP	NP	NP	NP
25.00	25.00	22.67	0.50	0.84	2.70	2.70	NF	NF	NF	NF	NP	NP	NP	NP
35.00	7.30	11.13	2.40	0.83	294.50	294.00	NF	NF	NF	NF	81.47	135.47	486.63	809.18
35.00	10.00	13.75	1.75	0.87	82.70	28.70	NF	NF	NF	NF	137.95	245.95	439.12	782.90
35.00	15.00	18.03	1.17	0.89	10.00	10.00	NF	NF	NF	NF	NP	NP	NP	NP
35.00	20.00	21.86	0.88	0.89	4.60	4.60	NF	NF	NF	NF	NP	NP	NP	NP
35.00	25.00	25.37	0.70	0.88	2.40	2.40	NF	NF	NF	NF	NP	NP	NP	NP
45.00	7.30	12.12	3.08	0.79	266.00	296.00	NF	NF	NF	NF	78.00	138.00	465.91	824.30
45.00	10.00	14.96	2.25	0.83	87.90	30.00	NF	NF	NF	NF	148.38	250.38	472.30	796.97
45.00	15.00	19.62	1.50	0.87	9.40	9.40	NF	NF	NF	NF	NP	NP	NP	NP
45.00	20.00	23.78	1.13	0.89	4.20	4.00	NF	NF	NF	NF	NP	NP	NP	NP
45.00	25.00	27.60	0.90	0.89	4.20	2.00	NF	NF	NF	NF	NP	NP	NP	NP
60.00	7.30	13.35	4.11	0.74	264.50	294.00	NF	NF	NF	NF	78.00	138.00	465.91	824.30
60.00	10.00	16.48	3.00	0.79	128.10	52.00	NF	NF	NF	NF	163.02	271.02	518.91	862.69
60.00	25.00	30.39	1.20	0.88	3.10	1.50	NF	NF	NF	NF	NP	NP	NP	NP

Table 5.2 FEM simulation results (F: Fractured; NF: Non-fractured; NP: No plastic deformation)

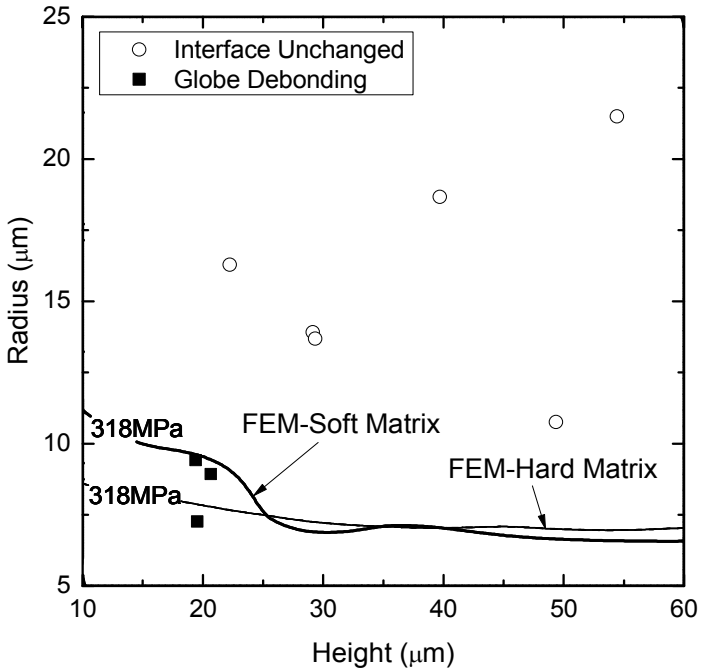

Fig. 5.11 A contour plot of Al/Si interface debonding. The z-axis denotes interface shear stress in Table 5.2. Solid marks are Si particle with global debonding (Case 2b & 3b). Circular dots are particles without sinking/debonding (Case 1).

(a)

(b)

(c)

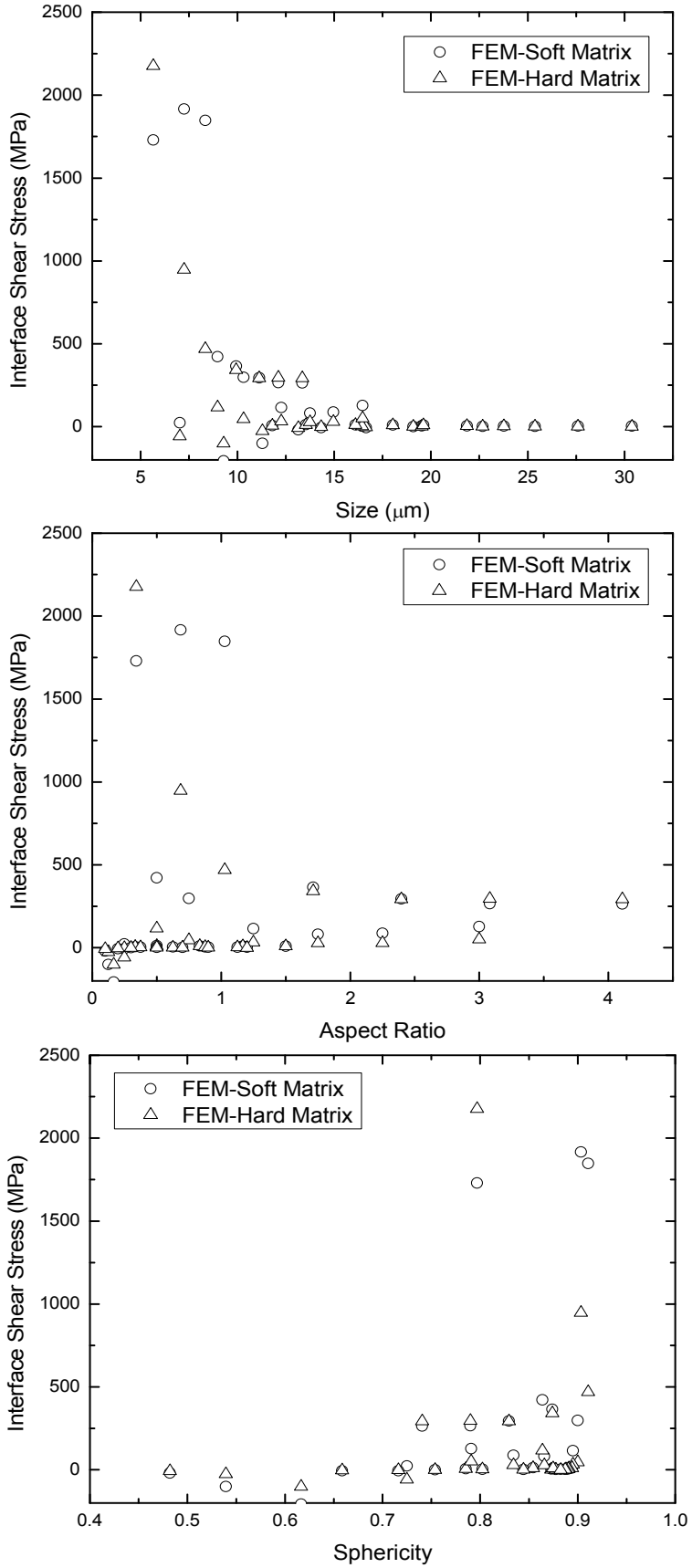

Fig. 5.12 The relationship between particle morphology and interface shear stress. (a) 3D size, (b) 3D aspect ratio and (c) sphericity.

5.6 Si Particle Fracture

5.6.1 Fracture Model of Si Particles

For Case 4 Si particles which are totally broken, the following fracture toughness model shown in Fig. 5.13 is proposed to determine whether the particle fractures or not by applying Eq. 2.1. The radial crack depth is in the same order of the indentation impression as shown in Fig 5.13b [103]. For mode I loading, K_{IC} is 0.9 MPa$\sqrt{m}$ for Silicon. Here we take the indentation depth as the crack length a. A variable $K_{IC}' = Y\sigma\sqrt{\pi a}$ is introduced: σ is tensile stress at the centre bottom of the particle as shown in Fig 5.13b and a is the crack length. The distance between the indent and the bottom of the particle is more than 5 times larger than a. Therefore, σ can be taken as a far field stress. If $K_{IC}' >$ 0.9 MPa$\sqrt{m}$ during the indentation loading procedure, we assume that fracture of Si particle occurs.

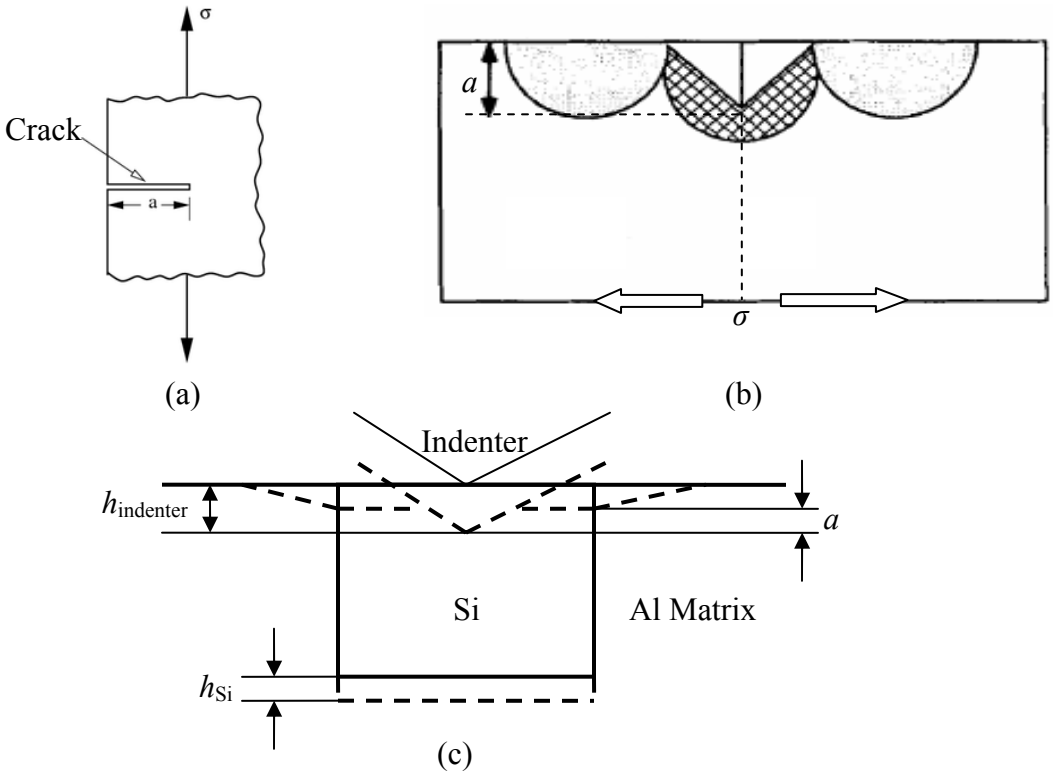

Fig. 5.13 Proposed fracture mechanism of Si particles under indentation. (a) Griffith fracture model; (b) proposed Berkovich fracture model; (c) calculation of crack depth of Si particle in Al matrix, where dashed lines are of particle and indenter at 300 mN load. The crack depth a is the displacement of indenter $h_{indenter}$ deducted by the displacement of the whole particle h_{Si}.

5.6.2 Fracture Contour Plot

First, tensile stress σ at the bottom of centre line, the displacement of indenter h_{indenter} and displacement of the particle h_{Si} during loading are computed. Next, tensile stress σ and crack depth $a = h_{\text{indenter}} - h_{\text{Si}}$ are used to calculate $K_{\text{IC}}' = Y\sigma\sqrt{\pi a}$, as presented in Fig. 5.14. After that, load at $K_{\text{IC}}' = 0.9\ \text{MPa}\sqrt{\text{m}}$ is derived and defined as fracture load and is used to calculate fracture stress. Fracture stress is defined as the fracture load over the section area of the Si particle under an indenter.

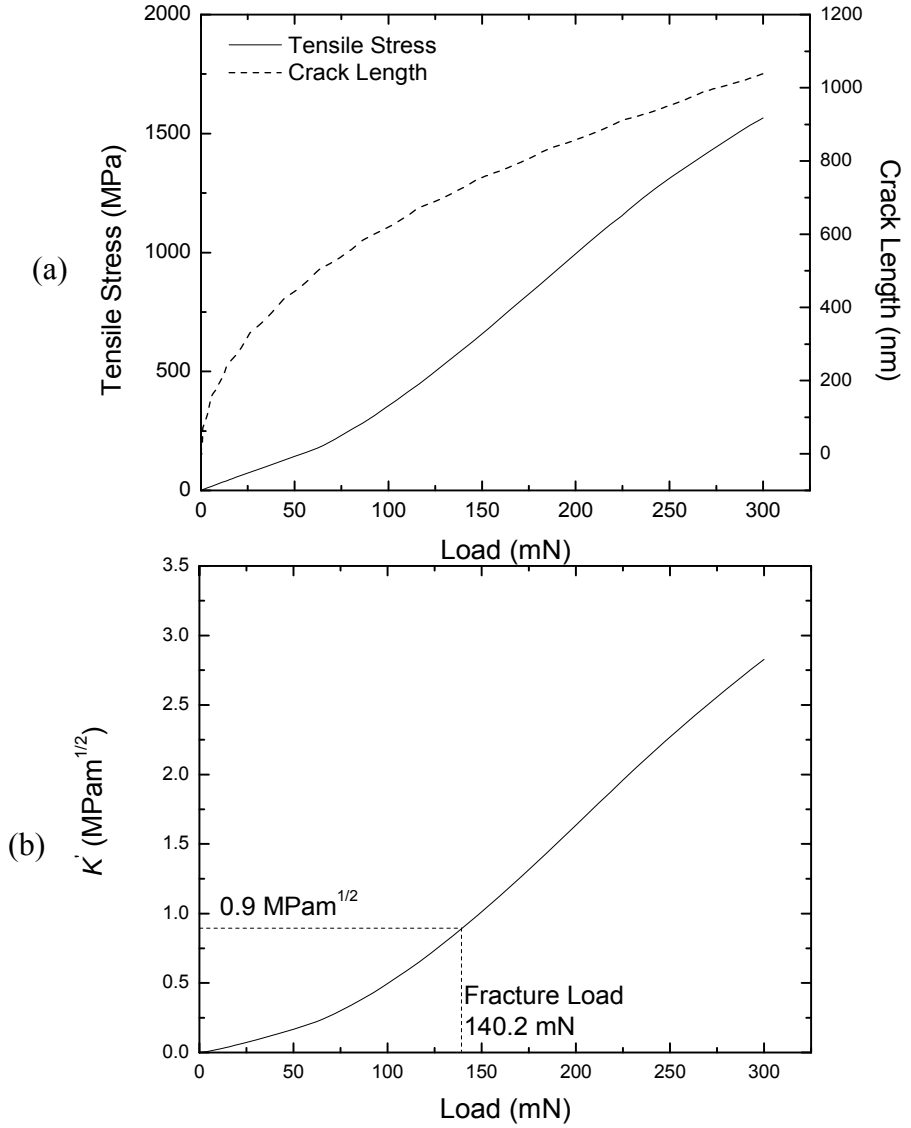

Fig. 5.14 Fracture toughness FEM calculation: (a) tensile stress and crack depth; (b) $K_{\text{IC}}' = Y\sigma\sqrt{\pi a}$. The height and radius of the simulated Si particle are 10 μm.

After abovementioned calculations are finished for all different particles, a fracture contour plot is plotted with the height, radius and fracture load as demonstrated in Fig. 5.15. To the left of the contour line of 300 mN, $K_{IC}' > 0.9$ MPa$\sqrt{m}$ and Si particles in this area will fracture with a load up to 300 mN. The experimental broken particles and interface unchanged particles are plotted as dots by their height and radius. Fig. 5.15 demonstrates that experimental fractured Si particles locate to the left of the contour line. With the experimental verification, the proposed fracture mechanism of Si particles in Al matrix has been proved to be a successful model and may be used to study other inclusion/matrix systems.

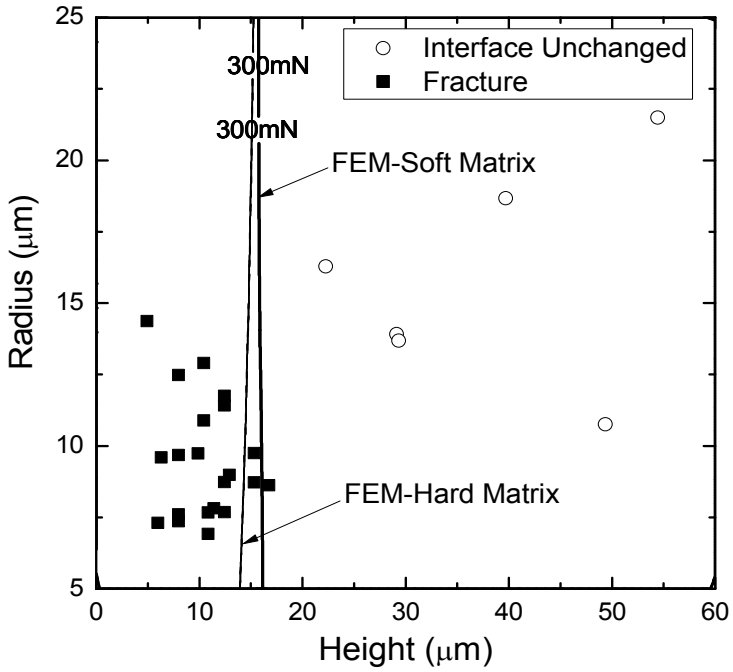

Fig. 5.15 A contour plot for fracture of Si particles. The z-axis denotes fracture load in Table 5.2. Solid marks are experimental fracture Si particles (Case 4) and circular dots are unchanged particles (Case 1).

5.6.3 Influence of Morphology of Particles on Fracture Behavior

Whether a Si particle fractures or not under loading is determined by its dimension as shown in Fig. 5.15. For fracture particles, it is necessary to study when fracture happens and how particle morphology affects its fracture behavior. As discussed in Chapter 4, particle morphology makes a great contribution to fracture stress as shown in Fig. 4.12.

In this section, FEM analysis has been done to study the morphology effect further. During the FEM simulation of indentation loading, the relationship between particle morphology and fracture stress is investigated and shown in Fig. 5.16. Obviously, Si particles in hard matrix show higher resistance to fracture than in soft matrix in the fewer fracture particle quantity and higher fracture stress. Similar to experimental results, the 3D size effect on fracture stress from FEM calculation is not explicit. On the contrary, FEM data of 3D aspect ratio and sphericity of Si particles accord well with experimental data and both exhibit a distinct tendency, i.e., the higher the 3D aspect ratio/sphericity, the higher stress needed to break the particle. However, due to the random distribution and orientation of Si particles in Al matrix, 3D aspect ratio is not a controllable parameter except that the aspect ratio of all Si particles is always 1, i.e., all particles are roughly round. The impossibility of such assumption means that the importance of the particle sphericity to resist-fracture ability is greater than the 3D aspect ratio.

Fracture loads of different simulation particles against particle height are also plotted in Fig. 5.17. The fracture load is found to be in direct ratio to the height of Si particles. The experimental fracture load is smaller than of the FEM results. This may be due to the irregular shape of Si particles and the difficulty of making indentation at the center line of the particle.

(a)

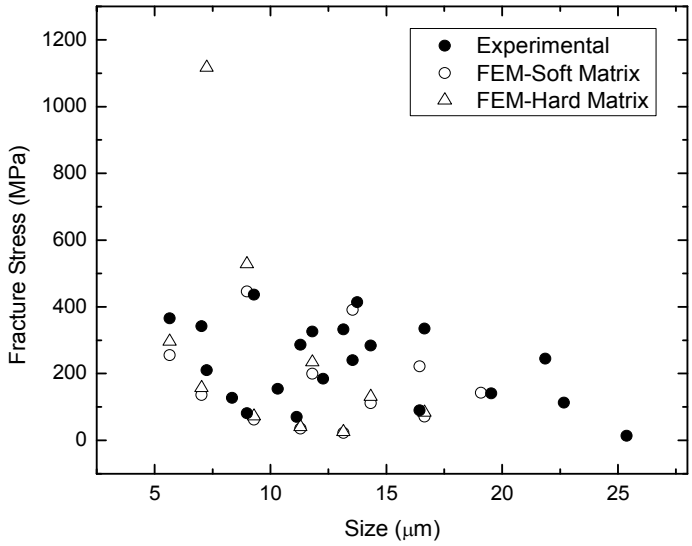

(b)

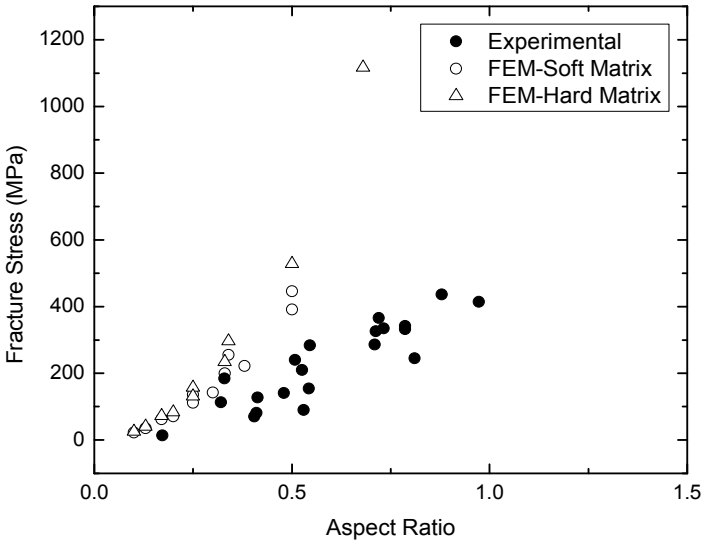

(c)

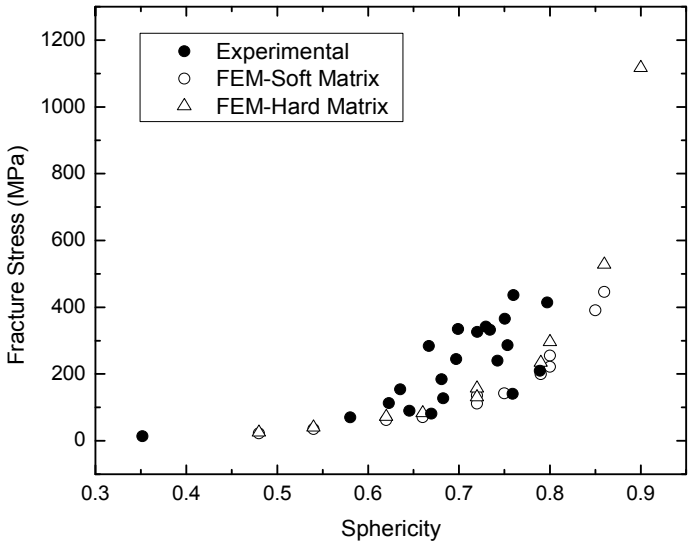

Fig. 5.16 The relationship between particle morphology and fracture behavior: (a) fracture stress vs. 3D size; (b) fracture stress vs. 3D aspect ratio; (c) fracture stress vs. sphericity.

3

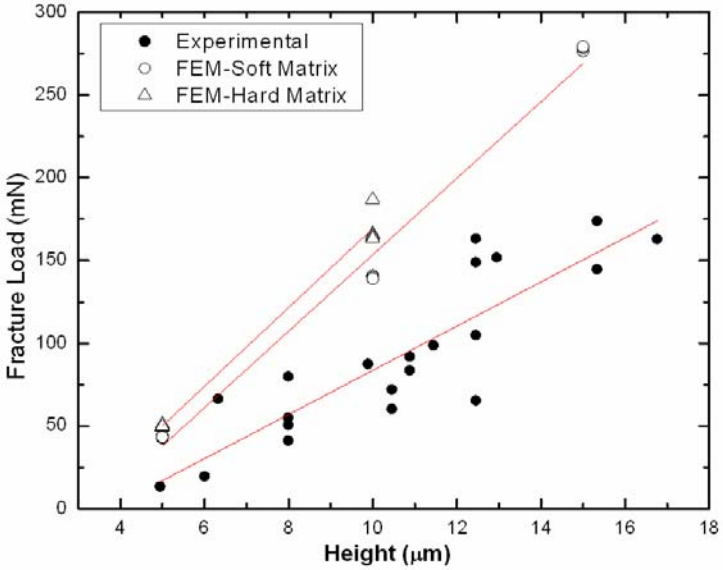

Fig. 5.17 FEM computed fracture load vs. particle shape.

5.7 Plastic Deformation in Al Matrix

As reviewed in Chapter 2, plastic deformation can cause fragmentation of silicon particles and subsurface delamination. The overall result is a dynamic change of the tribological properties of the material, which are of primary importance for its performance. Several authors have experimentally investigated the subsurface layer deformation in Al alloys. However, despite the intensive research in this area, the mechanism of plastic deformation induced crack formation and delamination leading to local structure is still under studying. In this section, plastic deformation in Al matrix around Si particle under indentation and its relationship to particle morphology factors are investigated.

5.7.1 Plastic Deformation Contour Plot

In this project, only plastic deformation of Al matrix is studied. The energy dissipated by rate-independent and rate-dependent plastic deformation (ALLPD) is used to obtain the threshold load for plastic deformation in Al matrix. A typical plastic energy versus load curve is shown in Fig. 5.18. The plastic energy in Al matrix is zero until indentation load reaches a threshold load of 127 mN. If indentation load is higher than the threshold load, plastic deformation occurs. Here we name the threshold load as plastic load. Accordingly,

the plastic load over the section area of Si particle under indenter is defined as plastic stress. The plastic loads of different simulated particles are listed in Table 5.2. Noticeable, for fractured Si particles, the plastic load is always smaller than fracture load which means plastic deformation in Al matrix occurs before Si particle fracturing.

.

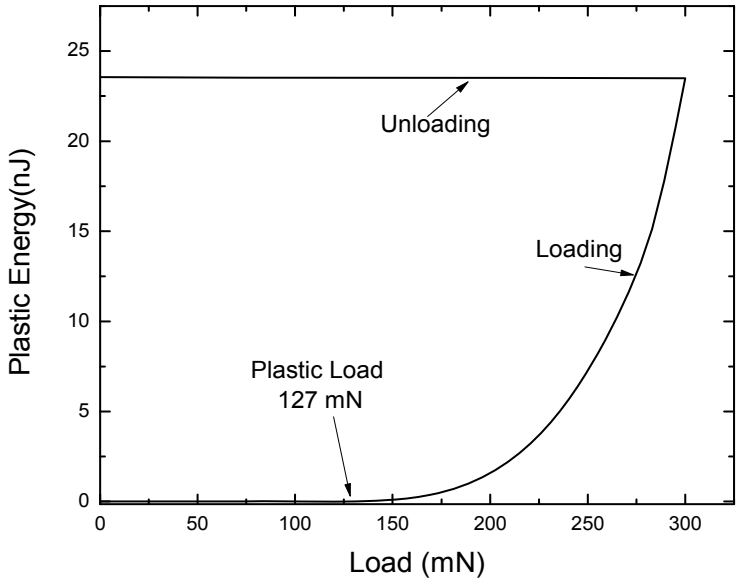

Fig. 5.18 Plastic energy in Al matrix from FEM computation.

The plastic load has been derived from the plastic energy curve with a maximal load of 300 mN for different particles. A contour plot of the plastic load is drawn in Fig. 5.19. Experimental fracture Si particles (Case 4) and interface unchanged particles (Case 1) are superposed in the plot. The top right areas outlined by contours are non-plastic deformation area. Fig. 5.19 demonstrates that plastic deformation in soft Al matrix is higher than in hard matrix. For example, plastic deformation occurs in soft matrix for most Case 1 particles. To the contrary, plastic deformation does not exist in hard matrix for most Case 1 particles. For smaller fractured particles such as Case 4, plastic deformation in both soft and hard matrixes occurs before the Si particle fracturing.

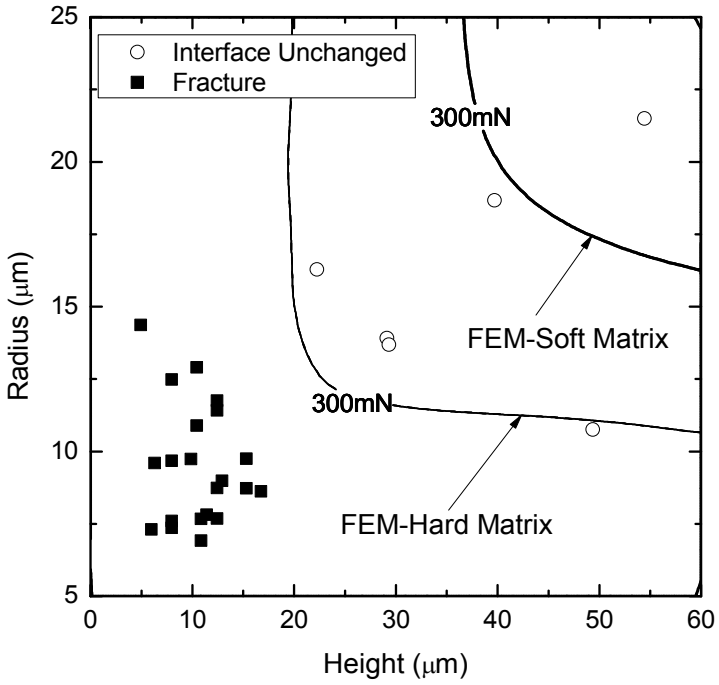

Fig. 5.19 A contour plot of plastic deformation in Al matrix. The z-axis denotes plastic load in Table 5.2. Solid marks are experimental fracture Si particles (Case 4) and circular dots are unchanged particles (Case 1).

5.7.2 Influence of Morphology of Particles on Plastic Deformation in Al Matrix

The relationship between particle morphology and plastic deformation in Al matrix is presented in Fig. 5.20. Apparently, the plastic stress of hard matrix is higher than soft matrix. It seems that harder matrix can hold higher load before plastic deformation occurs. Fig. 5.20 appears that the 3D size effect on plastic stress does not have a distinct trend. The fracture stress increases sharply with the increase of 3D aspect ratio and reaches a platform at the ratio around 1 as shown in Fig. 5.20b. Considering the definition of 3D aspect ratio (h/D) in Table 4.1, the plate like particles is easily plastically deformed. With the increase of 3D aspect ratio, the shapes of particles change from plate like to roughly round and gradually needle like. However, there is no sharp difference in plastic stress between roughly round particles and needle like particles. The plastic stress also seems to be sensitive to the sphericity of Si particles as shown in Fig. 5.20c. The plastic stress shows a general growth over particle sphericity. To sum up, high sphericity of Si particle is desired and low 3D aspect ratio should be avoided to resist plastic deformation.

(a)

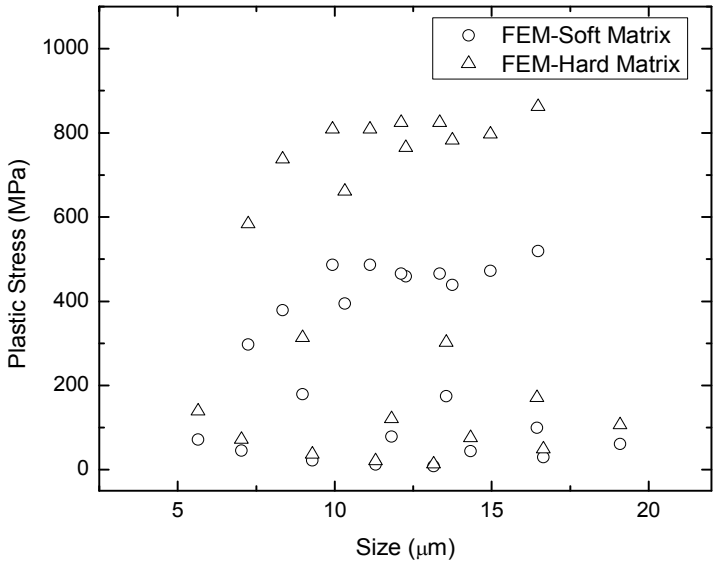

(b)

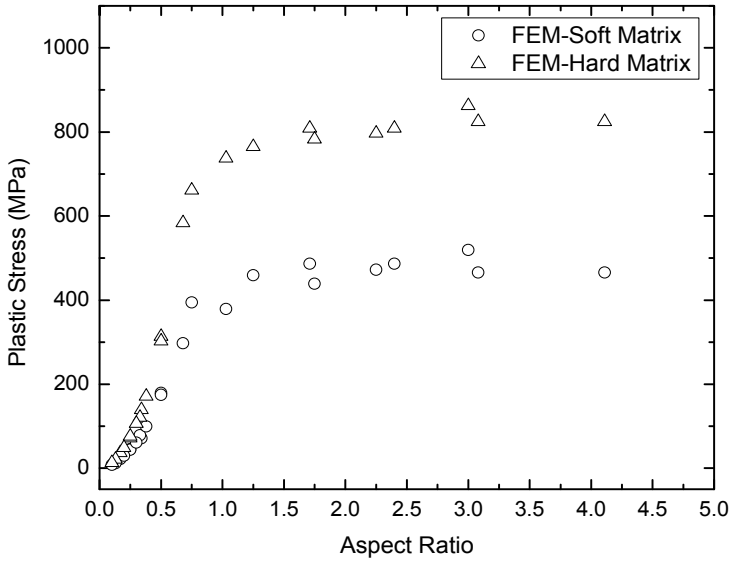

(c)

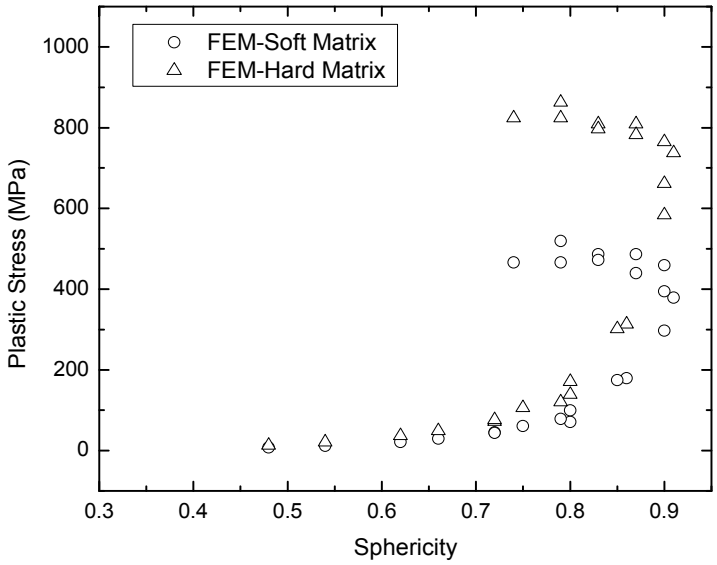

Fig. 5.20 The relationship between particle morphology and plastic deformation in Al matrix: (a) 3d size, (b) 3d aspect ratio, (c) sphericity.

5.8 Summary

In above sections, FEM analyses have been done for instrumented indentation at Si particles in Al matrix. Interface strength, fracture of Si particles and plastic deformation of Al matrix have been investigated based on the morphology of Si particles and matrix heat treatments. An indentation map is constructed with axes of particle height and radius to display all the deformations under loading as shown in Fig.5.21. For example, for a Si particle with 10 μm in both height and radius, during the loading procedure, plastic deformation in Al matrix occurs first at 56.3 mN then the particle fractures at 140.2 mN (Table 5.2). From the indentation map, we can see that this particle is located in all the three undesired areas. To avoid such damages under load of 300 mN, the particle size should be located in the top right area outline by the plastic deformation contour line of the soft matrix, for instance, 50 μm in height and 20 μm in radius according to the map. On the other hand, to reduce the influence of the irregular shape of real Si particles, higher sphericity is preferred, i.e., the Si particles should be round, rather than plate like, needle like or sharp edged. In addition, harder matrix can offer better resistance to interface debonding, particle fracture and matrix plastic deformation.

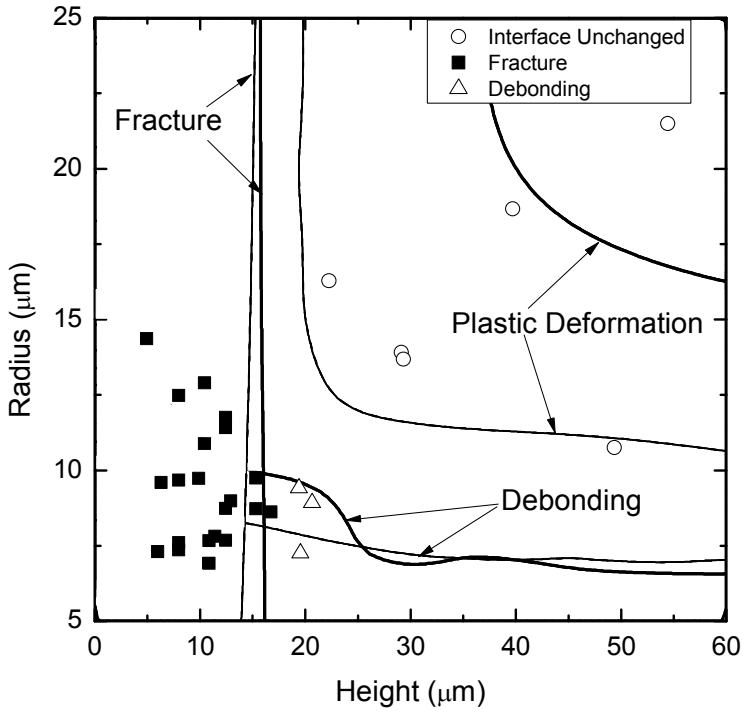

Fig. 5.21 An indentation map shows the Al/Si interface debonding, Si particle fracture and Al matrix plastic deformation. Maximal indentation load is 300 mN.

A deficiency for using the map to analyze UMW behavior is that the load is quasi-statistical along one direction. Further research is needed on the dynamic behavior such as sliding test, formation of MML, fatigue test, etc. However, the accordance between experimental results and FEM analysis show that this approach answers some questions such as inclusion fracture mechanism and interface debonding behavior of two phase materials. This methodology can also contribute to analyzing other MMC materials. For example, sharp wear debris or abrasive particles can act as moving indenters and therefore the fracture behavior of particles (inclusions) in matrix can be determined both statically and dynamically with FEM study. This understanding is helpful to study wear properties of the material. Furthermore, it is possible that the morphology of particles (inclusions) and the property of matrix can be designed intentionally with this method to obtain high wear resistance. In a word, AlSi alloys with high sphericity Si particles and hard Al matrix will have high wear resistance.

CHAPTER 6 CONCLUSIONS AND FUTURE WORK

Al/Si interface strength and fracture of primary Si particles in an AlSi alloy have been investigated at micro scale using a combination of nanoindentation, serial sectioning, numerical derivative analysis and finite element method. The indentation tests were carried on with a fixed 300 mN maximal load and a Berkovich pyramid indenter. Based on the test results and FEM analysis, the following conclusions and future works are drawn.

6.1 Conclusions

Nanoindentations were performed on primary Si particles in a soft Al matrix. Indentation behavior such as interface debonding, Si particle fracture and the mixing of interface debonding and particle fracture were characterized by SEM/SPM, first derivative analysis of load-displacement curves and 3D structure of the particles from a serial sectioning technique. Based on this classification, how a particle reacts under indentation, such as break, sink, and tilt or keeps the original status in a particle/matrix system was successfully and effectively determined. The underlying mechanism can then be used to analyze sliding wear mechanism of AlSi alloys.

First derivative analysis was used to study the overall range of load-displacement loading curve for the first time. By applying a subsection polynomial fitting, characteristic events, such as cracking, debonding, matrix yielding were successfully extracted from indentation load-displacement curves. With this new approach, micro/nano investigations in mechanical and metallurgy properties are feasible in particle/matrix systems and MMCs.

Through the serial sectioning method, 3D information of Si particles was obtained. 3D morphology results of cracked Si particles showed that particles with high sphericity can hold higher load. Accompanying with indentation results, 3D structure can be utilized for studying wear resistance and mechanical properties of MMCs.

Indentation fracture toughness was calculated for the undamaged Si particles. The fracture toughness of these undamaged Si particles was almost 30% higher than its bulk material counterpart. According to the analysis, Si particles sink to some extent under applied load and recover to their original positions elastically. The recoverable sink-in of Si particles was observed in FEM simulation.

The Al/Si interface strength, fracture mechanism of Si particles and plastic deformation in Al matrix have been studied mainly from a morphology point of view using finite element method. A facture model of particle in matrix based on Mode I fracture toughness was proposed and verified with experimental data successfully. It was also found that higher sphericity of Si particles and harder Al matrix are favorable to the resistance to interface debonding, fracture of Si particles and plastic deformation in Al matrix.

6.2 Future Work

Sliding wear experiments such as pin-on-disk are recommended to be performed to study the interface failure, fracture of Si particles, morphology of the Si particles, and different matrixes in a dynamic circumstance. FEM simulation in interface debonding is still need improving because the damage evolution criterion is unclear and will be continually investigated. Dynamic FEM simulation for wear mechanism of inclusion/matrix system may be another research interest. By these approaches, the wear mechanism of the two phase AlSi alloys can be understood in a greater detail. To sum up, the methodology used in this work not only can be carried out in MMCs, but also offer a promising approach to study multi phase materials at micro scale.

REFERENCES

1. American Society of Metals, ASM Handbook Online, A., *Vol. 18, Friction, lubrication and wear technology.* ASM International, 1992.
2. Rigney, D., *Fundamentals of Friction and Wear of Materials.* ASM, Metals Park, Ohio, 1980:p.1-12.
3. Dautzenberg, J.H., *The Role of Dynamic Recrystallization in Dry Sliding Wear.* Wear, 1980. **60**(2): p. 401-411.
4. Kuo, S.M. and D.A. Rigney, *Sliding Behavior of Aluminum.* Materials Science and Engineering a-Structural Materials Properties Microstructure and Processing, 1992. **157**(2): p. 131-143.
5. Rainforth, W.M., R. Stevens, and J. Nutting, *Deformation Structures Induced by Sliding Contact.* Philosophical Magazine a-Physics of Condensed Matter Structure Defects and Mechanical Properties, 1992. **66**(4): p. 621-641.
6. Yang, Z.Y., M.G.S. Naylor, and D.A. Rigney, *Sliding Wear of 304 and 310 Stainless-Steels.* Wear, 1985. **105**(1): p. 73-86.
7. Zhang, J. and A.T. Alpas, *Delamination Wear in Ductile Materials Containing 2nd Phase Particles.* Materials Science and Engineering a-Structural Materials Properties Microstructure and Processing, 1993. **160**(1): p. 25-35.
8. Qian, L., H. Toda, K. Uesugi, T. Ohgaki, M. Kobayashi, and T. Kobayashi, *Three-dimensional visualization of ductile fracture in an Al-Si alloy by high-resolution synchrotron X-ray microtomography.* Materials Science and Engineering a-Structural Materials Properties Microstructure and Processing, 2008. **483**: p. 293-296.
9. Riahi, A.R. and A.T. Alpas, *Fracture of silicon-rich particles during sliding contact of Al-Si alloys.* Materials Science and Engineering a-Structural Materials Properties Microstructure and Processing, 2006. **441**(1-2): p. 326-330.
10. Gall, K., N. Yang, M. Horstemeyer, D.L. McDowell, and J.H. Fan, *The debonding and fracture of Si particles during the fatigue of a cast Al-Si alloy.*

Metallurgical and Materials Transactions a-Physical Metallurgy and Materials Science, 1999. **30**(12): p. 3079-3088.

11. Bai, B.N.P. and S.K. Biswas, *Effect of Load on Dry Sliding Wear of Aluminum-Silicon Alloys.* Asle Transactions, 1986. **29**(1): p. 116-120.
12. Bai, B.N.P. and S.K. Biswas, *Subsurface Deformation in Dry Sliding of Hypo-Eutectic Al-Si Alloys.* Journal of Materials Science, 1984. **19**(11): p. 3588-3592.
13. Chiu, C., J.D. Embury, and T. Castillo, *Metallography of Adhesive Wear in Aluminum-Alloys.* Metallography, 1987. **20**(1): p. 99-112.
14. Bai, B.N.P. and S.K. Biswas, *Mechanism of Wear in Dry Sliding of a Hypoeutectic Aluminum-Alloy.* Lubrication Engineering, 1987. **43**(1): p. 57-61.
15. Suh, N.P., *Delamination Theory of Wear.* Wear, 1973. **25**(1): p. 111-124.
16. Fu, X.Y., T. Kasai, M.L. Falk, and D.A. Rigney, *Sliding behavior of metallic glass - Part I. Experimental investigations.* Wear, 2001. **250**: p. 409-419.
17. Alpas, A.T. and J.D. Embury, *The Role of Subsurface Deformation and Strain Localization on the Sliding Wear Behavior of Laminated Composites.* Wear, 1991. **146**(2): p. 285-300.
18. Alpas, A., H. Hu, and J. Zhang, *Plastic deformation and damage accumulation below the worn surfaces.* Wear, 1993. **162**(A): p. 188-195.
19. Perrin, C. and W.M. Rainforth, *Work hardening behaviour at the worn surface of Al-Cu and Al-Si alloys.* Wear, 1997. **203**: p. 171-179.
20. Modi, O.P., B.K. Prasad, A.H. Yegneswaran, and M.L. Vaidya, *Dry Sliding Wear Behavior of Squeeze Cast-Aluminum Alloy Silicon-Carbide Composites.* Materials Science and Engineering a-Structural Materials Properties Microstructure and Processing, 1992. **151**(2): p. 235-245.
21. Prasad, S.V. and K.R. Mecklenburg, *Friction Behavior of Ceramic Fiber-Reinforced Aluminum Metal-Matrix Composites against a 440c Steel Counterface.* Wear, 1993. **162**: p. 47-56.
22. ROHATGI, P., S. RAY, and Y. LIU, *Tribological properties of metal matrix-graphite particle composites.* International materials reviews, 1992. **37**(3): p. 129-149.

23. Sannino, A.P. and H.J. Rack, *Dry Sliding Wear of Discontinuously Reinforced Aluminum Composites - Review and Discussion.* Wear, 1995. **189**(1-2): p. 1-19.
24. Alpas, A.T. and J. Zhang, *Effect of Microstructure (Particulate Size and Volume Fraction) and Counterface Material on the Sliding Wear-Resistance of Particulate-Reinforced Aluminum-Matrix Composites.* Metallurgical and Materials Transactions a-Physical Metallurgy and Materials Science, 1994. **25**(5): p. 969-983.
25. Venkataraman, B. and G. Sundararajan, *The sliding wear behaviour of Al-SiC particulate composites .1. Macrobehaviour.* Acta Materialia, 1996. **44**(2): p. 451-460.
26. Zhang, J. and A.T. Alpas, *Wear Regimes and Transitions in Al2o3 Particulate-Reinforced Aluminum-Alloys.* Materials Science and Engineering a-Structural Materials Properties Microstructure and Processing, 1993. **161**(2): p. 273-284.
27. Antoniou, R. and D.W. Borland, *Mild Wear of Al-Si Binary-Alloys during Unlubricated Sliding.* Materials Science and Engineering, 1987. **93**: p. 57-72.
28. Riahi, A.R., T. Perry, and A.T. Alpas, *Scuffing resistances of Al-Si alloys: effects of etching condition, surface roughness and particle morphology.* Materials Science and Engineering A, 2003. **343**(1-2): p. 76-81.
29. Chen, M., T. Perry, and A.T. Alpas, *Ultra-mild wear in eutectic Al-Si alloys.* Wear, 2007. **263**: p. 552-561.
30. Chen, M. and A.T. Alpas, *Ultra-mild wear of a hypereutectic Al-18.5 wt.% Si alloy.* Wear, 2008. **265**(1-2): p. 186-195.
31. Das, S., K. Varalakshmi, V. Jayaram, and S.K. Biswas, *Ultra mild wear in lubricated tribology of an aluminium alloy.* Journal of Tribology, 2007. **129**(4): p. 942-951.
32. Chen, M., X. Meng-Burany, T.A. Perry, and A.T. Alpas, *Micromechanisms and mechanics of ultra-mild wear in Al-Si alloys.* Acta Materialia, 2008. **56**(19): p. 5605-5616.
33. Dienwiebel, M., K. Pohlmann, and M. Scherge, *Origins of the wear resistance of AlSi cylinder bore surfaces studies by surface analytical tools.* Tribology International, 2007. **40**(10-12): p. 1597-1602.

34. Schneider, E. and D. Blossfeld, *2004-01-2917 Effect of Break-In and Operating Conditions on Piston Ring and Cylinder Bore Wear in Spark-Ignition Engines.* SAE TRANSACTIONS, 2004. **113**(3): p. 1357.

35. Caceres, C. and J. Griffiths, *Damage by the cracking of silicon particles in an Al-7Si-0.4 Mg casting alloy.* Acta Materialia, 1996. **44**(1): p. 25-33.

36. Li, J., A. Elmadagli, V.Y. Gertsman, J. Lo, and A.T. Alpas, *FIB and TEM characterization of subsurfaces of an Al-Si alloy (A390) subjected to sliding wear.* Materials Science and Engineering a-Structural Materials Properties Microstructure and Processing, 2006. **421**(1-2): p. 317-327.

37. Wang, Q., C. Caceres, and J. Griffiths, *Damage by eutectic particle cracking in aluminum casting alloys A356/357.* Metallurgical and Materials Transactions A, 2003. **34**(12): p. 2901-2912.

38. Harris, S., A. O'Neill, J. Boileau, W. Donlon, X. Su, and B. Majumdar, *Application of the Raman technique to measure stress states in individual Si particles in a cast AlSi alloy.* Acta Materialia, 2007. **55**(5): p. 1681-1693.

39. Inci, L., S. Tavoosfard, and V. Stoilov, *Microstructure evolution of Al-Si alloys under shear loading.* International Journal of Mechanics and Materials in Design, 2008. **4**(2): p. 197-203.

40. Noreyan, A., Y. Qi, and V. Stoilov, *Critical shear stresses at aluminum-silicon interfaces.* Acta Materialia, 2008. **56**(14): p. 3461-3469.

41. Needleman, A., *A Continuum Model for Void Nucleation by Inclusion Debonding.* Journal of Applied Mechanics-Transactions of the Asme, 1987. **54**(3): p. 525-531.

42. Xu, X.P. and A. Needleman, *Void Nucleation by Inclusion Debonding in a Crystal Matrix.* Modelling and Simulation in Materials Science and Engineering, 1993. **1**(2): p. 111-132.

43. Gall, K., N. Yang, M. Horstemeyer, D.L. McDowell, and F. Jinghong, *The debonding and fracture of Si particles during the fatigue of a cast Al-Si alloy.* Metallurgical and Materials Transactions A (Physical Metallurgy and Materials Science), 1999. **30A**(12): p. 3079-88.

44. Camacho, G.T. and M. Ortiz, *Computational modelling of impact damage in brittle materials.* International Journal of Solids and Structures, 1996. **33**(20-22): p. 2899-2938.
45. Xu, X.P. and A. Needleman, *Numerical simulations of dynamic crack growth along an interface.* International Journal of Fracture, 1996. **74**(4): p. 289-324.
46. Siegmund, T., N. Fleck, and A. Needleman, *Dynamic crack growth across an interface.* International Journal of Fracture, 1997. **85**(4): p. 381-402.
47. Rigney, D.A., *Viewpoint Set on Materials Aspects of Wear - Introduction.* Scripta Metallurgica Et Materialia, 1990. **24**(5): p. 799-803.
48. Blau, P., *Wear Testing*, in *Metals Handbook Desk Edition*, J. Davis, Editor. 1998, ASM International. p. 1342-1347.
49. Budinski, K., *Surface Engineering for Wear Resistance*. 1988: Prentice Hall.
50. Tabor, D. *Status and direction of tribology as a science in the 80'S: Understanding and Prediction*. 1984. Washington, DC, USA: NASA, Scientific & Technical Information Branch.
51. Lim, S.C. and M.F. Ashby, *Overview no. 55 Wear-Mechanism maps.* Acta Metallurgica, 1987. **35**(1): p. 1-24.
52. Lim, S., *Recent developments in wear-mechanism maps.* Tribology International, 1998. **31**(1-3): p. 87-97.
53. Liu, Y., R. Asthana, and P. Rohatgi, *A map for wear mechanisms in aluminium alloys.* Journal of Materials Science, 1991. **26**(1): p. 99-102.
54. Antoniou, R. and C. Subramanian, *Wear mechanism map for aluminium alloys.* Scripta Metallurgica, 1988. **22**(6): p. 809-814.
55. Moore, M. and R. Douthwaite, *Plastic Deformation Below Worn Surfaces.* Metall. Trans. A, 1976. **7**(12): p. 1833-1839.
56. Rigney, D., M. Naylor, R. Divakar, and L. Ives, *Low Energy Dislokation and Substrutures Caused by Sliding and by Particall Impact.* Materials Science and Engineering, 1986. **81**: p. 409-425.
57. Rigney, D.A. and W.A. Glaeser, *The significance of near surface microstructure in the wear process.* Wear, 1978. **46**(1): p. 241-250.

58. Rigney, D.A. and J.P. Hirth, *Plastic deformation and sliding friction of metals.* Wear, 1979. **53**(2): p. 345-370.
59. Bikerman, J.J., *Adhesion in friction.* Wear, 1976. **39**(1): p. 1-13.
60. Hosking, F.M., F.F. Portillo, R. Wunderlin, and R. Mehrabian, *Composites of Aluminum-Alloys - Fabrication and Wear Behavior.* Journal of Materials Science, 1982. **17**(2): p. 477-498.
61. Rigney, D.A., L.H. Chen, M.G.S. Naylor, and A.R. Rosenfield, *Wear processes in sliding systems.* Wear, 1984. **100**(1-3): p. 195-219.
62. Sasada, T., *Wear research in Japan: Trends and future directions.* Wear, 1984. **100**(1-3): p. 561-577.
63. Feng, Z. and K. Tandon, *Behavior of surface layers during the reciprocating wear of SiC-Al/Si metal matrix composites.* Scripta Metallurgica et Materiala, 1995. **32**(4): p. 523-528.
64. Kerridge, M. and J. Lancaster, *The Stages in a Process of Severe Metallic Wear.* Proceedings of the Royal Society of London. Series A, Mathematical and Physical Sciences (1934-1990), 1956. **236**(1205): p. 250-264.
65. Heilmann, P., J. Don, T. Sun, W. Glaeser, and D. Rigney, *Characterization of wear surfaces and wear debris generated by sliding.* Wear, 1983. **91**: p. 171-190.
66. Chen, L.H., *Deformation, transfer and debris formation during sliding wear of metals.* Scripta Metallurgica Et Materialia, 1990. **24**(5): p. 827-832.
67. Subramanian, C., *On mechanical mixing during dry sliding of aluminium-12.3wt.%silicon alloy against copper.* Wear, 1993. **161**(1-2): p. 53-60.
68. Li, X.Y. and K.N. Tandon. *Mechanical mixing induced by sliding wear of an Al-Si alloy against M2 steel*. 1999. Switzerland: Elsevier.
69. Lederich, R. and S. Sastry, *Deformation Behaviour of SiCM Reinforced Al composites.* Mat. Sci, & Eng, 1982. **55**: p. 143-146.
70. Arsenault, R. and R. Fisher, *Microstructure of fiber and particulate SiC in 6061 Al composites.* Scripta Metallurgica, 1983. **17**(1): p. 67-71.
71. Arsenault, R.J., L. Wang, and C.R. Feng, *Strengthening of composites due to microstructural changes in the matrix.* Acta Metallurgica et Materialia, 1991. **39**(1): p. 47-57.

72. Taya, M. and K. Lulay, *DJL ioyd. Strengthening of a particulate metal matrix composite by quenching [J]*. Acta Metall, 1991. **39**: p. 73-87.
73. Nardone, V. and K. Prewo, *On the strength of discontinuous silicon carbide reinforced aluminum alloys.* Scripta metall, 1986. **20**: p. 43-48.
74. Levi, C., G. Abbaschian, and R. Mehrabian, *Interface interactions during fabrication of aluminum alloy-alumina fiber composites.* Metallurgical and Materials Transactions A, 1978. **9**(5): p. 697-711.
75. Wang, N., Z. Wang, and G. Weatherly, *Formation of magnesium aluminate (spinel) in cast SiC particulate-reinforced Al (A356) metal matrix composites.* Metallurgical and Materials Transactions A, 1992. **23**(5): p. 1423-1430.
76. Nutt, S.R. and R.W. Carpenter, *Non-equilibrium phase distribution in an Al-SiC composite.* Material Science and Engineering, 1985. **75**: p. 169-77.
77. Reddy, A.S., B.N.P. Bai, K.S.S. Murthy, and S.K. Biswas, *Wear and seizure of binary Al---Si alloys.* Wear, 1994. **171**(1-2): p. 115-127.
78. Martinez, M.A., A. Martin, and J. Llorca, *Wear of Al-Si Alloys and Al-Si/Sic Composites at Ambient and Elevated-Temperatures.* Scripta Metallurgica Et Materialia, 1993. **28**(2): p. 207-212.
79. Martin, A., M.A. Martinez, and J. LLorca, *Wear of SiC-reinforced Al-matrix composites in the temperature range 20-200 degrees C.* Wear, 1996. **193**(2): p. 169-179.
80. Wilson, S. and A.T. Alpas, *Effect of temperature on the sliding wear performance of Al alloys and Al matrix composites.* Wear, 1996. **196**(1-2): p. 270-278.
81. Singh, J. and A.T. Alpas, *High-temperature wear and deformation processes in metal matrix composites.* Metallurgical and Materials Transactions a-Physical Metallurgy and Materials Science, 1996. **27**(10): p. 3135-3148.
82. Gall, K., M.F. Horstemeyer, M. Van Schilfgaarde, and M.I. Baskes, *Atomistic simulations on the tensile debonding of an aluminum-silicon interface.* Journal of the Mechanics and Physics of Solids, 2000. **48**(10): p. 2183-2212.
83. Ward, D.K., W.A. Curtin, and Y. Qi, *Aluminum-silicon interfaces and nanocomposites: A molecular dynamics study.* Composites Science and Technology, 2006. **66**(9): p. 1151-1161.

84. Komanduri, R., N. Chandrasekaran, and L. Raff, *Molecular dynamics (MD) simulation of uniaxial tension of some single-crystal cubic metals at nanolevel.* International Journal of Mechanical Sciences, 2001. **43**(10): p. 2237-2260.
85. Baskes, M.I., *Modified Embedded-Atom Potentials for Cubic Materials and Impurities.* Physical Review B, 1992. **46**(5): p. 2727-2742.
86. Allen, M. and D. Tildesley, *Computer Simulation of Liquids*. 1989: Oxford University Press, USA.
87. Davidson, D.L., *Fracture toughness of particulate Metal Matrix Composites*. Metal Matrix Composites: Mechanisms and Properties, ed. R.K. Everett and R.J. Arsenault. 1991, Boston: Academic Press.
88. Venkatesh, T.A., K.J. Van Vliet, A.E. Giannakopoulos, and S. Suresh, *Determination of elasto-plastic properties by instrumented sharp indentation: guidelines for property extraction.* Scripta Materialia, 2000. **42**(9): p. 833-839.
89. Giannakopoulos, A.E. and S. Suresh, *Determination of elastoplastic properties by instrumented sharp indentation.* Scripta Materialia, 1999. **40**(10): p. 1191-1198.
90. VanLandingham, M.R., *Review of instrumented indentation.* Journal of Research of the National Institute of Standards and Technology, 2003. **108**(4): p. 249-265.
91. Oliver, W. and G. Pharr, *Improved technique for determining hardness and elastic modulus using load and displacement sensing indentation experiments.* Journal of Materials Research, 1992. **7**(6): p. 1564-1583.
92. Alcala, J., A.C. Barone, and M. Anglada, *The influence of plastic hardening on surface deformation modes around vickers and spherical indents.* Acta Materialia, 2000. **48**(13): p. 3451-3464.
93. Das, G., S. Ghosh, S. Ghosh, and R.N. Ghosh, *Materials characterization and classification on the basis of materials pile-up surrounding the indentation.* Materials Science and Engineering: A, 2005. **408**(1-2): p. 158-164.
94. Xu, Z.H. and D. Rowcliffe, *Method to determine the plastic properties of bulk materials by nanoindentation.* Philosophical Magazine a-Physics of Condensed Matter Structure Defects and Mechanical Properties, 2002. **82**(10): p. 1893-1901.

95. Giannakopoulos, A.E., P.-L. Larsson, and R. Vestergaard, *Analysis of Vickers indentation.* International Journal of Solids and Structures, 1994. **31**(19): p. 2679-2708.

96. Hatch, J., *Aluminum: Properties and Physical Metallurgy*. 1984: ASM International.

97. Dukino, R.D. and M.V. Swain, *Comparative Measurement of Indentation Fracture-Toughness with Berkovich and Vickers Indenters.* Journal of the American Ceramic Society, 1992. **75**(12): p. 3299-3304.

98. Laugier, M.T., *Palmqvist Indentation Toughness in Wc-Co Composites.* Journal of Materials Science Letters, 1987. **6**(8): p. 897-900.

99. Casellas, D., A. Feder, L. Llanes, and M. Anglada, *Fracture toughness and mechanical strength of Y-TZP/PSZ ceramics.* Scripta Materialia, 2001. **45**(2): p. 213-220.

100. Niihara, K., *A Fracture-Mechanics Analysis of Indentation-Induced Palmqvist Crack in Ceramics.* Journal of Materials Science Letters, 1983. **2**(5): p. 221-223.

101. Anstis, G.R., P. Chantikul, B.R. Lawn, and D.B. Marshall, *A Critical-Evaluation of Indentation Techniques for Measuring Fracture-Toughness .1. Direct Crack Measurements.* Journal of the American Ceramic Society, 1981. **64**(9): p. 533-538.

102. Lawn, B., A. Evans, and D. Marshall, *Elastic/Plastic Indentation Damage in Ceramics: The Median/Radial Crack System.* Journal of the American Ceramic Society, 1980. **63**(9-10): p. 574-581.

103. Dukino, R. and M. Swain, *Comparative Measurement of Indentation Fracture Toughness with Berkovich and Vickers Indenters.* Journal of the American Ceramic Society, 1992. **75**(12): p. 3299-3304.

104. Weppelmann, E.R., J.S. Field, and M.V. Swain, *Observation, Analysis, and Simulation of the Hysteresis of Silicon Using Ultra-Micro-Indentation with Spherical Indenters.* Journal of Materials Research, 1993. **8**(4): p. 830-840.

105. Bradby, J.E., J.S. Williams, J. Wong-Leung, M.V. Swain, and P. Munroe, *Transmission electron microscopy observation of deformation microstructure under spherical indentation in silicon.* Applied Physics Letters, 2000. **77**(23): p. 3749-3751.

106. Bradby, J., J. Williams, J. Wong-Leung, M. Swain, and P. Munroe, *Transmission electron microscopy observation of deformation microstructure under spherical indentation in silicon.* Applied Physics Letters, 2000. **77**: p. 3749.

107. Domnich, V., Y. Gogotsi, and S. Dub, *Effect of phase transformations on the shape of the unloading curve in the nanoindentation of silicon.* Applied Physics Letters, 2000. **76**: p. 2214.

108. Leipner, H., D. Lorenz, A. Zeckzer, H. Lei, and P. Grau, *Nanoindentation pop-in effect in semiconductors.* Physica B: Physics of Condensed Matter, 2001. **308**: p. 446-449.

109. Jang, J. and G. Pharr, *Influence of indenter angle on cracking in Si and Ge during nanoindentation.* Acta Materialia, 2008. **56**(16): p. 4458-4469.

110. Giannakopoulos, A., P. Larsson, and R. Vestergaard, *Analysis of vickers indentation.* International Journal of Solids and Structures, 1994. **31**(19): p. 2679-2708.

111. Larsson, P., A. Giannakopoulos, E. Soderlund, D. Rowcliffe, and R. Vestergaard, *Analysis of Berkovich indentation.* International Journal of Solids and Structures, 1996. **33**(2): p. 221-248.

112. Zeng, K. and L. Shen, *A new analysis of nanoindentation load-displacement curves.* Philosophical Magazine A, 2002. **82**(10): p. 2223-2229.

113. Juliano, T., Y. Gogotsi, and V. Domnich, *Effect of indentation unloading conditions on phase transformation induced events in silicon.* J. Mater. Res, 2003. **18**(5): p. 1193.

114. Malzbender, J. and G. de With, *The use of the indentation loading curve to detect fracture of coatings.* Surface & Coatings Technology, 2001. **137**(1): p. 72-76.

115. Babout, L., E. Maire, J. Bufficre, and R. Fougcres, *Characterization by X-ray computed tomography of decohesion, porosity growth and coalescence in model metal matrix composites.* Acta Materialia, 2001. **49**(11): p. 2055-2063.

116. Schmidt, S., S. Nielsen, C. Gundlach, L. Margulies, X. Huang, and D. Jensen, *Watching the Growth of Bulk Grains During Recrystallization of Deformed Metals*. 2004, American Association for the Advancement of Science. p. 229-232.

117. Spowart, J., *Automated serial sectioning for 3-D analysis of microstructures.* Scripta Materialia, 2006. **55**(1): p. 5-10.
118. Alkemper, J. and P. Voorhees, *Quantitative serial sectioning analysis.* Journal of Microscopy, 2001. **201**(3): p. 388-394.
119. Spowart, J., H. Mullens, and B. Puchala, *Collecting and analyzing microstructures in three dimensions: A fully automated approach.* JOM Journal of the Minerals, Metals and Materials Society, 2003. **55**(10): p. 35-37.
120. Hainsworth, S., H. Chandler, and T. Page, *Analysis of nanoindentation load-displacement loading curves.* Journal of Materials Research, 1996. **11**(8): p. 1987-1995.
121. Reddy, A.S., B.N.P. Bai, K.S.S. Murthy, and S.K. Biswas, *Wear and Seizure of Binary Al-Si Alloys.* Wear, 1994. **171**(1-2): p. 115-127.
122. Dighe, M.D. and A.M. Gokhale, *Relationship between microstructural extremum and fracture path in a cast Al-Si-Mg alloy.* Scripta Materialia, 1997. **37**(9): p. 1435-40.
123. Alpas, A.T., M. Elmadagli, and T. Perry, *A parametric study of the relationship between microstructure and wear resistance of Al-Si alloys.* Wear, 2007. **262**(1-2): p. 79-92.
124. Yun-Biao, X., K.J. Hsia, and D.A. Lange, *Quantitative characterization of the fracture surface of Si single crystals by confocal microscopy.* Journal of the American Ceramic Society, 1995. **78**(12): p. 3201-8.
125. Brede, M. and P. Haasen, *The brittle-to-ductile transition in doped silicon as a model substance.* Acta Metallurgica, 1988. **36**(8): p. 2003-2018.
126. Chen, C.P. and M.H. Leipold, *Fracture toughness of silicon.* American Ceramic Society Bulletin, 1980. **59**(4): p. 469-72.
127. Casellas, D., J. Caro, S. Molas, J.M. Prado, and I. Valls, *Fracture toughness of carbides in tool steels evaluated by nanoindentation.* Acta Materialia, 2007. **55**(13): p. 4277-4286.
128. Ericson, F., S. Johansson, and J.-A. Schweitz, *Hardness and fracture toughness of semiconducting materials studied by indentation and erosion techniques.*

Materials Science & Engineering A: Structural Materials: Properties, Microstructure and Processing, 1988. **A105-6**(pt1): p. 131-141.

129. Liang, Z. and Y. Yingxue, *Single crystal bulk material micro/nano indentation hardness testing by nanoindentation instrument and AFM.* Materials Science & Engineering A (Structural Materials: Properties, Microstructure and Processing), 2007. **460-461**: p. 95-100.
130. Davis, J., *Aluminum and Aluminum Alloys*. 1993: ASM International.
131. *Tip Selection Guide*, in *http://www.hysitron.com*, H. Incorporated, Editor. 2008.
132. ABAQUS, I., *ABAQUS Documentation Version 6.8.* ABAQUS Inc., Rawtucket, RI, 2008.
133. Zhang, L. and M. Mahdi, *The plastic behaviour of silicon subjected to micro-indentation.* Journal of Materials Science, 1996. **31**(21): p. 5671-6.
134. Kiser, M.T., F.W. Zok, and D.S. Wilkinson, *Plastic flow and fracture of a particulate metal matrix composite.* Acta Materialia, 1996. **44**(9): p. 3465-76.

LIST OF PUBLICATIONS AND CONFERENCE PRESENTATIONS RESULTING FROM THIS WORK

Publications resulting from this work:

Su, J., Nie, X., Stoilov V., and Yang Q. Characterization of the Al/Si interfaces under dry wear conditions. Journal of Vacuum science and technology A. Accepted for publication in Jul/Aug 2009

Conference presentations resulting from this work:

Su, J., Nie, X., and Stoilov, V. (October 2008) Characterization of the Al/Si interfaces under dry wear conditions. AVS 55th International Symposium. Boston, MA, USA

VITA AUCTORIS

NAME:	Jun Feng Su
PLACE OF BIRTH:	Wuhan, China
YEAR OF BIRTH:	1971
EDUCATION:	Nanjing University of Science & Technology, China 1988-1992, B.Sc Nanyang Technological University, Singapore 2003-2005, M.Eng University of Windsor, Canada 2007-2009, M.A.Sc